

---

# Single Plane Compton Imaging for Range Verification in Proton Therapy - A Proof-of-Principle Study -

---

MASTERARBEIT  
zur Erlangung des Hochschulgrades  
Master of Science  
im Master-Studiengang Physik

**B. Sc. Jonathan Berthold**  
geboren am 31.03.1993 in Dresden

Institut für Kern- und Teilchenphysik  
Fachrichtung Physik  
Fakultät Mathematik und Naturwissenschaften  
Technische Universität Dresden  
2018



Eingereicht am 5. Juli 2018

1. Gutachter:	Prof. Dr. Arno Straessner
2. Gutachter:	Prof. Dr. Wolfgang Enghardt
Betreuer:	Dr. Guntram Pausch

## Abstract

Proton and ion therapy has become widely spread over the course of the last two decades as cost and size of accelerators have lowered. The clinical advantage of having a conformal dose distribution while sparing healthy tissue is encountered by high range uncertainties and missing monitoring of the range. Ongoing research activities try to develop detection systems for range verification of the proton beam during the treatment. Many ideas are based on measuring prompt gamma radiation produced by nuclear reactions in the target. Most of the systems reach their detection limit under clinical condition, i.e. high load and short irradiation time. There are attempts to introduce segmented detectors for load reduction in order to be able to gain more statistics. Such a segmented system could exploit the principle of a Directional Gamma Radiation Detector (DGRD). The DGRD is based on the angular distribution of the energy from Compton scattered events deposited in different detectors. A coincident detection of these Compton scattered events enables a reconstruction of the position of a radiation source. In the present thesis it is shown, that this principle can be transferred to energies of prompt gamma radiation. Further, different methods for range extraction based on the mean energy difference (FOM) and matching of the coincident spectra are discussed. In a proof-of-principle setup with a two  $\varnothing 2'' \times 2''$  cerium bromide scintillator a precision of few millimeters is achieved for a homogenous phantom. This precision is obtained at a statistic of 1000 to 10 000 times the number of events from a single pencil beam spot. A more segmented detector setup may yield a higher detection efficiency measured at the detection volume. Therefore the influence of segmentation on the detection efficiency is studied by a simulation at typical prompt gamma-ray energies. Aim is the development of a detector which could be used for an imaging modality as proposed by the concept of Single Plane Compton Imaging (SPCI). The simulation yields results for the first estimation on the detector dimensions.

## Kurzdarstellung

Die Protonen- und Iontherapie hat sich mit sinkenden Kosten und Verkleinerung der Teilchenbeschleuniger in den letzten zwei Dekaden als alternative Krebstherapie etabliert. Dem klinischen Vorteil einer konformalen Dosisdeposition bei gleichzeitiger Schonung des gesunden Gewebes steht eine hohe Reichweiteunsicherheit und fehlende Monitorsysteme gegenüber. Momentan gibt es viele Forschungsvorhaben auf dem Gebiet der Reichweitekontrolle, die überwiegend auf der Messung von prompter Gammastrahlung aus Kernreaktionen beruhen. Die meisten Systeme stoßen jedoch unter klinischen Bedingungen, d.h. hohe Last und kurze Bestrahlungszeit, an ihre Grenzen um ausreichend valide Ereignisse

detektieren zu können. Damit man mehr Statistik sammeln kann, gibt es Bestrebungen die vorhandenen Detektionssysteme zu segmentieren, um eine Lastreduktion der einzelnen Detektoren zu erzielen. Mit einem solchen Detektor ließe sich das Prinzip des richtungsauflösenden Gammastrahlungsdetektor anwenden. Es beruht auf der winkelabhängigen Energieverteilung der Comptonstreuung, die koinzidente Ereignisse zwischen einem Detektorpaar verursachen kann. Die Energieverteilung bei einer solchen Koinzidenz enthält Informationen über den Quellort der Strahlung. In dieser Arbeit ist gezeigt, dass eben jenes Prinzip auf den Energiebereich prompter Gammastrahlung erweitert werden kann. Weiterhin werden verschiedene Methoden zur Reichweitebestimmung mittels Differenz der Mittelwerte und Spektrenabgleich der koinzidenten Spektren diskutiert. Dabei wird in einem grundlegendem Aufbau mit zwei  $\varnothing 2'' \times 2''$  Cerbromid Szintillatoren eine Genauigkeit der Reichweitebestimmung von wenigen Millimetern für ein homogenes Phantom erreicht. Diese Größenordnung erhält man bei einer tausend- bis zehntausendfachen Statistik eines einzelnen Punktes im Rasterscanverfahren. Andere Detektorgeometrien wie ein pixelierter Detektor können eine höhere Detektionseffizienz bei gleichem Detektorvolumen erreichen. Deshalb wurde mit einer Simulation der Einfluss der Segmentierung auf die Detektionseffizienz für typische Energien der prompten Gammastrahlung untersucht. Ziel dabei ist die Entwicklung eines Detektors, der sich für ein bildgebendes Verfahren, dem sogenannten Single Plane Compton Imaging (SPCI), eignet. Die Simulation kann dafür eine erste Abschätzung der Detektorabmessung liefern.

# Contents

<b>Acronyms</b>	<b>vii</b>
<b>1 Basics of Proton Therapy</b>	<b>1</b>
1.1 Interactions of Protons with Matter . . . . .	1
1.2 Proton Therapy from a Physical and Clinical Perspective . . . . .	3
1.3 Range Uncertainties in Proton Therapy . . . . .	5
1.4 Prompt Gamma Radiation for Range Verification . . . . .	6
1.5 Range Verification Methods Based on Prompt Gamma Radiation . . . . .	7
<b>2 The Directional Gamma Radiation Detector</b>	<b>9</b>
2.1 Principle of a Classical Compton Camera . . . . .	10
2.2 Principle of a Directional Gamma Radiation Detector . . . . .	11
2.2.1 The Figure of Merit as Measure . . . . .	14
2.2.2 The Scintillation Mechanism in Inorganic Crystals . . . . .	16
2.3 Generalization of a DGRD: Single Plane Compton Imaging . . . . .	17
<b>3 A Proof-Of-Principle Experiment</b>	<b>19</b>
3.1 Characterization of the Detection System . . . . .	19
3.2 Benchmark of the Detection System . . . . .	22
3.3 Setup at the Experimental Beam Line of OncoRay Dresden . . . . .	23
<b>4 Methods for Data Analysis</b>	<b>27</b>
4.1 A General Algorithm for Finding Coincidences . . . . .	27
4.2 The Bootstrapping Method for Energy Calibration . . . . .	29
4.3 Combinatorial Study on Coincidences . . . . .	33
4.4 Energy Selection . . . . .	35

---

<b>5</b>	<b>Modeling Based on the Geant4 Simulation Toolkit</b>	<b>39</b>
5.1	Introduction to the Geant4 Simulation Toolkit . . . . .	39
5.2	Features of the Simulation . . . . .	40
5.3	Choosing the Right Physics List . . . . .	43
5.3.1	The High Precision (HP) Neutron Model Problem . . . . .	47
<b>6</b>	<b>Experimental and Simulated Results</b>	<b>51</b>
6.1	Experimental Results of the Figure of Merit . . . . .	51
6.2	Simulation of Conditional Spectra . . . . .	56
6.3	Simulated Results of the Figure of Merit in Comparison . . . . .	60
<b>7</b>	<b>Optimizing a SPCC for Range Verification</b>	<b>65</b>
7.1	Test of a Template Matching Algorithm . . . . .	65
7.2	Efficiency of the Detector Setup . . . . .	68
7.3	Efficiency of a Segmented Detector . . . . .	71
<b>8</b>	<b>Summary and Conclusion</b>	<b>75</b>
	<b>Bibliography</b>	<b>77</b>
	<b>List of Figures</b>	<b>85</b>
	<b>List of Tables</b>	<b>89</b>

# Acronyms

ADC	Analog-to-Digital Converter
CSDA	Continuous Slowing Down Approximation
DGRD	Directional Gamma Radiation Detector
FOM	Figure of Merit
LET	Linear Energy Transfer
ML-EM	Maximum Likelihood Estimation Maximization
PBS	Pencil-Beam-Scanning
PGI	Prompt Gamma-Ray Imaging
PGS	Prompt Gamma-Ray Spectroscopy
PGT	Prompt Gamma-Ray Timing
PMMA	Polymethylmethacrylat
PMT	Photomultiplier Tube
ROI	Region of Interest
SOBP	Spread-Out Bragg Peak
SPCC	Single Plane Compton Camera
SPCI	Single Plane Compton Imaging
UPTD	Universitäts Protonen Therapie Dresden





# 1 Basics of Proton Therapy

In Germany cancer is the second most common cause of death [DESTATIS, 2017]. In 2014 there have been about 476 000 newly diagnosed cancer patients estimated by the Robert Koch Institute in Berlin. As of current statistics more or less every second person will suffer from cancer once in his or her lifetime. The direct mortality rate for some tumors lies as high as 24.4% for lung cancers. [Koch-Institut, 2017]

These facts show how important cancer therapy is for our society. Cancer treatment has three important pillars: surgery, drug therapy such as chemotherapy, immunotherapy, and hormone therapy, and last but not least radiotherapy which is often combined with the other types. There are different types of radiotherapy, first of all the conventional X-ray therapy. Over the last two decades also proton and ion therapy have developed to a widely spread application for cancer treatment in radiotherapy. There are currently 68 proton and eleven C-ion facilities worldwide (April 2018) [PTCOG, 2018]. In this chapter the physical basis and clinical challenges of proton therapy shall be discussed.

## 1.1 Interactions of Protons with Matter

Protons as being positively charged, do primarily interact with matter through Coulomb force. They lose their energy mainly by interactions with orbital electrons of the penetrated material. Rarely they also lose energy due to inelastic scattering with the target nuclei, putting them into an excited state. Compared to other heavy charged particles protons tend to be scattered elastically by the target nuclei a lot, especially at the end of their range. Looking at the projected range of a proton beam on its initial axis, the range will be affected by this lateral broadening [Knoll, 2010, p. 30 ff.]. But this effect can be neglected in the clinical regime [Paganetti, 2012, p. 35].

The slowing down process of a heavy charged particle is described by the *linear stopping power*  $S$ . It is defined as the differential energy loss for a particle in a specific material per differential path length:

$$S := - \left( \frac{dE}{dx} \right) \quad (1.1.1)$$

The linear stopping power along the particle's path due to ionization is modeled by the *Bethe-Bloch-formula* [Leo, 1994, p. 24]:

$$-\left(\frac{dE}{dx}\right) = 2\pi N_a r_e c^2 \rho z_{eff} \frac{Z}{A} \frac{1}{\beta^2} \left[ \ln \frac{2m_e c^2 \beta^2 \gamma^2 T_{max}}{I^2} - 2\beta^2 - \delta - 2\frac{C}{Z} \right] \quad (1.1.2)$$

$$\text{with: } \beta = \frac{v}{c} \text{ and } \gamma = \frac{1}{\sqrt{1 - \beta^2}}$$

$N_a$  ... Avogadro's number

$r_e$  ... classical electron radius

$m_e$  ... electron mass

$\rho$  ... density of stopping material

$z_{eff}$  ... effective charge of the incident particle

$Z$  ... atomic number of stopping material

$A$  ... atomic weight of stopping material

$T_{max}$  ... maximum energy transfer in a single collision

$I$  ... average excitation potential of target atoms

$\delta$  ... density correction

$C$  ... shell correction

For particles up to few hundred MeV per nucleon there is a  $\frac{1}{v^2}$  dependency of the specific energy loss according to this formula. In the high energy regime above several hundred MeV per nucleon its value reaches a near-constant broad minimum due to the logarithmic term of the formula. Obviously, there is a strong influence of the target material denoted by the term  $\rho \frac{Z}{A}$  and the intruding particle's charge  $z_{eff}$ . According to Paganetti, 2012 the particle energy in proton therapy is in the range of 3 - 300 MeV which means there is still a  $\frac{1}{v^2}$  dependency of the specific energy loss.

The plot of the specific energy loss along the track of a heavy charged particle is known to be the Bragg curve with the well known Bragg peak. Because the energy deposition is a stochastic process, range straggling occurs and the range of one specific particle is not exactly predictable. Therefore the Bragg curve of a parallel monoenergetic particle beam is broadened as shown in Figure 1.1.1. The mean range  $R(E_0)$  can be calculated using the *Continuous Slowing Down Approximation (CSDA)* [Berger et al., 2017].

$$R(E_0) = \int_0^{E_0} \frac{1}{S(E_0)} dE \quad (1.1.3)$$

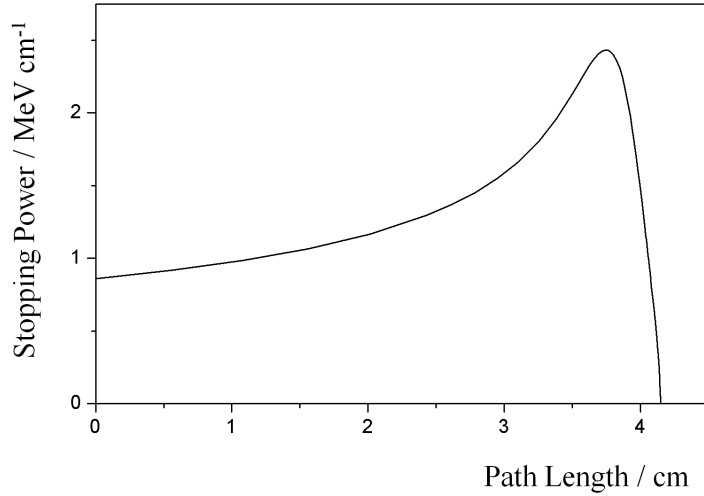


**Figure 1.1.1:** Exemplary Bragg curve with Bragg peak of 5.49 MeV  $\alpha$ -particles in air. (Adopted from [Paul, 2006](#))

## 1.2 Proton Therapy from a Physical and Clinical Perspective

The Bragg curve in Figure 1.1.1 shows that heavy charged particles such as protons deposit most of their energy (area under the curve) towards the end of their range in a sharp region, the Bragg peak. This behavior seems predestined for the treatment of cancers especially those which are not close to the body's surface.

From a physical perspective the depth-dose curve is an appropriate measure in optimizing the outcome of therapy. The *physical dose*  $D$  is defined as energy deposition in a certain volume with respect to its mass and is measured in *Gray* ( $1 \text{ Gy} = 1 \text{ J/kg}$ ):

$$D := \frac{dE}{dm} = \frac{1}{\rho} \frac{dE}{dV} \quad (1.2.1)$$

The dose is a very basic measure for radiation damage and does not consider biological effects. Assuming the energy transfer to the tissue is local to the beam track, the depth-dose curve and the Bragg curve are alike. This is described by the *Linear Energy Transfer (LET)*  $L$  which only considers energy deposition less than a defined ionization energy  $\Delta$ :

$$L_{\Delta} := \frac{dE_{\Delta}}{dx} \quad (1.2.2)$$

But in reality energy could also be transferred into the volume. For instance, there are

high energetic electrons produced, so called  $\delta$ -rays. Also, not described by the Bethe-Bloch-formula, there occur nuclear reactions induced by inelastic scattering on a target nuclei [Paganetti, 2012, p. 54]. High energetic gamma photons from these reactions can even escape the patient's body.

From a therapeutic perspective the interest is set to the cell death caused by proton radiation which is of course correlated to the dose deposition. In general this is not an easy task, because the mechanisms of cell death are not yet completely understood. Currently, cell death is believed to be mainly caused by double-strand breakage of the cell's DNA. Radiation with high LET like protons is causing more of such breakages as low LET radiation like X-ray photons. Moreover, it has been found, that the *relative biological effectiveness (RBE)* of radiation compared to X-ray photons is LET depended and has a maximum value for about  $100 \text{ keV } \mu\text{m}^{-1}$  which for example corresponds to low energetic protons at the distal falloff of the Bragg peak [Sørensen et al., 2011]. This is in focus of current research and might have an influence on future treatment planning [Giovannini et al., 2016].

The challenge of proton therapy does not only comprise models for cell death, but the main issue is to determine the relative stopping power of the irradiated tissue. This is a physical problem which can be encountered in a number of ways. In the state-of-the-art proton therapy the relative stopping power is derived from computer tomographic (CT) Hounsfield units [Paganetti, 2012, p. 240]. This holds a great uncertainty since the Hounsfield scale, symbolizing the extinction coefficient of an X-rays spectrum, does not perfectly correlate with the electron density which is most important for the stopping power calculation. There is a new method using dual-energy-CT to estimate the electron density much more precisely [Wohlfahrt et al., 2017]. Additionally the material composition is important because of the protons interacting with the nuclei as well. Ideally there would be a method to measure the proton stopping power directly, for instance via proton radiography or tomography. But there are two main issues appearing. First of all there is no device yet which could produce a comparable image to computer tomography in the same time, thus proton radiography is simply uneconomic. Secondly the maximal energy of current clinical accelerators is too low for the radiography of some parts of the body. The IBA isochronous cyclotron at OncoRay for instance yields maximal 230 MeV per proton which corresponds to a CSDA range of 33 cm in water. Because ion imaging does not seem to be applied soon, there are ideas for verifying the proton range from the conversion of Hounsfield units directly during the beam application. Generally there is a high demand for in-vivo online range verification because of many uncertainties arising in the workflow of proton therapy as described in the next section.

### 1.3 Range Uncertainties in Proton Therapy

In the treatment, a homogeneous dose distribution is realized by the weighted superposition of depth-dose curves of different proton energies. The resulting dose distribution is called the *Spread-Out Bragg Peak (SOBP)*. There exist two different modes in delivering the dose to the patient. In Double-Scattering-Mode a monoenergetic beam is passively modulated and collimated by massive components in the beam's path. Because this is expensive in terms of time and costs, many facilities have established the so called Pencil-Beam-Scanning (PBS). In PBS mode the tumor is divided in layers of constant energy which are scanned spot-wise by deflecting magnets as shown in Figure 1.3.1. In this thesis, estimations on the proton range will refer to the statistics of a single spot.

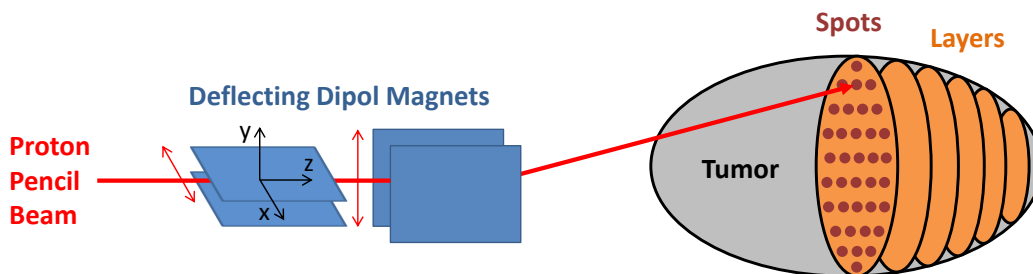


**Figure 1.3.1:** Principle of dose delivery in Pencil-Beam-Scanning (PBS) mode. Deflecting magnets vary the beam of width of a pencil in the x- and y-plane and the beam energy modulates the penetration depth in z-direction.

Range verification is demanded in proton therapy as the advantage of the highly localized dose deposition of protons cannot yet completely be exploited. The depth-dose curve of protons is extremely sensitive to uncertainties in range. From Figure 1.3.2 it becomes clear that range uncertainties in proton therapy are much more critical than in the conventional radiotherapy using photons. The most dominant uncertainties in proton therapy arise from patient positioning, the conversion of CT Hounsfield units to relative proton stopping power, and interfractional changes of the tissue. By considering these effects all clinics use rather broad safety margins to ensure complete tumor coverage. These safety margins do generally increase with proton range. For the Universitäts Protonen Therapie Dresden (UPTD) the margin is calculated by 3.5% of the proton range plus 1 mm [Hueso-González et al., 2016]. Reducing the safety margin means sparing much more healthy tissue and thus lowering the risk of side effects and preventing recurrence. The aim of research performed by many groups worldwide is to achieve this by verifying the proton range in real time during the treatment [Knopf and Lomax, 2013].

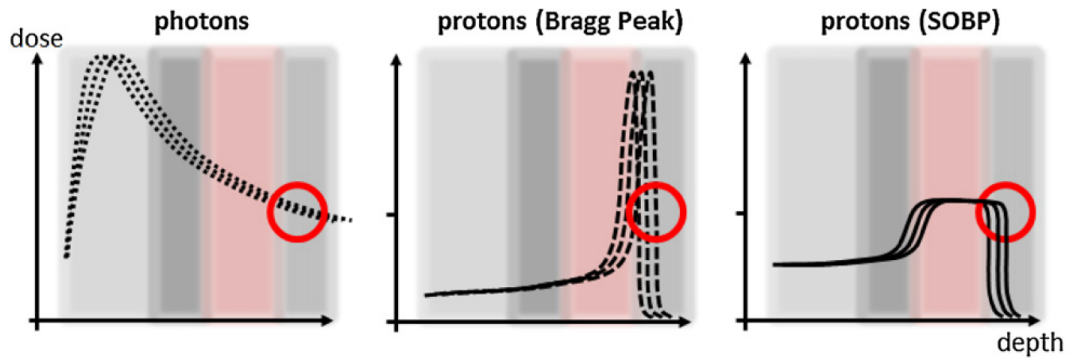


**Figure 1.3.2:** Influence of range uncertainties on the depth dose curves of photons (left) protons (middle) and the SOBP (right). The gray scales symbolize different tissues and the red region indicates the position of the tumor. The different curves result from range uncertainties. From the red circles can be seen that for proton therapy the dose deposition in the healthy tissue due to range uncertainties increases drastically in contrast to the case of photons. (Courtesy of [Knopf and Lomax, 2013](#))

## 1.4 Prompt Gamma Radiation for Range Verification

Range verification is rather difficult since the protons are completely stopped in the tissue and can therefore not be measured directly. Hence one has to find secondary signatures encoding the range of the protons. In this thesis the focus for range verification is laid upon prompt gamma radiation from nuclear interactions of protons with target nuclei. Roughly every tenth proton at clinical energies produces prompt gamma radiation [[Smeets, 2012](#)]. Since the energy of most prompt gamma radiation is in the order of 1-8 MeV, the chance of the photons coming out of the patient is fairly high. In addition the de-excitation process of the nuclei is almost instantaneous, on the time scale of picoseconds or less, which is why the radiation is called prompt. Hence it is most eligible for real time range verification. An example of such a nuclear reaction is shown in Figure 1.4.1.

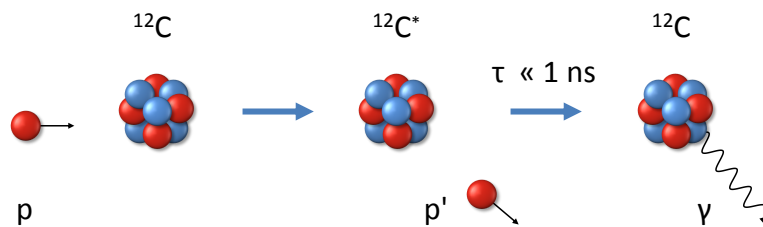


**Figure 1.4.1:** An inelastic nuclear reaction of an incident proton  $p$  with carbon  $^{12}\text{C}$  resulting in prompt gamma radiation. Reaction  $^{12}\text{C}(p, p')^{12}\text{C}^*$  with a decay time  $\tau = 88 \text{ fs}$  for the  $^{12}\text{C}^*$  isotope emitting a gamma photon with an energy of 4.44 MeV. (Adopted from [Hueso-González et al., 2016](#))

In the energy spectrum of prompt gamma radiation from Polymethylmethacrylat (PMMA) shown in Figure 1.4.2 the most dominant prompt gamma transitions for clinical applications can be found. These are the 4.44 MeV gamma line due to the reactions  $^{16}\text{O}(p, x)^{12}\text{C}^*$  and  $^{12}\text{C}(p, p')^{12}\text{C}^*$ , the 6.13 MeV line due to  $^{16}\text{O}(p, p')^{16}\text{O}^*$ , and the 0.718 MeV line due to  $^{12}\text{C}(p, x)^{10}\text{B}^*$ . In general the exact prompt gamma spectrum of course depends on the target composition and the beam energy. A list of selected transitions from [Kozlovsky et al., 2002](#) is given in table 1.4.1. [[Smeets, 2012](#)]

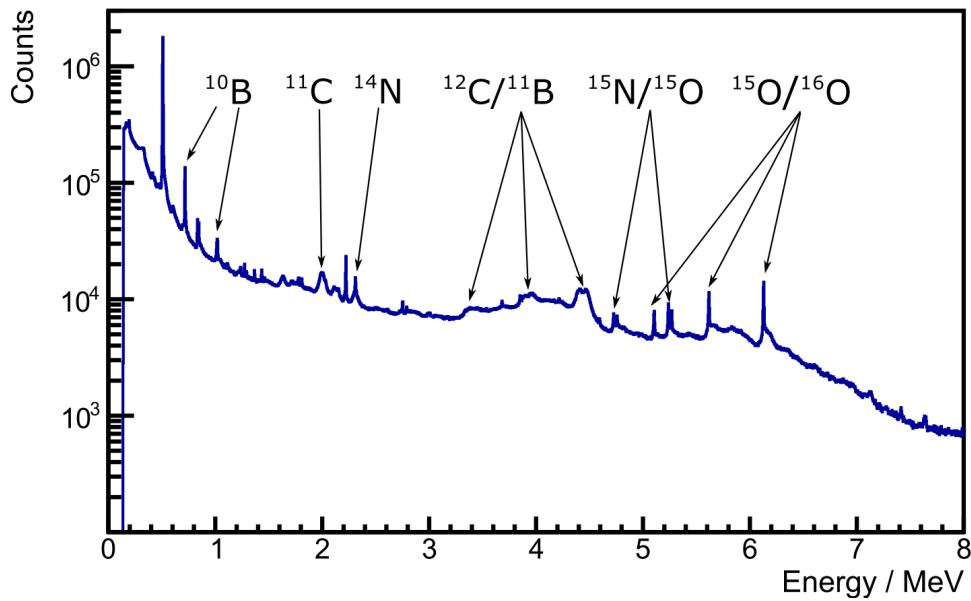


**Figure 1.4.2:** Prompt gamma-ray spectrum produced by a 150 MeV proton beam in PMMA measured with a High-Purity Germanium (HPGe) detector. (Courtesy of [Petzoldt, 2016](#))

## 1.5 Range Verification Methods Based on Prompt Gamma Radiation

There have already been proposed different methods for range verification in proton therapy. One can distinguish between three basic principles based on prompt gamma radiation. Derived from conventional imaging modalities is the approach of Prompt Gamma-Ray Imaging (PGI) with a gamma camera system. Common systems are the slit camera [[Smeets et al., 2012](#)], which has already been tested in the clinics [[Richter et al., 2016](#)], and different Compton camera solutions described in Section 2.1. The idea of Prompt Gamma-Ray Spectroscopy (PGS) is to exploit the different variation of cross sections of certain gamma-ray transitions towards the Bragg peak for range determination

**Table 1.4.1:** List of gamma-ray lines from proton reactions with  $^{16}\text{O}$  and  $^{12}\text{C}$ . Data taken from [Kozlovsky et al., 2002](#).

Energy / MeV	Transition	Nuclear Reaction	Mean life / s
0.718	$^{10}\text{B}^{*0.718} \rightarrow \text{g.s.}$	$^{12}\text{C}(\text{p}, \text{x})^{10}\text{B}^*$	$1.0 \times 10^{-9}$
		$^{16}\text{O}(\text{p}, \text{x})^{10}\text{B}^*$	$1.0 \times 10^{-9}$
1.022	$^{10}\text{B}^{*1.740} \rightarrow ^{10}\text{B}^{*0.718}$	$^{12}\text{C}(\text{p}, \text{x})^{10}\text{B}^*$	$7.5 \times 10^{-15}$
		$^{16}\text{O}(\text{p}, \text{x})^{10}\text{B}^*$	$7.5 \times 10^{-15}$
2.000	$^{11}\text{C}^{*2.000} \rightarrow \text{g.s.}$	$^{12}\text{C}(\text{p}, \text{x})^{11}\text{C}^*$	$1.0 \times 10^{-14}$
2.313	$^{14}\text{N}^{*2.313} \rightarrow \text{g.s.}$	$^{16}\text{O}(\text{p}, \text{x})^{14}\text{N}^*$	$9.8 \times 10^{-14}$
4.438	$^{12}\text{C}^{*4.439} \rightarrow \text{g.s.}$	$^{12}\text{C}(\text{p}, \text{p}')^{12}\text{C}^*$	$6.1 \times 10^{-14}$
		$^{16}\text{O}(\text{p}, \text{x})^{12}\text{C}^*$	$6.1 \times 10^{-14}$
4.444	$^{11}\text{B}^{*4.445} \rightarrow \text{g.s.}$	$^{12}\text{C}(\text{p}, 2\text{p})^{11}\text{B}^*$	$5.6 \times 10^{-19}$
5.180	$^{15}\text{O}^{*5.181} \rightarrow \text{g.s.}$	$^{16}\text{O}(\text{p}, \text{x})^{15}\text{O}^*$	$< 4.9 \times 10^{-14}$
5.240	$^{15}\text{O}^{*5.241} \rightarrow \text{g.s.}$	$^{16}\text{O}(\text{p}, \text{x})^{15}\text{O}^*$	$3.3 \times 10^{-12}$
5.269	$^{15}\text{N}^{*5.270} \rightarrow \text{g.s.}$	$^{16}\text{O}(\text{p}, 2\text{p})^{15}\text{N}^*$	$2.6 \times 10^{-12}$
5.298	$^{15}\text{N}^{*5.299} \rightarrow \text{g.s.}$	$^{16}\text{O}(\text{p}, 2\text{p})^{15}\text{N}^*$	$1.2 \times 10^{-14}$
6.129	$^{16}\text{O}^{*6.130} \rightarrow \text{g.s.}$	$^{16}\text{O}(\text{p}, \text{p}')^{16}\text{O}^*$	$2.7 \times 10^{-11}$
6.175	$^{15}\text{O}^{*6.176} \rightarrow \text{g.s.}$	$^{16}\text{O}(\text{p}, \text{x})^{15}\text{O}^*$	$< 2.3 \times 10^{-14}$

[[Verburg and Seco, 2014](#)]. The group which had found this method has now developed a prototype for clinical trials. Lastly a research group at OncoRay has discovered a method called Prompt Gamma-Ray Timing (PGT) which is capable of determining the range from a time-of-flight measurement of the protons via the prompt gamma radiation timing spectrum [[Golnik et al., 2014](#)]. All of these methods are limited in the collection of enough prompt gamma-ray events under clinical conditions, i.e. high load and short irradiation time, especially for a single pencil beam spot. This also limits the significance of detected range variation due to statistical fluctuation. Often the throughput of the detection system is restricting the number of detectable events per spot. To counteract this the idea of segmentation of the detectors arises, which leads to a reduced load per channel. Especially for PGT and PGS this could lead to more events per spot, as the detection system could be positioned closer to the patient. As positive side effect of this segmentation another detection method can be combined with the detection system. From coincident events due to Compton scattering between different detector segments the principle of a Directional Gamma Radiation Detector (DGRD) can be exploited. In this thesis it will be investigated if the principle of a DGRD can be transferred to prompt gamma-ray energies and if it is therefore applicable for range verification. If so, parameters of the efficiency shall be studied with regard to the development of a segmented Single Plane Compton Camera (SPCC). The basics principle of a DGRD and a SPCC are explained in the next chapter.



## 2 The Directional Gamma Radiation Detector

The detection of gamma radiation is mainly based on three types of interaction with matter: photoelectric effect, incoherent scattering - here in particular Compton scattering - and pair production. For each material there are different energy regimes in which these effects are dominating, as shown in Figure 2.0.1. The energy of prompt gamma radiation in proton therapy is in a range where Compton scattering and pair production are dominant. In contrast to the other two processes, Compton scattering is dependent on the initial direction of the photon. Based on this effect a detector can therefore be built for the location of a source. In this chapter different approaches to this will be introduced like the idea of a Directional Gamma Radiation Detector (DGRD).

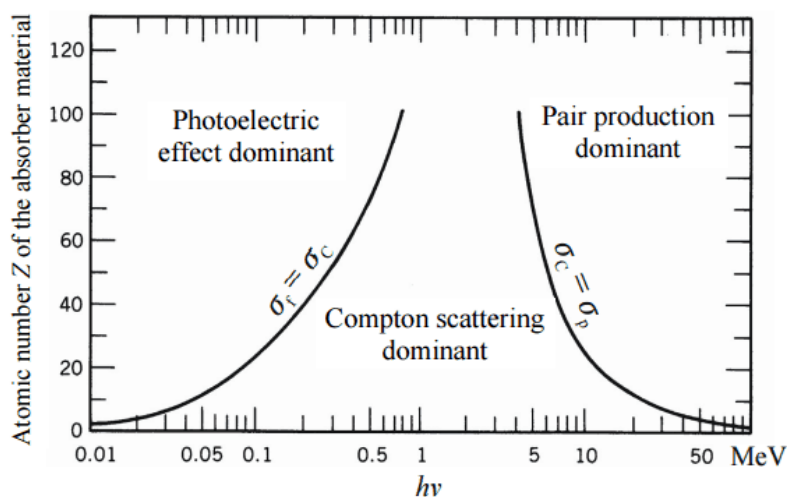


**Figure 2.0.1:** Dominant regions in energy for the three main interactions of photons with matter at different atomic numbers  $Z$ . The solid lines correspond to equal cross section of neighboring effects at photon energy  $h\nu$  and atomic number  $Z$ . [Knoll, 2010, p. 51]

## 2.1 Principle of a Classical Compton Camera

The Compton effect describes the scattering process of a photon and an electron. The incoming photon with *energy*  $E$  is deflected by an *angle*  $\theta$  with respect to its original direction of flight. Since energy and momentum are conserved and no scattering angles are restricted for the photon, the energy transfer on the recoil electron (considered at rest) can vary from zero to a large fraction of the photon's energy. The energy of the scattered photon  $E'$  can be derived from the equations of energy and momentum conservation.

$$E' = \frac{E}{1 + \frac{E}{m_e c^2} (1 - \cos \theta)} \quad (2.1.1)$$

The Compton scattered photons follow an angular distribution described by the Klein-Nishina formula for the *differential scattering cross section*  $\frac{d\sigma}{d\Omega}$ .

$$\frac{d\sigma}{d\Omega} = Z r_e^2 \left( \frac{1}{1 + \alpha \cdot A} \right)^2 \left( \frac{B}{2} \right) \left( 1 + \frac{\alpha^2 \cdot A^2}{B \cdot [1 + \alpha \cdot A]} \right) \quad (2.1.2)$$

Here are defined  $\alpha := E/m_e c^2$ ;  $A := 1 - \cos \theta$  and  $B := 1 + \cos^2 \theta$ , respectively [Knoll, 2010, p. 49 f.]. Derived from this formula, the different contours in Figure 2.1.1 show the propensity of forward scattering for photon energies as low as 100 keV. For typical prompt gamma energies of about 1-8 MeV this effect is even more dominant.

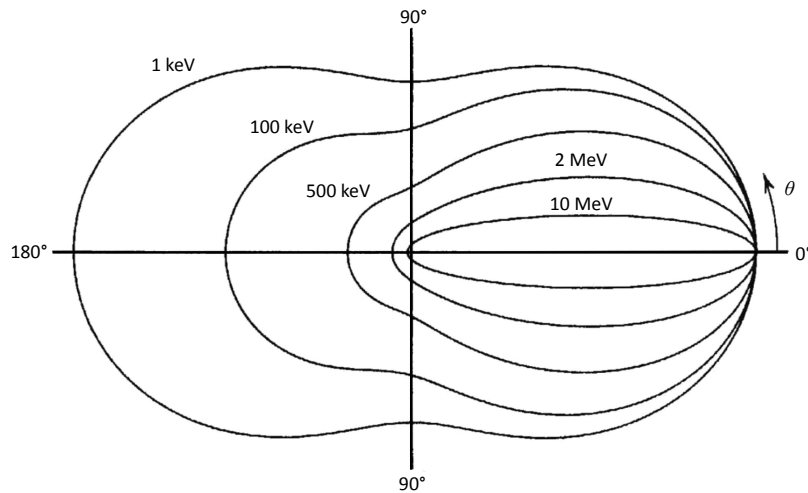


**Figure 2.1.1:** Visualization of the Klein-Nishina cross section formula in polar coordinates. The angular coordinate corresponds to the scattering angle  $\theta$  and the radial component to the cross section. The contours mark the Klein-Nishina cross section of different initial photon energies normalized on the value of forward scattering at  $0^\circ$ . [Knoll, 2010, p. 50]

The Compton kinematics set the frame of the development of a detection system based on Compton scattering. The classical Compton camera comprises a scattering plane and an absorber plane. In the scattering plane the interaction point of the Compton scattering and the recoil electron's energy are detected. The absorber plane detects the point of absorption and the energy of the scattered photon. Therefrom the determination of the momentum vector of the scattered photon and its scattering angle according to formula 2.1.1 is feasible. The initial photon's momentum vector can then be reconstructed on the surface of a cone as shown in Figure 2.1.2 (a). Most detection methods work with at least one scattering and an absorption plane. The planes need a reasonable energy and spatial resolution for reconstruction. Also the time resolution needs to be decent enough to enable the correct assignment of a signal in the scattering plane to a signal in the absorber plan. If there were signals produced in both planes almost instantaneously - in the order of the time of flight of an photon between the planes - the pair of signals is called a *coincident event* or simply a *coincidence*.

There are also detectors capable of reproducing the momentum direction of the scattered electron. This is for example achievable with multilayer Compton camera [Thirolf et al., 2016], a time projection chamber [Orito et al., 2003] or by a rather new approach which is trying to use the Cherenkóv effect of the recoil electron [Peterson et al., 2012]. The Cherenkóv effect occurs in materials for charged particles which move faster than the speed of light in this material. Similar to sonic cones, light is then emitted in a conical shape along the particles path. With the information of the recoil electron's momentum direction a scattering plane can be reconstructed which leaves only one possible incident photon direction on the reconstructed Compton cone. Because of the resolution of the system this is called the Compton arc as demonstrated for a multilayer Compton camera in Figure 2.1.2 (b).

## 2.2 Principle of a Directional Gamma Radiation Detector

In contrast to the classical Compton camera which is able of single photon reconstruction, the reconstruction by the Directional Gamma Radiation Detector is based on the distribution of energy spectra obtained from many coincidences. By definition a DGRD is a pair of detectors in one detection plane only [Gueorguiev et al., 2012a]. Rather than having a scattering and an absorption plane, each of the detectors serves as scatterer and absorber at the same time. For reconstruction, the energy sharing of coincident events from Comp-

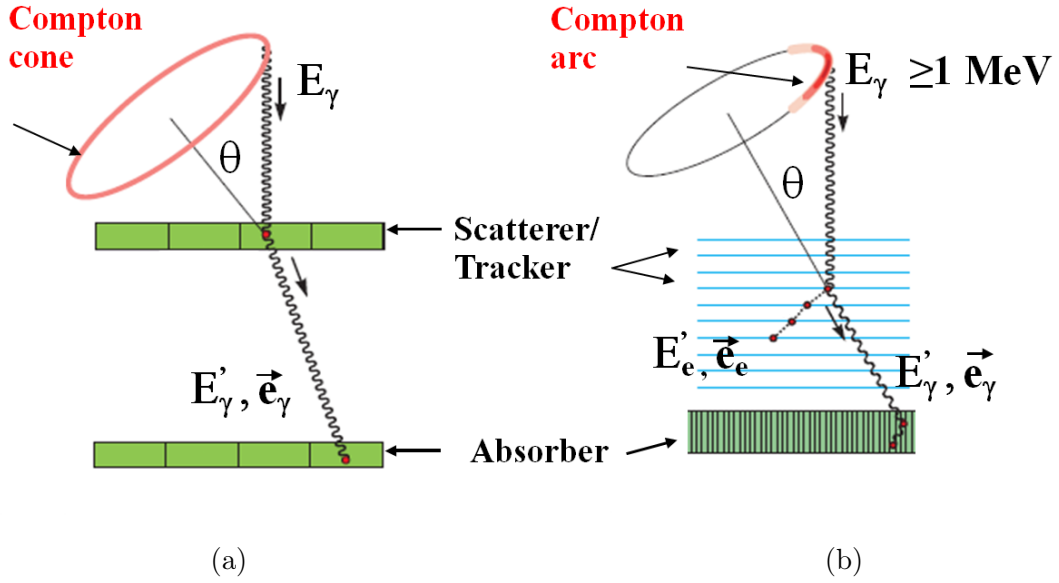


**Figure 2.1.2:** Reconstruction of a photon source by the Compton camera principle. Demonstrated are (a) single and (b) multiple scattering planes. The initial photon with energy  $E_\gamma$  is scattered in one of the scattering planes and absorbed in the absorber plane. The interaction points give the photon's direction  $\vec{e}_\gamma$ . In the multiple scattering plane also the electron's direction  $\vec{e}_e$  is measured. The reconstructed source position is indicated in red. (Adapted from [Thirolf et al., 2016](#))

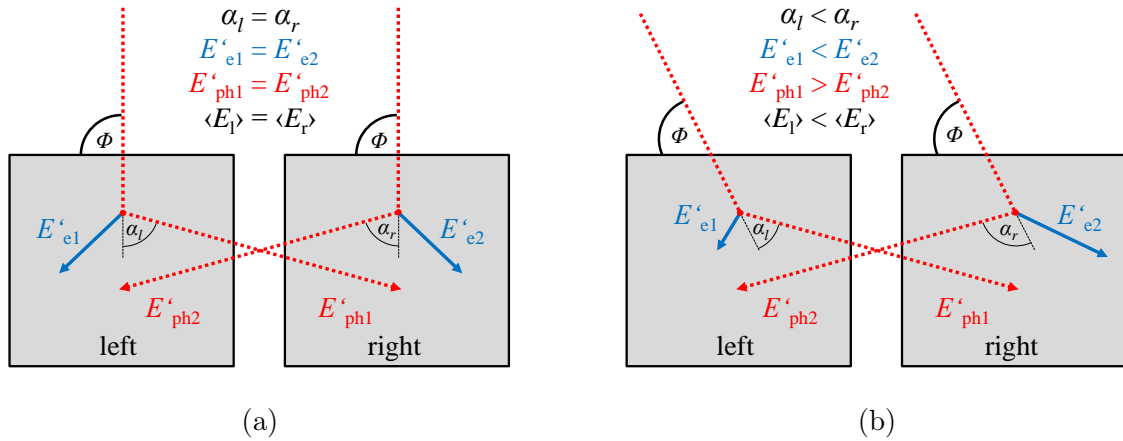


**Figure 2.2.1:** Principle of a Directional Gamma Radiation Detector. Exemplary visualization of coincident events from Compton scattering processes between a pair of detectors in the (a) symmetric and the (b) asymmetric case. The energy of the recoil electrons is labeled  $E'_e$  and for the scattered photons  $E'_{ph}$ , respectively. In the asymmetric case a coincident event from the scattering in the left detector will on average be scattered under a smaller angle  $\alpha_l < \alpha_r$  than an event from scattering in the right detector. Thus the photons scattered in the left detector carry on average more energy than the photons scattered in the right detector. (Adapted from [Gueorguiev et al., 2012a](#))

ton scattering between the two detectors is measured. A similar detector using adjacent layers of different detector materials for an angular resolution based on the energy sharing of the incoming gamma radiation has first been patented by [Enghardt et al., 2011](#).

In Figure 2.2.1, to describe the principle of a DGRD the two detectors are denoted *left*  $l$  and *right*  $r$ , respectively. In this consideration parallel and monoenergetic photons are assumed which can be characterized by the *angle of incidence*  $\phi$  to the plane of the detector pair. As mentioned, there is a chance of Compton scattering between the two detectors. In the simplest case the scattered photon is fully absorbed after a single Compton scattering. The resulting energy spectra  $E_r$  and  $E_l$  of such coincidences are then referred to as *conditional spectra* as the condition of single scattering in the one and full absorption in the other detector holds. Two different scenarios of the incident angle can be distinguished as visualized by Figure 2.2.1. In the symmetric case of perpendicular radiation, the conditional spectra are identical for each detector due to the symmetric Compton kinematics. Especially the “*allowed*” *scattering angles*  $\alpha$  leading to a coincidence are the same at each point in the left and the right detector, respectively. In the asymmetric case of non-perpendicular radiation the allowed scattering angles with respect to the initial photons’ direction are different for each of the mirrored positions in the detectors. Hence the shape of the conditional spectra will differ from each other. As the exact shape of the conditional spectra depends on the incident angle  $\phi$  of the photons it can be determined. So far this principle can be used for the localization of a point source under a certain angle. In more complex detector arrays with at least two perpendicularly aligned DGRDs this principle yields also reconstruction of a single source in more than one dimension. Such a detector is referred to as SPCC as suggested by the later proposal of a patent by [Gueorguiev et al., 2012b](#). But there is even an imaging potential for multiple sources. This is due to the fact, that the conditional spectra from different source positions add up linearly which makes a Maximum Likelihood Estimation Maximization (ML-EM) applicable for the reconstruction of an activity distribution. This method of Single Plane Compton Imaging (SPCI) with a SPCC was first proposed by [Pausch et al., 2016a](#) and will be shortly discussed in Section 2.3.

As one can imagine, the resulting conditional spectra depend not only on the activity distribution in the image space. The influence of two more effect - the emission spectrum and the detector composition - shall be briefly discussed. The emitted energy spectrum has an influence on the conditional spectra because the Compton effect is energy dependent. Figure 2.2.2 shows the resulting recoil electron’s and scattered photon’s energy, respectively, for different scattering angles and initial photon energies. It demonstrates, that for higher initial photon energies the relative energy transfer on the electron is much higher at

the same scattering angle. Besides, the Klein-Nishina formula prefers forward scattering of high energetic photons as already mentioned. The influence of the detector composition can be divided in two parts. The geometry determines the allowed scattering angles when thinking of the simple model of a single Compton scattering. The material of the detector defines the probability of Compton scattering for the incident photons and the photoelectric effect for the scattered photons.

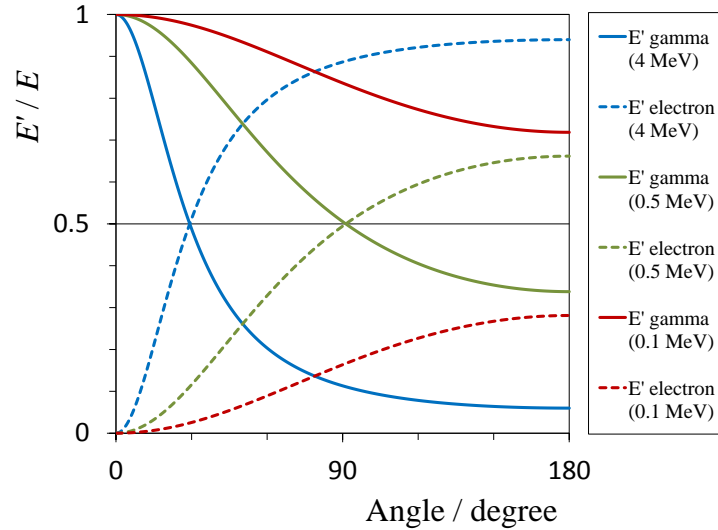


**Figure 2.2.2:** Ratio of the recoil electron's and the scattered photon's energy  $E'$ , respectively, to the initial photon's energies  $E$  (in brackets) for different scattering angles according to the Compton scattering formula in Equation 2.1.1.

### 2.2.1 The Figure of Merit as Measure

As the authors of the patent of a DGRD suggest, the effect of the incident angle  $\phi$  on shape of the conditional spectra can be quantified by the *difference of mean values*  $\Delta E$ . Denoting the *mean energy* of the left detector  $\langle E_l \rangle$  and of the right detector  $\langle E_r \rangle$ , the parameter  $\Delta E$  is defined as follows.

$$\Delta E(\phi) = \langle E_l \rangle - \langle E_r \rangle \quad (2.2.1)$$

In the following, this function is considered for events with constant *sum energy*  $e_0 = E_r + E_l$  which is for instance the case for Compton scattering followed by full absorption. From this concludes that the *mean sum energy*  $E_0 = \langle E_l \rangle + \langle E_r \rangle$  is also constant. Therefore the two variables  $\langle E_l \rangle$  and  $\langle E_r \rangle$  are not independent but correlated with a *correlation factor*  $\rho = -1$ . Because of this, the *statistical uncertainty*  $\sigma$  of the mean energy difference  $\sigma_{\Delta E}$  is determined by the following.

$$\sigma_{\Delta E} = \sqrt{\{\partial_{\langle E_l \rangle} \Delta E \cdot \sigma_{\langle E_l \rangle}\}^2 + \{\partial_{\langle E_r \rangle} \Delta E \cdot \sigma_{\langle E_r \rangle}\}^2 + 2 \cdot \partial_{\langle E_l \rangle} \Delta E \partial_{\langle E_r \rangle} \Delta E \cdot \text{Cov}(\langle E_l \rangle, \langle E_r \rangle)}$$
(2.2.2)

$$\text{Cov}(\langle E_l \rangle, \langle E_r \rangle) = \rho \cdot \sigma_{\langle E_l \rangle} \sigma_{\langle E_r \rangle}$$
(2.2.3)

With  $\partial_{\langle E_l \rangle} \Delta E := \frac{\partial(\Delta E)}{\partial \langle E_l \rangle} = 1$  and  $\partial_{\langle E_r \rangle} \Delta E := \frac{\partial(\Delta E)}{\partial \langle E_r \rangle} = -1$  concludes equation 2.2.5.

$$\sigma_{\Delta E} = \sqrt{\sigma_{\langle E_l \rangle}^2 + \sigma_{\langle E_r \rangle}^2 - 2 \cdot \rho \cdot \sigma_{\langle E_l \rangle} \cdot \sigma_{\langle E_r \rangle}}$$
(2.2.4)

$$\sigma_{\Delta E} = \sigma_{\langle E_l \rangle} + \sigma_{\langle E_r \rangle}$$
(2.2.5)

The uncertainty of the mean value is given by  $\sigma_{\langle E_{l/r} \rangle} = \frac{\sigma_{E_{l/r}}}{\sqrt{N}}$  where  $\sigma_{E_{l/r}}$  denotes the *standard deviation* and  $N$  the *number of coincidences* which is the number of entries in the conditional spectra. Hence Equation 2.2.6 is the derived formula for the statistical uncertainty of the mean energy difference.

$$\sigma_{\Delta E} = \frac{\sigma_{E_l} + \sigma_{E_r}}{\sqrt{N}}$$
(2.2.6)

By normalization of the mean energy difference to the corresponding sum energy  $E_0$  this function can be utilized as a so called *Figure of Merit (FOM)* (Equation 2.2.7).

$$\text{FOM}(\phi, E_0) = \frac{\Delta E}{E_0}(\phi) = \frac{\langle E_l \rangle - \langle E_r \rangle}{E_0}$$
(2.2.7)

By plotting the FOM at different sum energies it can thus be concluded which sum energy is more sensitive towards the direction of the source. The sensitivity of the FOM for different gamma lines is shown in Figure 2.2.3.

There are also other parameters that can quantify the change of the conditional spectra. One such parameter is the skewness which is more easy to be applied on the energy difference histogram  $\Delta e = E_l - E_r$ . A similar parameter is the ratio of the number of events where  $\Delta e < 0$  to the number of events where  $\Delta e > 0$ . It will be denoted as left/right count ratio in the following.

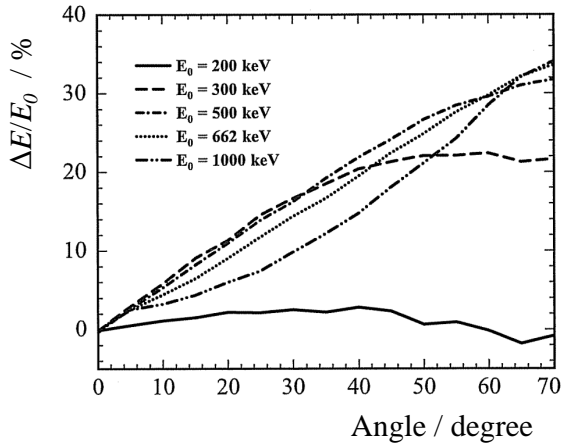


**Figure 2.2.3:** Figure of Merit (FOM) at various gamma-ray energies. Different incident angles lead to a variation in the mean energy difference between the two detectors. (Adapted from [Gueorguiev et al., 2012a](#)).

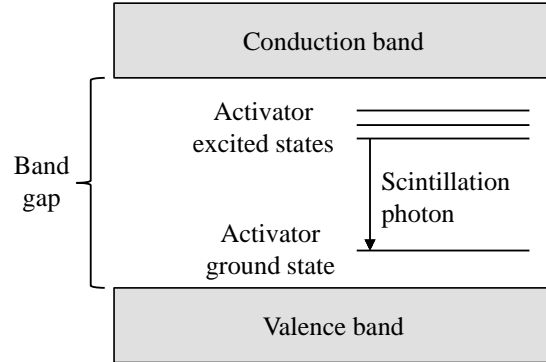


**Figure 2.2.4:** Energy band structure of an activated crystalline scintillator. Excited electrons get trapped in an excited activator state. After a certain decay time the electrons fall down to the ground state of the activator emitting a scintillation photon. (Adapted from [Knoll, 2010](#))

### 2.2.2 The Scintillation Mechanism in Inorganic Crystals

The principle of a DGRD can be easily realized using halide inorganic scintillation materials as they are able of both, sufficient timing for coincident detection and decent energy resolution for the conditional spectra (see section 3.1 for more details). Therefore the detection principle of inorganic scintillators shall be explained in this section. Detection of ionizing radiation by scintillation light is one of the oldest techniques on record. To understand the mechanism behind this, the energy states of electrons in the crystal lattice are to be considered. As materials are classified by their band gap between the valence band and the conduction band, electrons in an insulator can be lifted into the conduction band by an external energy transfer. Only then they can migrate through the crystal lattice; beforehand they are bound to the atoms. In the band gap between the two bands energies cannot be taken by the electrons. This means that on capture of electrons from the conduction band, they fall back in the valence band emitting a photon of just that energy difference. By excitation also so called excitons consisting of a bound state of an electron and a hole can be created which are able to freely move around in the crystal and also recombine by emitting a photon. These photons could be detected by a photosensitive detector. But there are two problems: the photon energy is often higher than of visible light and the absorption of such photons by other electrons in the valence band is very probable,



delaying the transmission through the crystal and thus enhance quenching effects.

These problems can be solved by adding small amounts of an impurity into the crystal in such a way, that the ground and excited state of these activator centers lie within the band gap as shown in Figure 2.2.4. This results in less self-absorption of photons from these transitions since the energy is too low to overcome the band gap. The lattice is so to speak transparent to this wavelength. In addition the emitted energy can be chosen to be a transition in the visible regime. On the one hand inorganic scintillators tend to be rather slow since their decay time of these activator states ranges typically from 30-500 ns, but on the other hand the light output is higher and the light yield is more proportional to the energy deposition observed in organic scintillators. [Knoll, 2010, p. 235 ff.]

## 2.3 Generalization of a DGRD: Single Plane Compton Imaging

The idea of a DGRD can be generalized to not only determining the direction to a source but also for an imaging modality. To achieve this the extension of a single DGRD to a two-dimensional pixel array, the so call SPCC, is needed. It is obvious that such a detector array can localize a point source by triangulation, using the directional information obtained by multiple pixel pairs. This principle could already be shown by other students', work namely that of Beyer, 2014 and Jannusch, 2014. As already mentioned, the keyword of advancing this principle to an imaging modality is Single Plane Compton Imaging (SPCI). Opposed to the determination of a point source by the FOM, this principle reconstructs the activity distribution in a defined image space. Therefore the image space is divided in small volumes called voxels. Each voxel of the image space contributes by linear superposition to the conditional spectra of a pixel pair. A potential ML-EM algorithm by Pausch et al., 2016a will be explained in the next paragraph (based on Vandenberghe et al., 2001 and Zeng, 2001).

This ML-EM algorithm is designed for an array of  $N$  detectors, e.g. scintillator pixels with individual readout arranged for instance in a checkerboard configuration like sketched in Figure 2.3.1. Considering events of pixel  $d$  ( $d = 1 \dots N$ ) and pixel  $c$  ( $c = 1 \dots N; c \neq d$ ), the term conditional spectrum  $S_{dc}$  refers to the energy spectrum  $E_d$  for events at which pixel  $c$  is coincident. Furthermore criteria for these coincidences like a condition on the sum energy  $E_\Sigma = E_d + E_c$  can be introduced. One condition could for instance be that  $E_\Sigma = const.$  representing the energy of a certain photo peak. Though adjacent pixel pairs contribute the most, all other combinations of conditional spectra are also possible holding

$\frac{1}{2}[N \cdot (N - 1)]$  pairs. The conditional spectra are described by the entries in each bin  $N_{dcb}$  with the bin index  $b$  which are following Poisson statistic. The image space with  $\nu$  voxels on the other hand is contributing to these bin contents depending on their activity distribution  $A_\nu$  and the probability  $p_{dcb\nu}$  of a single photon emitted from voxel  $\nu$  to raise the bin content of  $N_{dcb}$  by one. Thus the bin contents of the conditional spectra result from the sum over the activity of all voxels with respect to the probability of contribution:

$$N_{dcb} = \sum_{\nu} \{A_{\nu} \cdot p_{dcb\nu}\} \quad (2.3.1)$$

For reconstruction, the elements of the projection matrix  $p_{dcb\nu}$  need to be obtained by a voxel-by-voxel measurement or modeling. A ML-EM algorithm can then be formulated straight forward. Starting with a homogeneous activity distribution  $A_{\nu}^0$ , the real distribution is iteratively reconstructed by applying the following formula.

$$A_{\nu}^{k+1} = A_{\nu}^k \cdot \sum_{dcb} \left\{ p_{dcb\nu} \cdot \frac{N_{dcb}}{\sum_{\nu'} [A_{\nu'} \cdot p_{dcb\nu'}]} \right\} \quad (2.3.2)$$

That this reconstruction algorithm in principle works has been demonstrated by [Schulz, 2015](#). As a result, the iterative reconstruction of two separate point sources of equal energy could be shown. This demonstrates the potential of such a detection system for nuclear medical imaging. Also, such a system could in principle be applied for range and perhaps dose verification in proton therapy. For this a future task might be the adoption of the algorithm to higher multiplicity of coincidences caused by multiple Compton scattering. It has yet to be discovered whether the statistics from a single spot will be enough to reconstruct the Bragg curve.

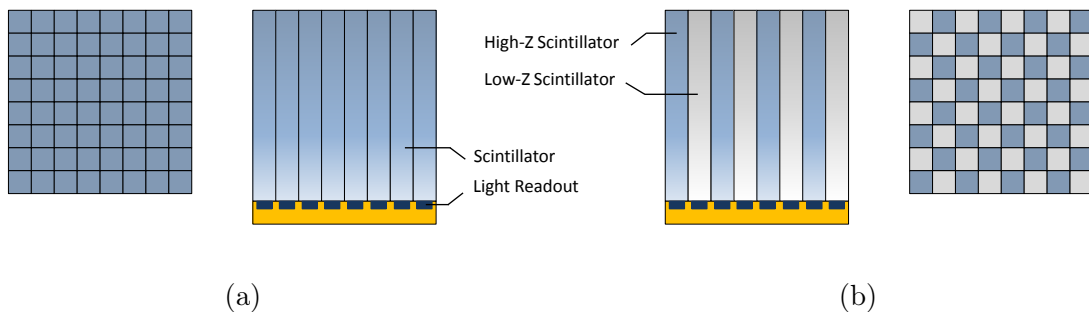


**Figure 2.3.1:** Checkerboard setup of scintillation materials for a SPCI detector from top and in profile. The material composition can either be (a) homogenous or (b) alternating to gain a higher efficiency for Compton scattering in between the pixels. (Courtesy to [Pausch et al., 2016a](#))

## 3 A Proof-Of-Principle Experiment

The aim of the performed experiment is to evaluate if the principle of a DGRD can be transferred to typical prompt gamma energies and may even be used for range verification in proton therapy. In this chapter the detection system is characterized and the conduction of the proof-of-principle experiment is described.

### 3.1 Characterization of the Detection System

The detection system for the used DGRD is based upon the scintillator material cerium bromide ( $\text{CeBr}_3$ ). It was chosen, as detectors using  $\text{CeBr}_3$  are already present in the field of range verification for PGT because of their excellent timing properties (resolution  $\Delta T = 189 \text{ ps}$  at  $4.4 \text{ MeV}$  [Roemer et al., 2015]). With a rise time of less than  $1 \text{ ns}$  and a decay time of about  $17\text{-}24 \text{ ns}$   $\text{CeBr}_3$  is one of the fastest inorganic scintillators [Schmall et al., 2015]. Also the light output of about  $60 \text{ photons/keV}$  is high compared to that of Sodium Iodide ( $\text{NaI}$ ) which is the gold standard in nuclear medical imaging. Advantageous is an energy resolution of less than  $5 \%$  at  $662 \text{ keV}$ . From the parametrization of Roemer et al., 2015 the energy resolution at  $4.44 \text{ MeV}$  can be extrapolated to  $2.5 \%$ . The cross sections for the main photonic interactions in  $\text{CeBr}_3$  are shown in Figure 3.1.1. The dominant effect in the energy range of  $0.3 - 7 \text{ MeV}$  is Compton scattering which covers most of the prominent prompt gamma-ray lines.

To fully exploit the potential of  $\text{CeBr}_3$  a photon-read-out with a high quantum efficiency is needed, as well as a spectrometer with brilliant behavior towards timing. The light readout is accomplished via an R13089 or R13089-100 magnetically shielded Photomultiplier Tube (PMT) from Hamamatsu<sup>1</sup>. The spectrometer U100 by *Target Systemelektronik*<sup>2</sup> is uniquely tailored to the needs of PGT. It has a very good timing resolution of approximately  $170 \text{ ps}$  with a  $\varnothing 2'' \times 1''$   $\text{CeBr}_3$  crystal and holds a throughput of up to  $1 \text{ MHz}$  (fix dead time of  $1 \mu\text{s}$ ). Latter is important to collect a high number

---

<sup>1</sup><http://www.hamamatsu.com/>

<sup>2</sup><http://target-sg.com/>

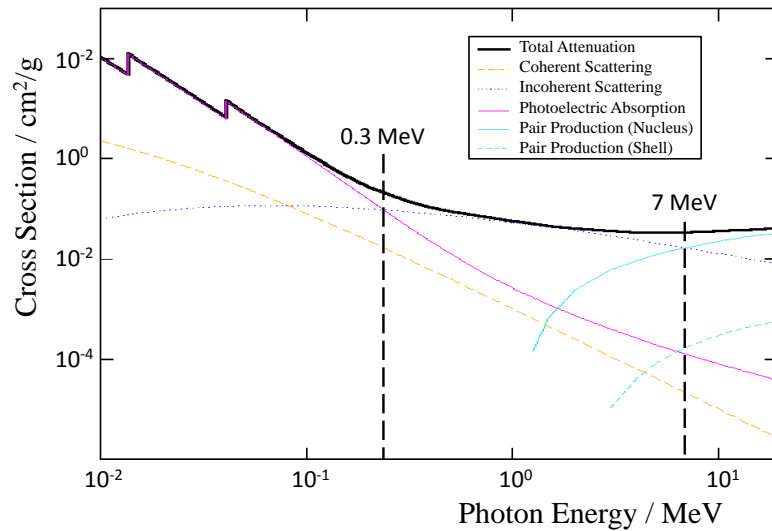


**Figure 3.1.1:** Photonic interaction cross sections of  $\text{CeBr}_3$  in the energy region of interest for prompt gamma radiation. The dashed black lines indicate the dominant region of Compton scattering. (from XCOM database [Berger et al., 2010])

of valid events under clinical conditions. The U100 can be plugged onto a standard 14-pin connector. This connector is provided by the PMT within a housing of Scionix<sup>3</sup> which also contains the scintillator. The digital spectrometer U100 converts signals via free-running Analog-to-Digital Converter (ADC) sampling the signals at a rate up to  $2 \times 310 \text{ MHz}$ <sup>4</sup> in 14 bit resolution. An event in the listmode data stream already contains the time stamp and the integrated charge with base line correction, corresponding to the energy deposition in the crystal. The recent firmware 20.18.2 offers particle identification via pulse shape discrimination in a phoswich detector. The power supply and data transfer is managed via Ethernet. By adjusting the high voltage (HV) up to 1.5 kV on the PMT the dynamic energy range of the device is set. Figure 3.1.2 shows the hardware components and ports of the U100. For more details see Pausch et al., 2016b.

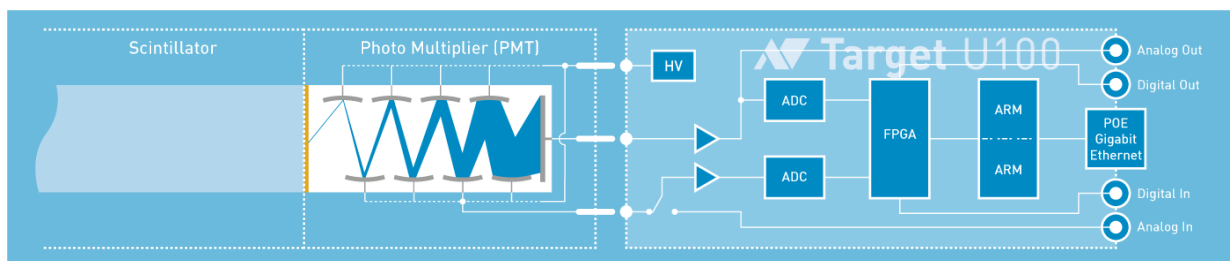


**Figure 3.1.2:** Schematic sketch of the hardware and ports of the U100. [Target, 2018]

<sup>3</sup><https://scionix.nl/>

<sup>4</sup>The U100 is equipped with two ADCs. Only one is used with the current design.

The precise timing of the U100 is optimal for a DGRD as the timing resolution for coincidences is enhanced. Between two of such detection units with  $\varnothing 2'' \times 2''$  CeBr<sub>3</sub> as scintillator, PMT and U100 for readout, the timing resolution has been determined to  $\Delta T \approx 0.8$  ns for 511 keV photons from Na-22  $\beta$ -decay. This has been done for different lengths of the synchronization cable in between the two detectors where one served as master clock with 13 MHz and the other as slave. Internally the U100 divides this frequency to  $2.12992 \times 10^{11}$  time stamps per second. As shown in Figure 3.1.3, the different *cable lengths*  $l_{sync}$  change the offset of the time stamps between the detectors because of the transit time of the sync signal. The plot therefore shows that the time synchronization is working as expected.

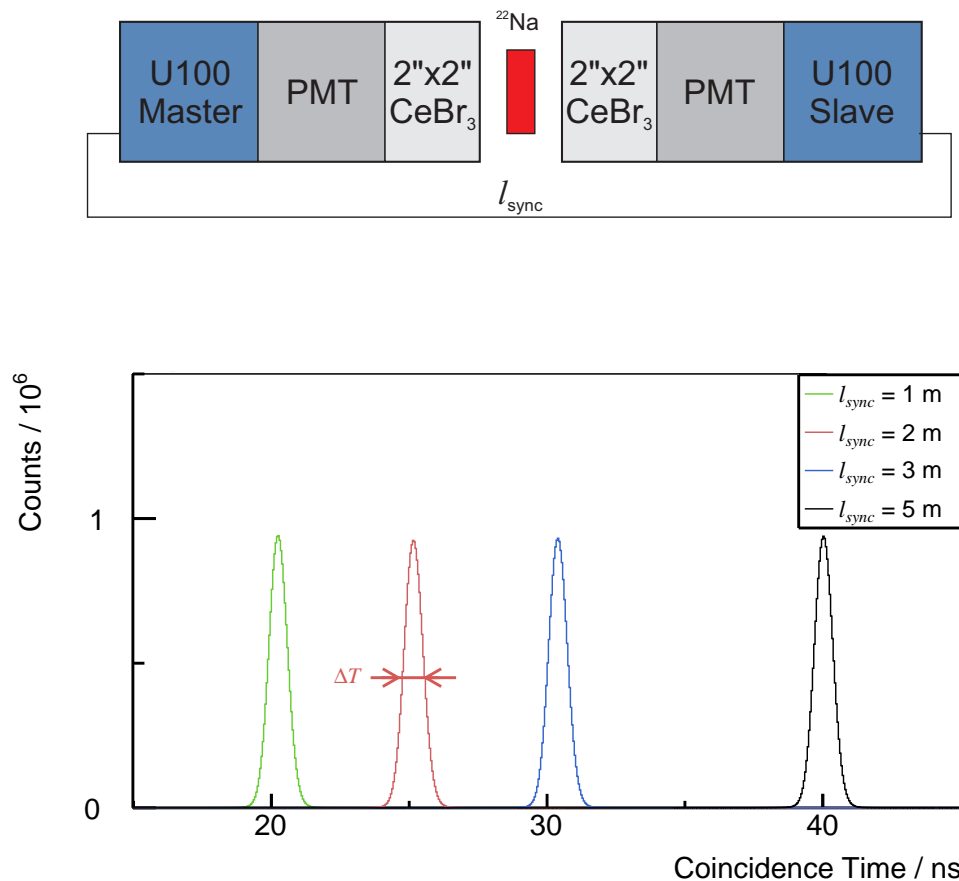


**Figure 3.1.3:** Coincidence time of two U100 detection units coupled to  $\varnothing 2'' \times 2''$  CeBr<sub>3</sub> scintillators with different cable lengths between the spectrometers. The two annihilation photons of a <sup>22</sup>Na source were detected by two the detectors.

### 3.2 Benchmark of the Detection System

In analogy to [Gueorguiev et al., 2010](#) an experiment has been performed with the detectors standing head-to-head. The  $^{22}\text{Na}$  source could be positioned around the detection unit at different angles as shown in Figure 3.2.1.

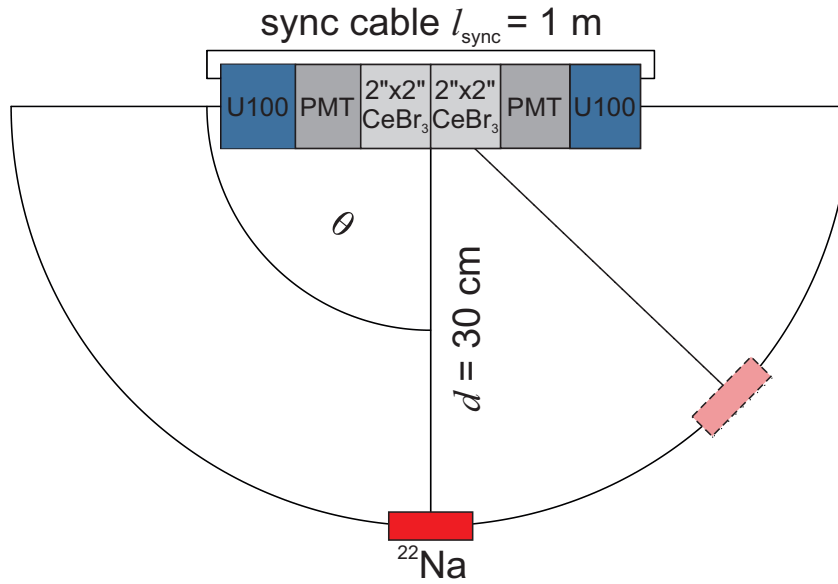


**Figure 3.2.1:** Setup of the benchmark experiment for the detection system. The source position can be rotated by the angle  $\theta$  to the plane of the detection system.

The  $^{22}\text{Na}$  standard radioactive source emits gamma photons with energies of 511 keV and 1275 keV. For different angles of the source, coincidences from Compton scattering between the detectors of these gamma-ray lines are detected. During offline analysis of the listmode data these coincident events are ascertained as described in Section 4.1. The FOM (see Section 2.2.1) for the two different sum energies is presented in Figure 3.2.2. It can be seen, that the resulting curve can be parametrized as described by [Gueorguiev et al., 2010](#). This is proving, that the introduced detection system is indeed a DGRD. Also it can be denoted, that for 1275 keV the angular dependency of the FOM is less than for 511 keV. When extrapolating this principle to proton therapy it has to be considered that there is no point source present but a distributed source. Furthermore, the emission spectrum at each point of the source is differing as the nuclear cross sections vary. The idea and setup of a prove-of-principle experiment is described in the next section.

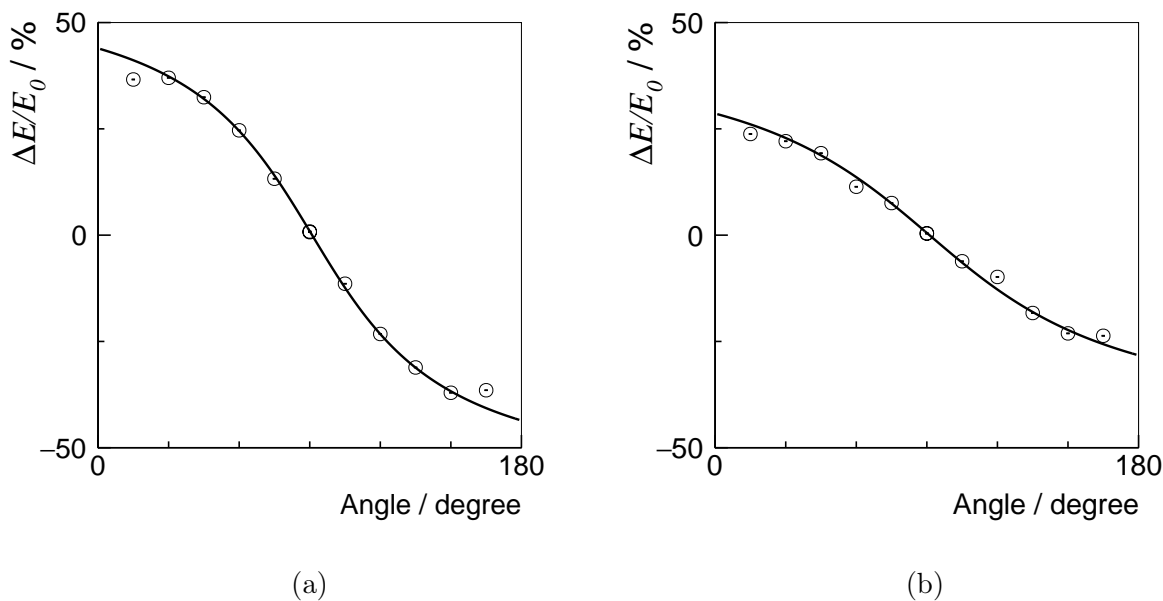


**Figure 3.2.2:** FOMs of a Na-22 point source for sum energy condition of (a) 511 keV and (b) 1275 keV, respectively. The fit is parametrized according to [Gueorguiev et al., 2010](#). Uncertainties can barely be seen.

### 3.3 Setup at the Experimental Beam Line of OncoRay Dresden

Task of the experiment is to figure out if a DGRD can be used for range verification in proton therapy to eventually develop a SPCC. This is motivated by the fact, that the direction of a point source can be determined by a DGRD. In the case of proton therapy there is a patient from whom prompt gamma radiation is emitted along the intruding beam's path. It is expected that a change in range of the beam can be monitored when a stationary detector setup as described above is used. This corresponds to the changed activity distribution with respect to the detection unit. The effect would manifest in a changed shape of the coincident energy spectra. For a prove-of-principle experiment a full PMMA target is positioned along the proton beam in a way that the proton beam is fully stopped inside. With detection units parallel to the beam axis a series of measurements is performed. Two types of detectors were used as demonstrated in Figure 3.3.1 which shows the experimental setup. One detection units was equipped with  $\varnothing 2'' \times 1''$  and the other one with  $\varnothing 2'' \times 2''$  CeBr<sub>3</sub> crystals.

At the OncoRay Dresden there is the proton facility Universitäts Protonen Therapie Dresden (UPTD). The UPTD is equipped with an isochronous cyclotron of 106 MHz

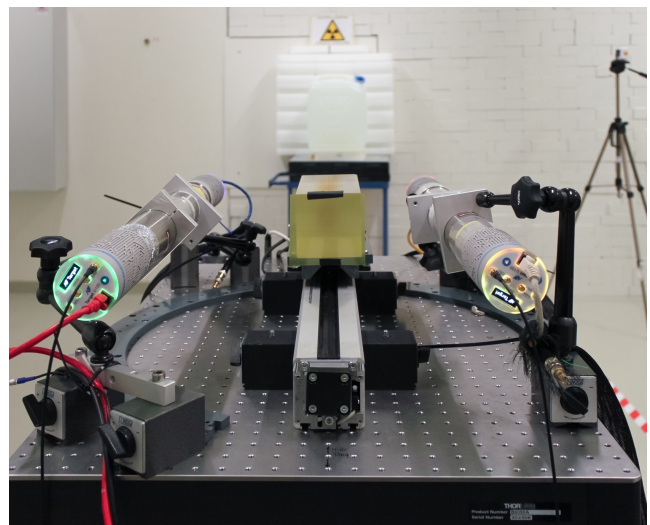
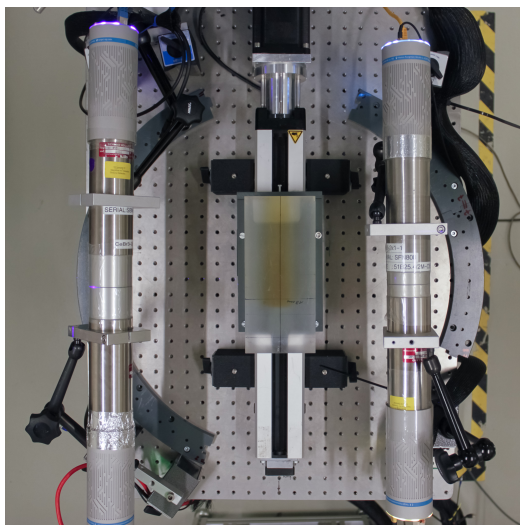
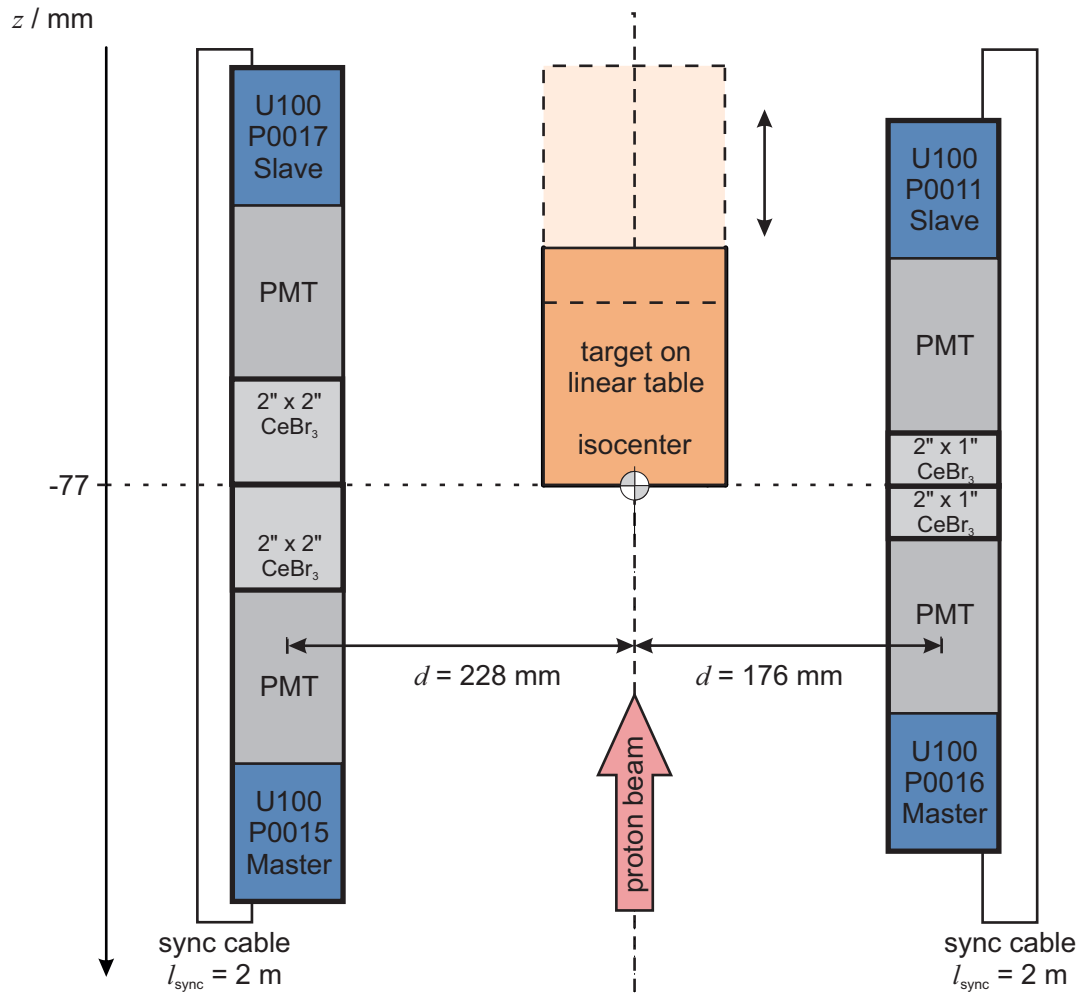


**Figure 3.3.1:** Sketch and photographs of the proof-of-principle experimental setup. The detection units and the PMMA target in the proton beam line can be seen from above. The right picture shows the setup from the perspective of the beam nozzle.



operated and built by *IBA*<sup>5</sup>. The kinetic energy of the protons extracted from the cyclotron is constantly about 230 MeV. Via a Degradar and an Energy Selection System (ESS) the proton energy is reduced discretely to energies as low as 70 MeV. An overview of the accelerator system and the beam lines of the UPTD is given in Figure 3.3.2.

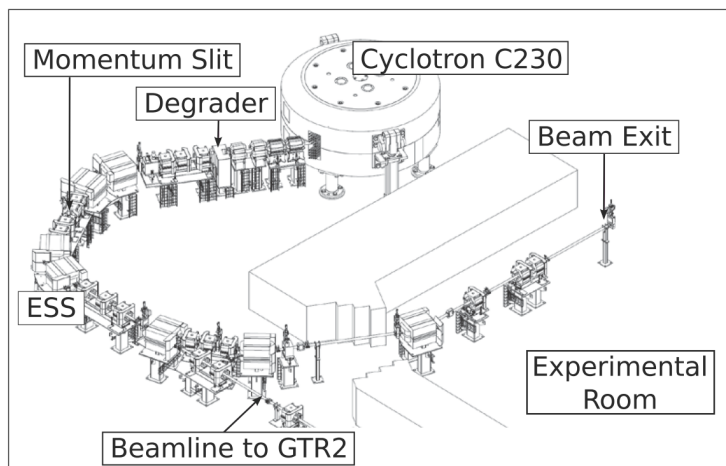


**Figure 3.3.2:** Sketch of the cyclotron and beamline at the UPTD. The gantry treatment room (GRT2) is not displayed. (Courtesy of [Petzoldt et al., 2016](#))

Using the experimental setup described above, the following measurements were performed at the experimental fix beam line: For two different proton energies the position of the linear table with the PMMA target was varied, changing only the relative position of the activity distribution to the detectors. In another series the setup was fix, changing the energy of the intruding proton beam and thus the range in the target. For this series the activity distribution along the  $z$ -axis is not only shifted but completely changed. Both cases should have a similar effect on the FOM and correspond to clinical situations, namely positioning and change of tissue density. An overview of the performed measurement series is given in table 3.3.1.

**Table 3.3.1:** List of all performed measurements of the proof-of-principle experiment.

Measurement Series	Beam Energy / MeV	Position linear Table / mm
(1) fix energy	90	-77 - 23
(2) fix position	90 - 110	-12
(3) fix energy	150	-77 - 23

<sup>5</sup><https://iba-worldwide.com/>



## 4 Methods for Data Analysis

The analysis of the experimental data can be divided into individual steps. The first step is the offline matching of coincident events from the listmode data and the second step is the energy calibration for each measurement. This chapter describes the algorithms performing these analyses and introduces a method for studying random coincidences.

### 4.1 A General Algorithm for Finding Coincidences

The task of the offline analysis is to find coincidences in the listmode data produced by the detection system. The algorithm used for this is going through all events chronologically. In principle it may be extended to any number of channels and even consider an offset between the clocks of different entities. At the beginning of this algorithm an array is filled with the first recorded time stamps of each detector. Afterwards it is checked, if these *time stamps*  $T$  are lying within a given coincidence time window. If yes, the time stamps are kept. Then the entry of the channel with the smallest time stamp is replaced by the time stamp of the next event in that channel. Again the coincidence of this tuple is checked. This is repeated as long as events exist for any channel. As of now, in the case of two or more possible coincidences for one time stamp of a channel, all the possible coincidences are discarded. This never happened for the coincidence time window applied in the analysis of the presented experiments. The principle of the algorithm is shown by a structure chart in Figure 4.1.2 (a) and by an example in Figure 4.1.1 (a).

For the analysis of the coincident energy spectra not all of these coincidences are selected. Only those that are situated in a  $4\sigma$  region around the coincidence time peak are being used further. That way also a region of the same time interval can be defined in the coincidence time spectrum, where only random coincidences occur. This is used for background subtraction in later analysis steps. As for some of the following plots of the analysis in this chapter, the coincidence time interval is shown exemplary in Figure 4.1.1 (b) for detectors 15 and 17 for one specific measurement.

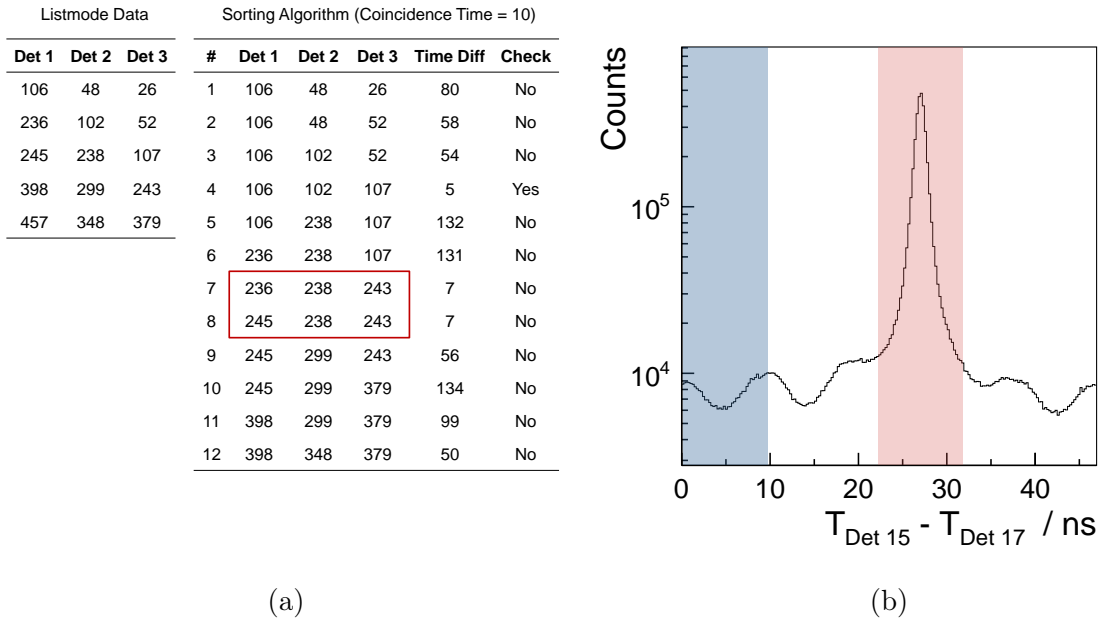


**Figure 4.1.1:** Principle of the offline coincidence algorithm.

(a) Visualization of the coincidence algorithm for a random set of listmode time stamps. For each step of the algorithm another column is updated and the resulting tuple is checked for coincidence from its time difference and uniqueness. As of now, during the algorithm multiple coincidences, indicated by the red box, are discarded.

(b) Coincidence time window for the coincidence peak (red) and a random background cut (blue). The non-constant background is the result of a known non-physical effect of the digital timing algorithm [Werner et al., 2019]. The width of the coincidence peak window was selected  $4\sigma$  so this periodical effect is represented by one period in the background window. The background-to-peak ratio without an energy cut is about 6%.

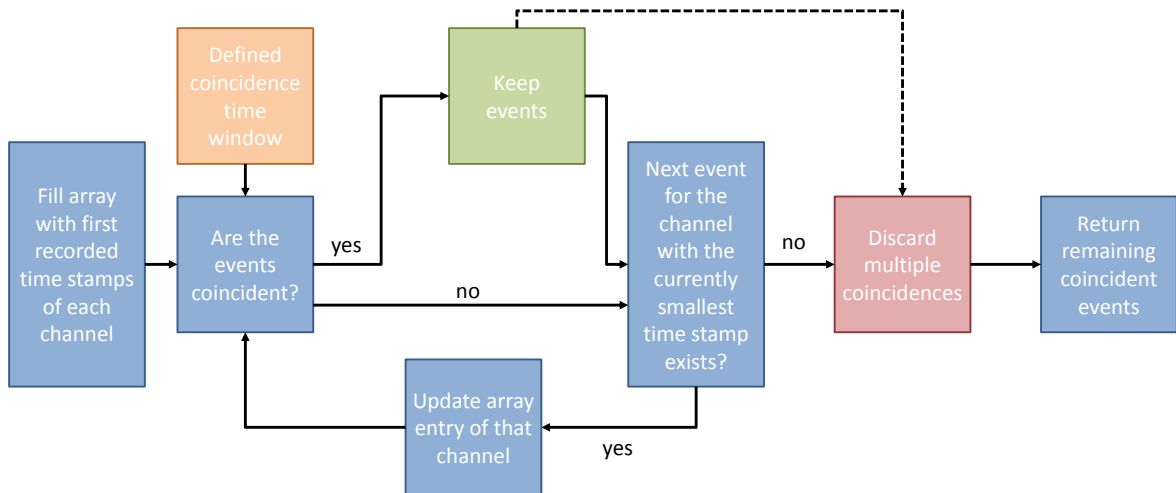


**Figure 4.1.2:** Structure chart of the offline coincidence algorithm.

## 4.2 The Bootstrapping Method for Energy Calibration

The energy calibration for each individual measurement file is necessary for the present detection system since the gain of the PMTs depends on the detector load [Küchler, 2017, Müller, 2017] and environmental conditions (temperature, magnetic field, etc.). For the consideration of a DGRD not the absolute energy calibration but the relative energy calibration is uttermost import. Mainly for this reason and because of the difficulty to determine the systematic uncertainty of the peak calibration, it was decided to use a spectrum matching method for the calibration of the different detectors. This could be achieved by applying a technique called Bootstrapping. Bootstrapping is a statistical method to simulate multiple sets of measurements by randomly drawing events from a given measurement. In the current application it is used as part of an offline template matching algorithm [Kong et al., 2010] which matches different energy spectra by varying the gain factor of the detectors. Bootstrapping is very useful to estimate the error on this gain factor and its exact value.

For the template matching the gain factor is varied by rescaling the measured energy spectrum according to the areal overlaps of the old and new binning as shown in

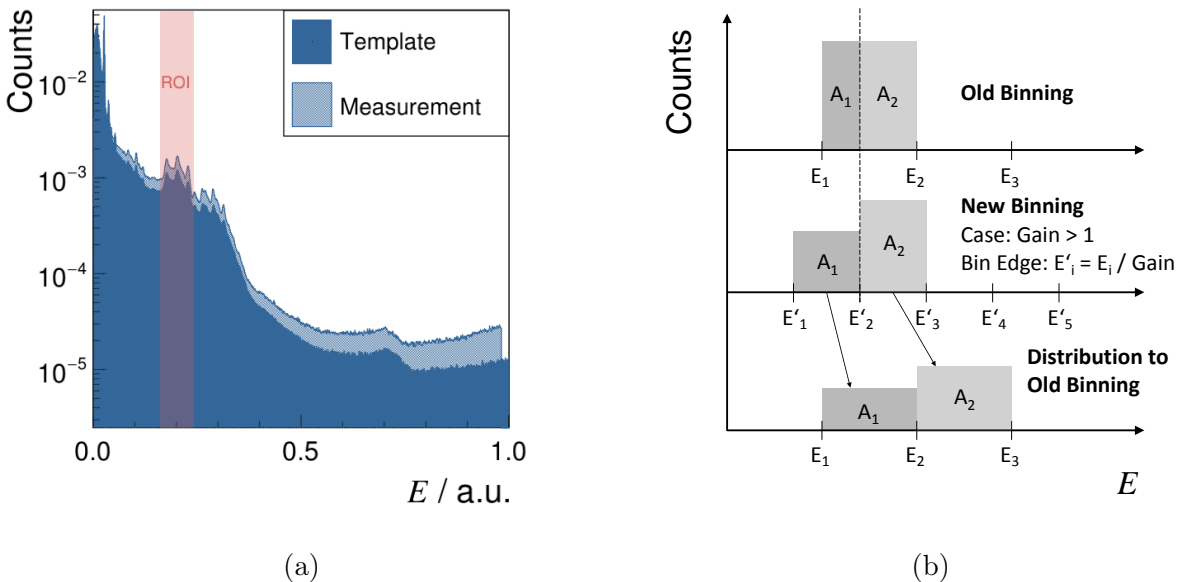


**Figure 4.2.1:** Demonstration of the rebinning algorithm.

(a) Rebinned measurement with the gain factor calculated from bootstrapping in the introduced Region of Interest (ROI). Within the ROI there is the full energy, the single and double escape peak of the 4.4 MeV gamma-ray line.

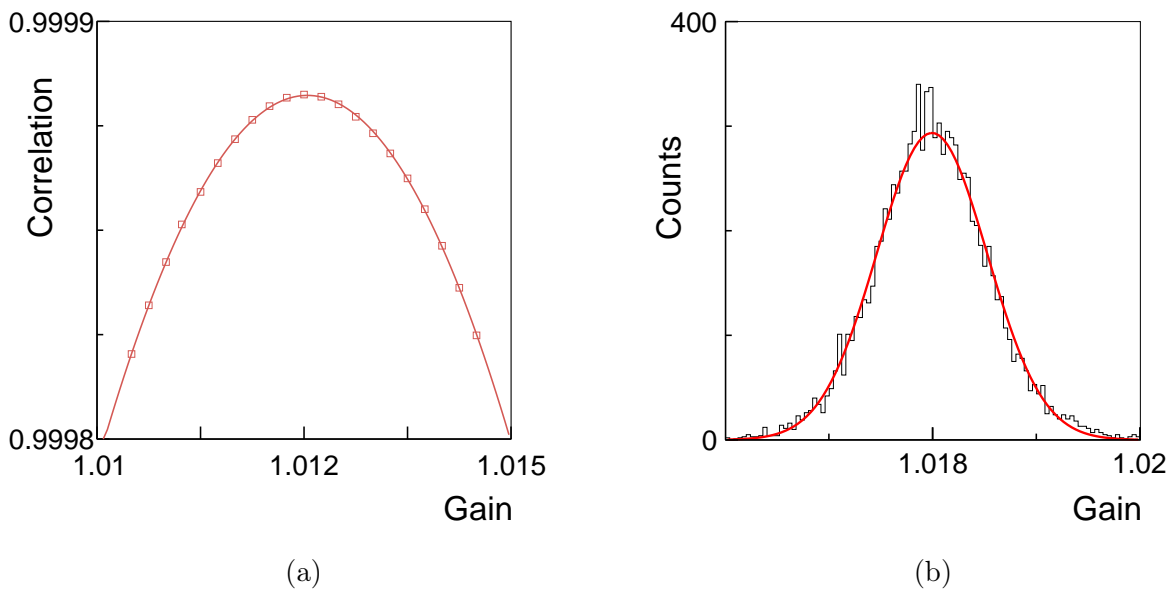
(b) Visualization of the analytical rebinning algorithm of a histogram with a gain factor. (Adapted from Knoll, 2010, p. 724)

Figure 4.2.1 (b). It is then important to define a variable, which is dependent on the gain factor and can therefore be maximized or minimized in the progress. In reference to [Kong et al., 2010](#) the correlation factor of the bin contents between the template and the measurement is used. Each bin in a defined Region of Interest (ROI) contributes to this correlation factor. For this work the ROI was chosen to be the 4.4 MeV structure in the energy spectrum as seen in Figure 4.2.1 (a). Let  $t_i$  be the bin content of bin  $i$  of the template and  $m_i$  be the bin content of the same bin of the gain varied measurement, then the correlation factor  $c(\textit{gain})$  of all bins in the ROI is defined as:

$$c(\textit{gain}) = \sum_i^{(ROI)} \frac{t_i \cdot m_i}{\sqrt{\sum_i^{(ROI)} t_i^2 \cdot \sum_i^{(ROI)} m_i^2}} \quad (4.2.1)$$

By varying the gain factor a value can be found at which the correlation is maximal. Bootstrapping means doing this not just once but for a number of repetitions. At each repetition the bins in the ROI are weighted randomly. So with Bootstrapping, for each bin a weight  $w_i$  is introduced to the formula above. In this manner a transformation  $t_i \rightarrow w_i \cdot t_i$  and  $m_i \rightarrow w_i \cdot m_i$  is performed. Furthermore the condition  $\sum_i^{(ROI)} 1 = \sum_i^{(ROI)} w_i$  holds. The core of bootstrapping is to shuffle these weights and recalculate the gain factor for each set of weights. An easy way to achieve this is to only allow natural numbers as weights. That way, for each set one can randomly draw bins within the ROI. To hold the condition above, the amount of draws must be the same each time, namely  $\sum_i^{(ROI)} 1$ . Any bin within the ROI can be drawn multiple times. Therefore some bins will not be drawn and others two or more times resulting in a weight of zero, two or more, respectively. The calculation of the resulting gain factor for each set of weights is done by a rough and a fine stepping. The exact value is taken from a parabola fit around the global maximum. An example of this is given in Figure 4.2.2 (a). This is repeated several times and the maximum of each iteration is filled in a histogram. The result is a Gauss like distribution of the gain factor. From this one can draw the mean value and the sigma for an uncertainty estimation. An example of such a distribution is shown in Figure 4.2.2 (b) with 10.000 random sets of weights.

For consistency studies, the Bootstrapping method is compared to a least-square fit routine of the ROOT analysis framework [[Brun and Rademakers, 1997](#)]. From the graphs in Figure 4.2.4 can be seen, that the gain correction factors are in great consistency but the uncertainty of the fit is unknowingly jumping between different measuring points. The methods need to be compared for the case of matching the template spectrum on itself. The best method would give a gain correction equal to one and a minimal uncertainty.



**Figure 4.2.2:** Progress graphs of the Bootstrapping algorithm. (a) Correlation factor over gain factor with parabola fit. (b) Maximal Gain factor from parabola for 10,000 repetitions with Gauss fit.

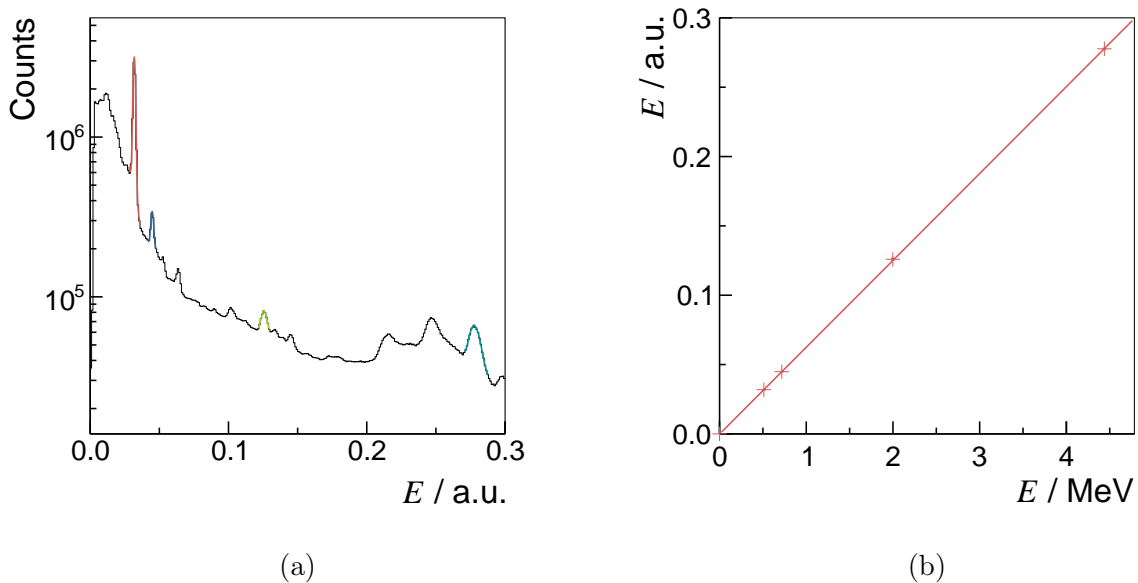


**Figure 4.2.3:** Energy calibration of the template spectrum. (a) Peak fit of the template spectrum for selected gamma lines. (b) Energy calibration function.

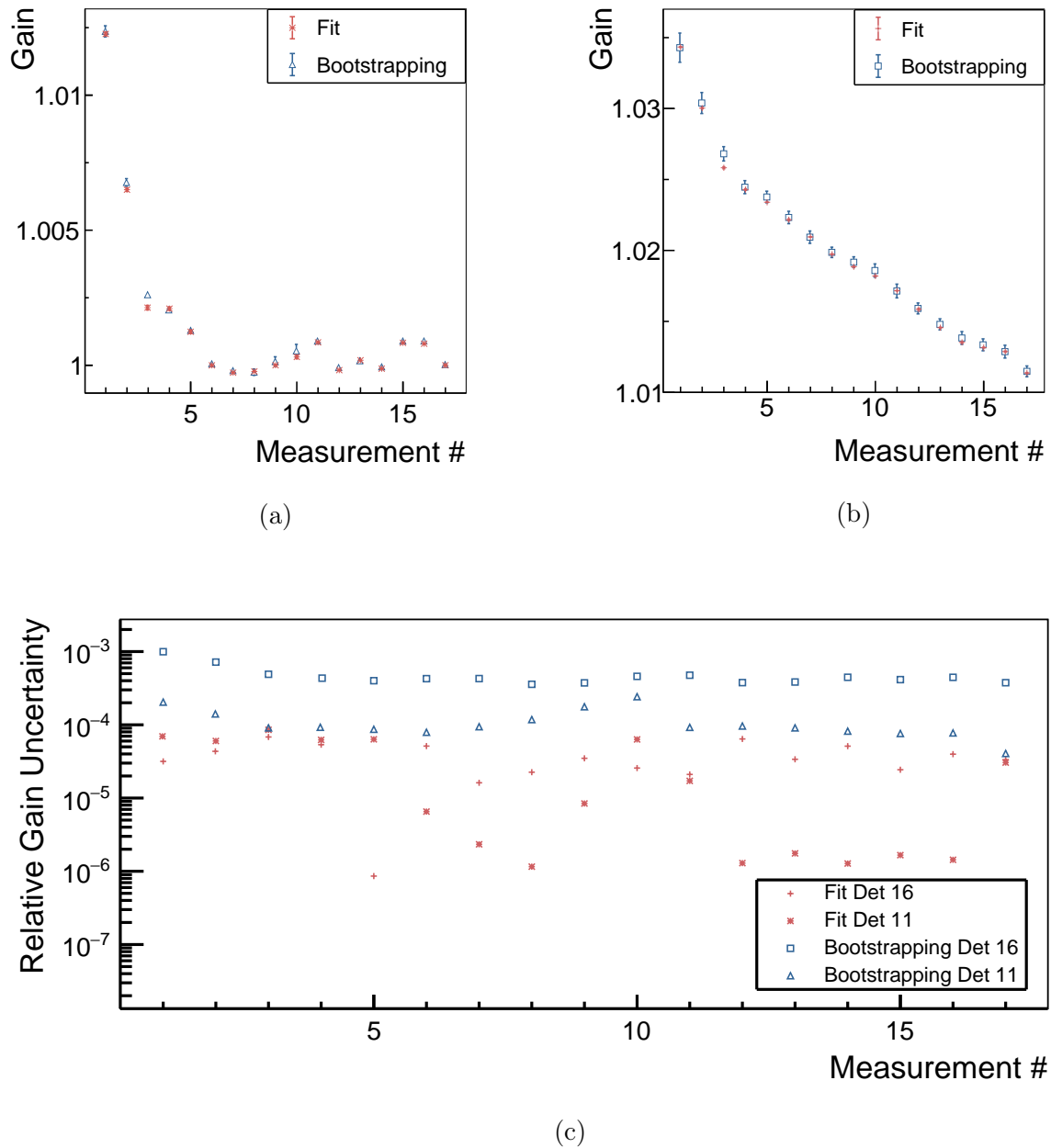


**Figure 4.2.4:** Exemplary comparison of the described Bootstrapping method to a conventional least-square fit. In the top row the gain factor is plotted for each measurement point of (a) detector 11 and (b) detector 16. (c) The relative gain uncertainty to these measurement points is shown. Template spectrum for both detectors is the last measurement point (# 17) of detector 11 (a).

The template spectrum for this series is the last measurement point for detector 11. In comparison to the uncertainty of the other measurement points the Bootstrapping method holds more realistic estimations for the template. Therefore Bootstrapping is chosen in



this work for relative energy calibration. With this method a relative uncertainty of 0.1 % and less is achieved. Also the template spectrum is calibrated to an absolute energy scale by peak calibration which is shown in Figure 4.2.3.

### 4.3 Combinatorial Study on Coincidences

The idea of the combinatorial study of the coincidences arises from the two-dimensional energy plots. In these histograms the energy deposition in each of the detectors  $E_r$  and  $E_l$  for coincident events is shown. There are two types of coincidences occurring in the experiment. At first there are *uncorrelated coincidences* appearing randomly in time from any two particle. The first particle is hitting the one and the second particle the other detector simultaneously. Secondly, *correlated coincidences* occur when a physical process causally leads to a simultaneous detection in both detectors. In the present experiment such correlated coincidences can be caused by Compton scattering as discuss in Section 2.2 and also by pair production. During pair production a positron and an electron is produced by a photon of at least 1022 keV - which is the energy of the rest mass of two electrons - inside one of the detectors. In the presence of the orbital electrons of the scintillator the positron then annihilates emitting two 511 keV photons at an angle of  $180^\circ$ . If one of these photons is detected in the other detectors this leads to a correlated coincidence. The other photon can either be detected in the first detector or escape. The correlated coincidences lead to a peak in the coincidence time as seen in Figure 4.1.1.

The two-dimensional energy histograms from the coincidences of the coincidence peak and the background window of a measurement are shown in Figure 4.3.1 (a). For the coincidences peak one finds clear evidence for a correlation between the energy deposition in both detectors. Especially in the case of Compton scattering and full absorption of a discrete gamma line. For this the correlation factor  $\rho = -1$  which can be seen from the clustering of descending diagonal lines. Coincidences from pair production can also be seen by the vertical and horizontal lines at 511 keV. This is due to the necessary detection of a 511 keV photon in one of the detectors. Looking at the energy spectrum of background window, there is no evidence for correlation from Compton scattering. The vertical and horizontal lines at 511 keV are cannot result from pair production in the detectors but from the random detection of a 511 keV photon. To validate that there is no correlation, it shall be studied if the displayed histogram of the background window is due to combinatorial detection of random events.

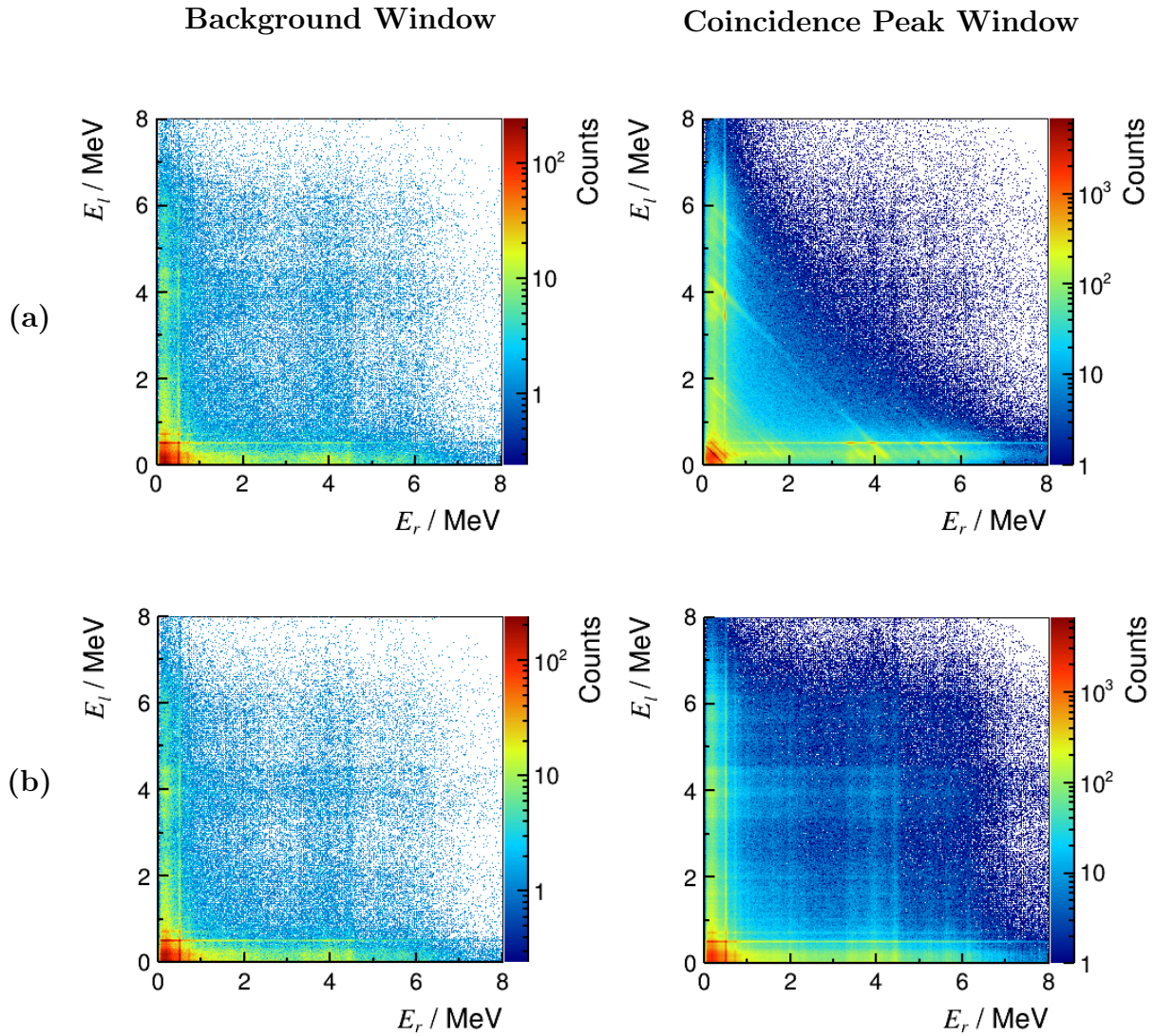


**Figure 4.3.1:** Two-dimensional energy histograms of prompt gamma radiation for coincidences from different coincidence time windows. (a) Measurement showing events from different time windows according to Figure 4.1.1. (b) Random reconstruction of events from the projections of the measured two-dimensional histograms displayed in (a).

The combinatorial study is performed by simply drawing random pairs of energy ( $E_r, E_l$ ) from the single detectors. The random selection of these energies follows the probability distribution of the energy spectra  $E_r$  and  $E_l$  of the single detectors. These spectra do not contain information on the correlation and are derived as projections of the two-dimensional energy histogram - background and coincidence peak, respectively. If produced by just combinatorics, then the two-dimensional energy histogram of the randomly drawn pairs of energy should look alike the original measured distribution. For comparison the total number of coincidences is of course the same as in the measured histogram. The

combinatorial two-dimensional energy histograms are shown in Figure 4.3.1 (b). Therefrom can indeed be verified, that the coincidences in the background window results from the random selection of energies. The combinatorial two-dimensional histogram of the coincidence peak does not match the measurement. The information of the correlation from events of Compton scattering and pair production is lost in the combinatorial recombination of the energy pairs.

This analysis shows, that correlated coincidences are only contained by the coincidence time peak. Furthermore it is now justified to subtract the uncorrelated coincidences of the background window from the coincidence peak window. By this means, the resulting two-dimensional energy histogram will just contain correlated coincidences due to Compton scattering and pair production. It can therefore be concluded, that the correlated coincidences can be obtained in the analysis.

In further steps the correlated coincidences are classified according to the sum energy  $E_0 = E_r + E_l$ . Events of a specific sum energy  $E_0$  must not only result from photons of energy  $E_0$ . Also more energetic gamma photons can lead to a coincidence with energy deposition of  $E_0$  due to multiple Compton scattering. Coincidences by photons of energy higher than  $E_0$  will be denoted *correlated background coincidences* for  $E_0$  in the following.

## 4.4 Energy Selection

This work is meant to be a contribution to the development of a SPCC in the field of range verification in proton therapy. Therefore it is aim to show the principle of a DGRD as described in [Gueorguiev et al., 2010](#). In this report the authors used a similar setup as introduced in Chapter 3 where multiple gamma-ray lines were discriminated by sum energy criteria of the coincident events. The same approach can be used for the prompt gamma-ray spectrum obtained in this experiment. Because it is most prominent in this setup, the 4.44 MeV gamma-ray line is used for the analysis.

$$4.44 \text{ MeV} + \delta E_{4.44 \text{ MeV}} \geq E_r + E_l \geq 4.44 \text{ MeV} - \delta E_{4.44 \text{ MeV}} \quad (4.4.1)$$

Unlike the sources in [Gueorguiev et al., 2010](#) this gamma energy lies well above the threshold for pair production in the detector. Pair production is not dependent on the incident angle of the photons and therefore overlaying the searched effect of directionality. Below the energy of 511 keV it is not possible to distinguish whether a coincidence results from pure Compton scattering or if it is related to pair production. It is thus decided to apply

an additional energy cut on the energy deposition in the single detectors in order to be more sensitive.

$$E_{r/l} \geq 511 \text{ keV} + \delta E_{511 \text{ keV}} \quad (4.4.2)$$

The sum energy interval is calculated from the width of the 4.44 MeV peak in the sum energy spectrum which has a standard deviation  $\sigma$  of  $\delta E_{4.44 \text{ MeV}} = 3\sigma \approx 150 \text{ keV}$ <sup>1</sup>. The single detector cut on the other hand is calculated from the template spectrum for the bootstrapping algorithm and has a standard deviation of  $\delta E_{511 \text{ keV}} = 3\sigma \approx 70 \text{ keV}$ . This is defined as *selected energy cut* and makes up roughly 3% of the total rate of coincidences in the coincidence peak. A visualization of this cut in the two-dimensional energy histogram is displayed in Figure 4.4.1. Also the resulting projections of the standard energy cut which are the conditional spectra and the energy difference histogram, respectively, are shown in this figure. From the conditional spectra the mean energy difference is determined for the FOM and from the energy difference histogram the skewness and the left/right count ratio are extracted as described in Section 2.2.1.

By applying an energy cut on the two-dimensional energy histogram, knowingly a large portion of the given information is discarded to have a proof-of-principle of a DGRD. For the reconstruction of the range this information might still be used as discussed in Section 7.1.

---

<sup>1</sup>This width results from the resolution of the detector and the Doppler broadening of the 4.44 MeV gamma-ray line.

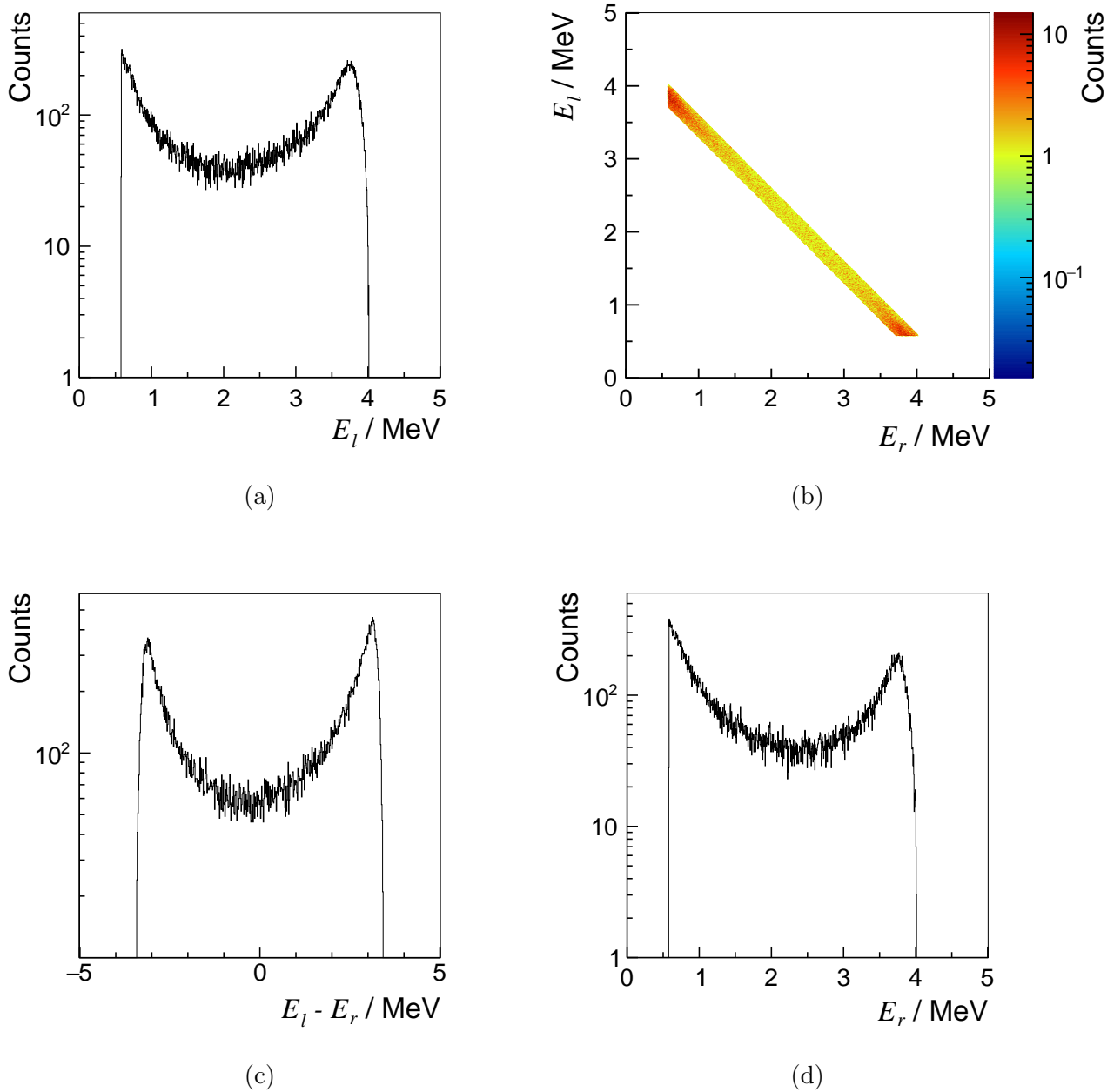


**Figure 4.4.1:** Exemplary energy spectra of the *selected energy window*. (b) The cut in the two-dimensional energy histogram. Figures (a) and (d) show the corresponding projections on the  $E_l$ - and  $E_r$ -axis of the two-dimensional energy spectrum, also known as the conditional spectra. (c) The projection on the diagonal axis  $E_l - E_r$  of the two-dimensional energy spectrum is displayed which is denoted as the energy difference histogram.



## 5 Modeling Based on the Geant4 Simulation Toolkit

Aim of the simulation is to model the experiment and to find a physical explanation of the obtained results. Adapting the models of the simulation to match the experimental results enables the extrapolation to more difficult setups in the simulation. Therefore the Geant4 simulation toolkit will be studied more closely especially regarding the different physics models. At first an overview of the performed simulation will be given.

### 5.1 Introduction to the Geant4 Simulation Toolkit

*Geant4* (GEometry ANd Tracking) is a simulation toolkit that evolved from a project of the CERN Detector Research and Development Committee (DRDC). Geant4 covers a wide range of application from “simple one-off studies of basic phenomena and geometries to full-scale detector simulations for experiments at the Large Hadron Collider and other facilities” [Agostinelli et al., 2003]. Key components of the simulation toolkit are the implementation of geometrical shapes with distinct physical properties and the transportation process for particles called tracking. Tracking is completely independent of the particle type. Physical processes are handled via physics modules. In Geant4 each user can implement the demanded physical processes. Of course there are some benchmarked reference physics lists<sup>1</sup> published by the Geant4 community for specific applications that include different models of electromagnetic and hadronic interactions. For hadrontherapy the use of QGSP\_BIC\_EMY was advised by Cirrone et al., 2011. Here QGSP\_BIC\_EMY is an acronym that stands for the hadronic model for nucleons QGSP (Quark Gluon String Precompound), the inelastic model for ions BIC (Binary Ion Cascade), and the electromagnetic model EMY (ElectroMagnetic Y) for all particles. Physics lists will be discussed in more detailed in Section 5.3.

---

<sup>1</sup><https://geant4.web.cern.ch/node/628>

## 5.2 Features of the Simulation

For the simulations Geant4 version 10.03.p01 was used. The main goal in this thesis is to model the coincidence system of two head-to-head  $\text{CeBr}_3$  scintillators - denoted *Det 0* and *Det 1* - as *sensitive detectors* of dimension  $\varnothing 2'' \times 2''$  each. Sensitive in this context means that Geant4 is saving a collection of all interactions in the volume during runtime. The experimental setup was simplified by only implementing a PMMA target as shown in Figure 5.2.1. Geometrical features of the simulation are:

- (1) setting the position of the detector pair along the cylindrical  $z$ -axis
- (2) setting the distance  $d$  between the  $z$ -axes of the detector pair and the target
- (3) setting the dimensions of the scintillators ( $R_{det}$ ,  $z_{det}$ )
- (4) setting a cover (aluminum) around the scintillators of thickness  $d_{cover}$
- (5) setting different predefined materials for world/cover/target

Particles are created by the *general particle source* (GPS) [Ferguson, 2000]. Two different predefined particle guns can be used via a macro file:

- (1) monoenergetic, isotropic photon radiation from the point of origin
- (2) monoenergetic proton beam along negative  $z$ -axis

The physics list can be chosen as input parameter of the simulation via abbreviations of the physics list factory.

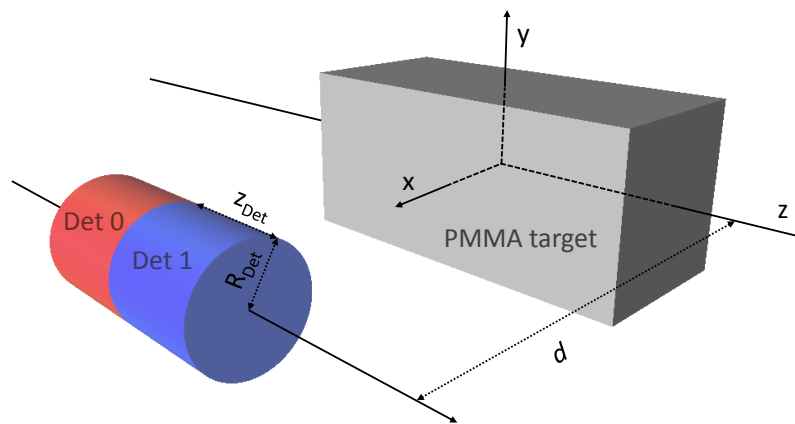


**Figure 5.2.1:** Perspective drawing of the experimental setup without a detector cover.



The simulation should comprise the production of prompt gamma radiation along the proton beam. These prompt gamma photons will initially interact with the target material and eventually with the detector setup. For the conditional spectra only coincident events between the two scintillators are of interest. The whole task could in principle be performed all-in-one but would take much simulation time since only few protons lead to nuclear reactions in the target. Besides, these photons would be distributed in  $4\pi$  solid angle and thus hit the detector pair rarely. For the reason of saving simulation time and to cross-check the gamma-ray emission profile along the proton's path, a successive simulation method was preferred. This simulation is divided into two steps:

- (1) Tracking of the production rate of a prompt gamma-ray line in the target along the proton's path. From this the emission profile of the prompt gamma-ray line is obtained.
- (2) Tracking of the interactions of prompt gamma radiation with the setup of target and detector. The prompt gamma radiation is emitted according to the obtained emission profile. By this step the coincidences between the two scintillators are obtained.

As discussed in Section 4.4, the focus is laid upon the emission of the 4.44 MeV gamma-ray line from  $^{12}\text{C}$  and  $^{11}\text{B}$ . There are some publications that have already made efforts to check cross sections of the prompt gamma-ray production for proton therapy in Geant4 [Jeyasugiththan and Peterson, 2015, Verburg et al., 2012]. They come to the conclusion, that the prompt gamma-ray emission of the 4.44 MeV gamma-ray line is underestimated by the investigated cross section models for proton energies above 10 MeV. The total production yield on the other hand seems to be higher in the simulation than in the experiment as stated by Schumann et al., 2015. Adaption of the simulation in terms of cross sections and photon production yield to the experimental setup would go beyond the scope of this work. Therefore the default cross sections and physics list of Geant4 were used to simulate the emission profile. The emission profile can be extracted by registering the *number of secondaries* with a specific energy produced at a certain point along the beam axis. The chosen ROI of the energy emission spectrum from 4.436 MeV to 4.446 MeV and the resulting emission profile along the *penetration depth*  $D$  of the 4.44 MeV gamma-ray line is displayed in Figure 5.2.2. From the broad peak in the emission spectrum the effect of Doppler broadening of in-flight emitted photons can be seen. The ROI was set before considering the Doppler broadening of the gamma-ray lines and should therefore only include a tight window which contains the gamma-ray emission of  $^{12}\text{C}$  and  $^{11}\text{B}$  at 4.44 MeV.

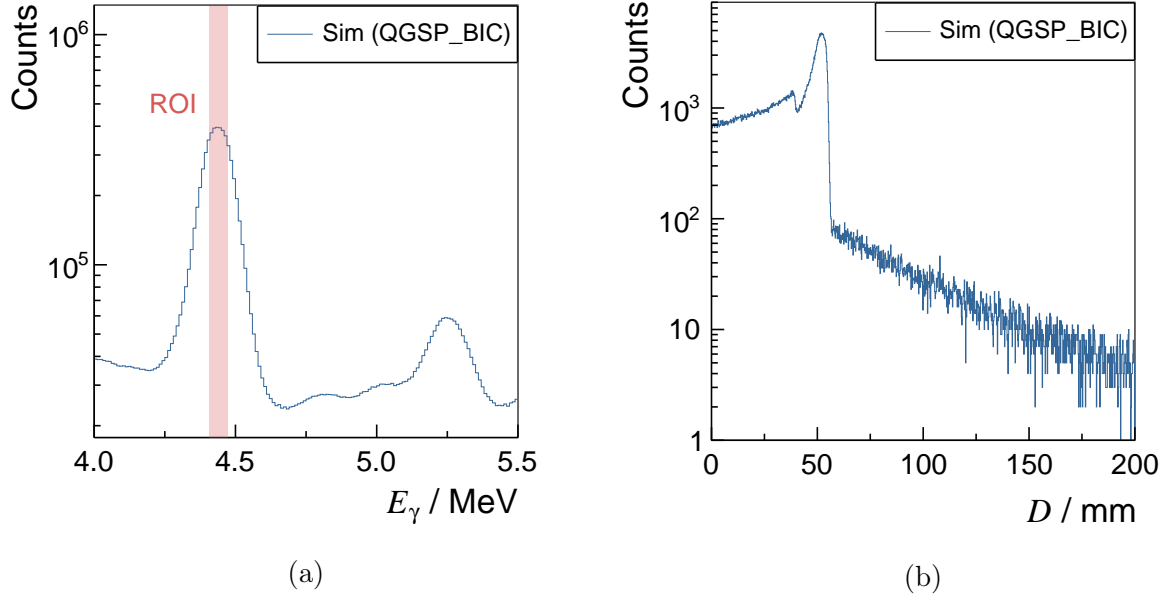


**Figure 5.2.2:** Visualizing the method of extracting the emission profile in the case of 90 MeV protons on a 20 cm PMMA target using the QGSP\_BIC physics list. (a) Emission spectrum with a narrow ROI marked in red. (b) Emission profile of events from the ROI along the proton’s beam path.

In the second step of the simulation these emission profiles are used to isotropically emit gamma photons from *discrete positions*  $Z_i$  along the incident proton beam. The *number of counts*  $N$  in the bin containing  $Z_i$  in the emission profile is defined as the *weight*  $N(Z_i)$  of the gamma-ray emission at this point. The isotropical emission is of course a simplistic assumption. From the experiment there is evidence that the prompt gamma-ray emission of the 4.44 MeV gamma-ray line is not isotropically distributed [Kelleter et al., 2017]. Like in the experiment, the position of the detector pair along the  $z$ -axis is changed. The energy deposition in the detectors of all the coincident events is saved for the further analysis of extracting the FOM.

To save simulation time, the emission angle at each source position  $Z_i$  with respect to the detector position  $z$  is restricted to events that hit the detector. Because of this a correction to the weights must be applied since the weights beforehand refer to emission in  $4\pi$ . The *new weights*  $N'(Z_i)$  can be obtained by multiplying the *old weights*  $N(Z_i)$  by the calculated *solid angle*  $\Delta\Omega(Z_i, z)$  as follows.

$$N'(Z_i) = N(Z_i) \cdot \Delta\Omega(Z_i, z) \quad (5.2.1)$$

Figure 5.2.3 shows the FOM of a random emission profile when emitted with restriction compared to the emission in a constant solid angle, for instance  $4\pi$ . It can be seen, that the correction gives the same results as the constant solid angle while the not corrected weights give a different curve with offset.

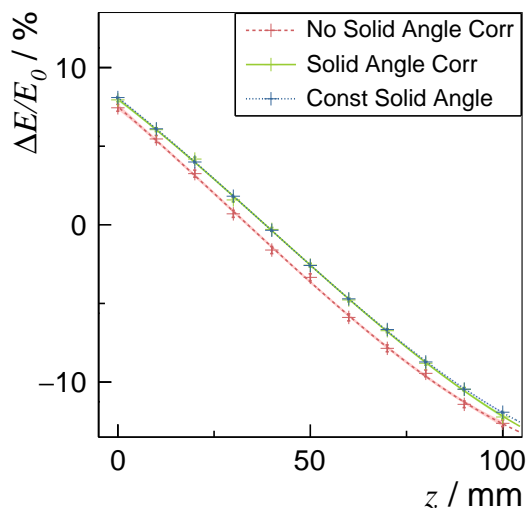


**Figure 5.2.3:** FOM of a random emission profile showing the result of a restricted solid angle emission with and without correction of the emission weight in comparison to a constant solid angle emission.

### 5.3 Choosing the Right Physics List

There have been several studies on physics lists for a medical application as stated in the last chapter. Since the prompt gamma-ray emission is becoming a field of interest, many groups try to find the best models for inelastic scattering of ions which can result in the emission of prompt gamma-rays. “Geant4 provides several pre-built physics models for low-energy proton-nuclear inelastic interactions: the binary cascade (BIC), precompound (PRECO),” which is included in the BIC model, “and intra-nuclear cascade (INCLXX) models. The alternate Bertini cascade model was unsuitable as discrete prompt gamma-ray spectrum was not observed”, which can be seen in Figure 5.3.1 [Jeyasugithan and Peterson, 2015]. This detector spectrum also shows the difference between the experiment and the spectrum of QGSP\_BIC\_EMY, the most commonly used physics list in hadron therapy. Compared to the height of the 4.44 MeV peak, the low energetic region is slightly underestimated while the high energetic region is greatly over-

estimated in this physics model. Schumann et al., 2015 found, that the prompt gamma-ray yield of the QGSP\_BIC\_HP physics list from 3 - 7 MeV is up to 50% higher compared to the experiment. On default, Geant4 uses the total non-elastic reaction cross section of Wellisch and Axen [Wellisch and Axen, 1996]. It might be considered repeating the simulation of the emission profile with the cross section of Tripathi [Tripathi et al., 1999] which have been found to be in greater accordance to experimental cross sections of the 4.44 MeV gamma-ray line by Jeyasugiththan and Peterson, 2015.

Additionally to these inelastic models, there is the option of activating the High Precision (HP) neutron models and cross sections to describe elastic and inelastic scattering, capture and fission of neutrons below 20 MeV. The G4NDL evaluated neutron data library is required for these physics lists. To discuss the influence, simulations were performed with and without the HP model.

Also, there are different models for electromagnetic interactions. There is the standard electromagnetic physics list option 3 (EMY) "particularly tailored for the use in medical physics" [Cirrone et al., 2011]. The most advanced electromagnetic physics list to date is option 4 (EMZ) which does include all packages from EMY and some more models. It was thus used for the second step of the simulation. The reference physics list QGSP\_BIC uses the *standard* Geant4 electromagnetic physics (EM) and was also tested.

For the interactions of nucleons the advised physics model (QGSP) for the application in proton therapy was not considered to be changed. For more information on the Geant4 reference physics lists see the Physics Reference Manual<sup>2</sup>.

The influence on the emission profile of the 4.44 MeV gamma-ray line for different of the above stated models has been tested. The used reference physics lists are denoted in the legend of Figure 5.3.2 (a) showing the various emission profiles. The simulated protons in this profile have an energy of 90 MeV corresponding to a CSDA range of 55 mm in PMMA. The emission profile of the 4.44 MeV gamma-ray line has contributions of two transition in the target as stated in table 1.4.1. These two transitions cannot be distinguished due to Doppler broadening. De-excitation from  $^{11}\text{B}^{*4.445}$  contributes only at the beginning of the penetration depth in the target as this isotope is a secondary product. The main part of the profile is resulting from de-excitation of the  $^{12}\text{C}^{*4.439}$  nucleus. As the nuclear reactions of the protons release neutrons from the target nuclei, there are also neutrons contributing to the emission profile which can especially be seen from the non-zero fraction of events after the protons have already stopped. In Figure 5.3.2 (b) the angular and energy integrated

<sup>2</sup><http://geant4-userdoc.web.cern.ch/geant4-userdoc/UsersGuides/PhysicsReferenceManual/fo/PhysicsReferenceManual.pdf>

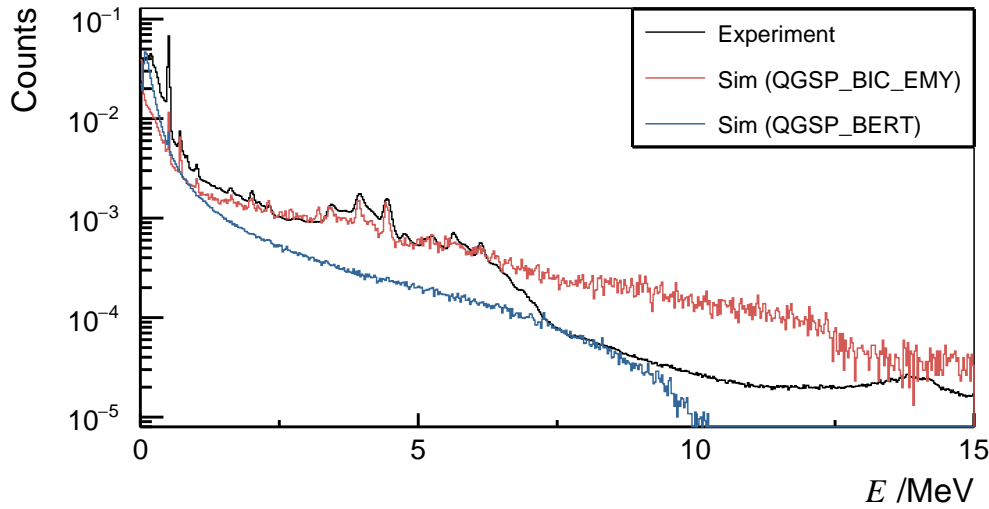


**Figure 5.3.1:** Comparison of the experimental detector spectrum to the detector spectrum resulting from Geant4 reference physics lists. The simulations are normalized on their integral and the experiment is scaled to match the the QGSP\_BIC\_EMY spectrum in the range of the 4.44 MeV gamma-ray peak. No detector resolution was considered in the simulation. Setting is a 90 MeV proton beam on a PMMA target.

production cross section data of the ENDF / B-VIII.0 evaluated cross section is shown for protons on  $^{12}\text{C}$  [Brown et al., 2018]. The production of  $^{11}\text{B}$  occurs only for incident protons above 20 MeV. Therefore no  $^{11}\text{B}$  contributes to the emission profile from the penetration depth on, where the protons carry an energy less than 20 MeV. Protons of about 20 MeV have a CSDA range of 4 mm in PMMA. Therefore from 51 mm on - assuming the range of the produced  $^{11}\text{B}$  nuclei is almost zero - there is no  $^{11}\text{B}$  in the target produced by a 90 MeV proton beam. The resulting Neutrons on the other hand are also just produced in the first five centimeters of the target but do contribute to the emission profile over the full penetration depth due to their neutral charge which makes them hard to stop. It is seen that the contribution of neutrons results in a tail of the emission spectrum with a logarithmic descent. The highest fraction of events in this emission profile results from reactions producing  $^{12}\text{C}^*4.439$ . The target nuclei of these reactions in PMMA are  $^{12}\text{C}$ ,  $^{13}\text{C}$  and  $^{16}\text{O}$  while  $^{12}\text{C}$  contributes the most and  $^{13}\text{C}$  the least. Hence the shape of the emission profile is mainly influenced by the inelastic collision of a proton with  $^{12}\text{C}$  which mainly produces 4.439 MeV photons as concluded from the ENDF / B-VIII.0 data base. It can be seen from the cross section data in Figure 5.3.2 (b) that there is a small dip at 20 MeV for the photon cross section. When comparing this curvature to the simulated emission profile in Figure 5.3.2 (a), such a dip is also present when using the BIC physics list. The

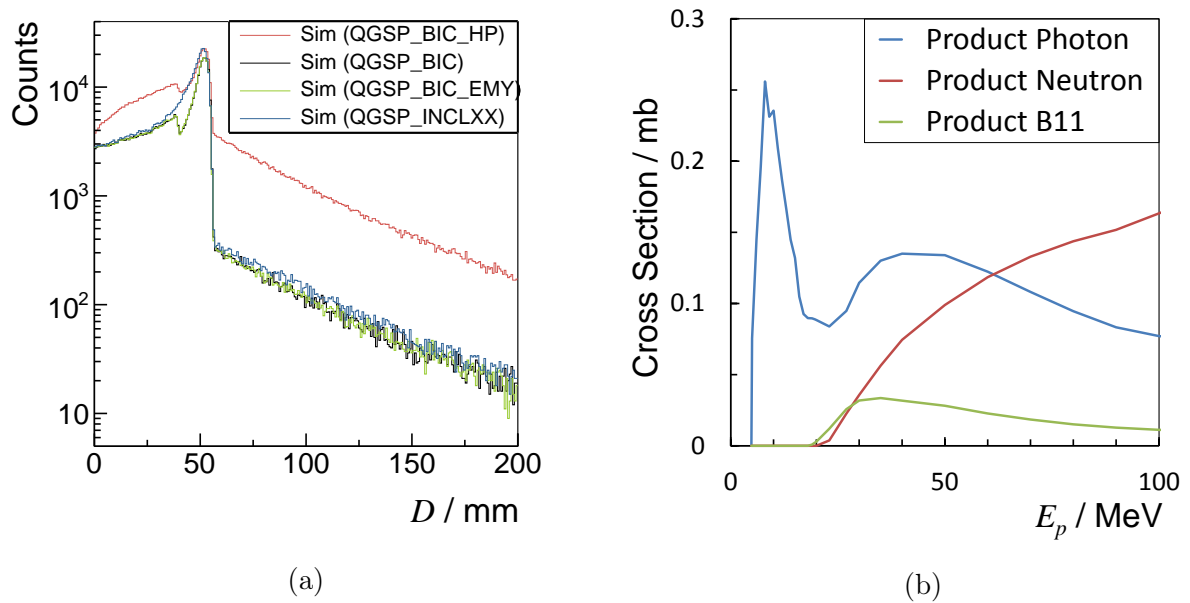


**Figure 5.3.2:** Comparison of the emission profile from different physics lists in reference to evaluated cross sections. (a) Emission profile of various Geant4 reference physics lists for a 90 MeV proton beam on a 20 cm long PMMA target. (b) Production cross section of various products for protons on  $^{12}\text{C}$  of the ENDF / B-VIII.0 evaluated cross section data base [Brown et al., 2018].

dip in the experimental data could also result from the different target nuclei producing a  $^{12}\text{C}^{*4.439}$  nucleus. The nuclei  $^{12}\text{C}$  and  $^{16}\text{O}$  for instance have a resonance at different proton energies [Jeyasugiththan and Peterson, 2015]. The INCLXX physics list does not show this dip leading to the conclusion, that the BIC model is better suited to describe the evaluated cross section data and the resonance of the different reactions in PMMA, respectively.

When applying the EMY electromagnetic model, there is no significant difference found compared to the standard electromagnetic physics list. Only the use of the HP neutron model leads to a drastic change of the emission profile seemingly overestimating the neutron induced reactions. This has been investigated closely and will be discussed in the next section. It could be shown that the resulting profile is due to missing Doppler broadening of in-flight emitted photons in the HP model.

All-in-all it was decided to use the emission profile resulting from the QGSP\_BIC reference physics list for the first step of the proof-of-principle simulation. For the emission of photons in the second step of this simulation the more precise electromagnetic physics list QGSP\_BIC\_EMZ was chosen. Additionally to the default *tracking cuts*, for neutrons an energy cut of 10 keV and a time cut of 10  $\mu\text{s}$  was applied in all simulations for performance.

### 5.3.1 The High Precision (HP) Neutron Model Problem

Comparing the emission profiles in Figure 5.3.2 (a), large deviations are found for the same physics list with and without the neutron HP model activated. This section is narrowing down the differences to find the cause of these deviations.

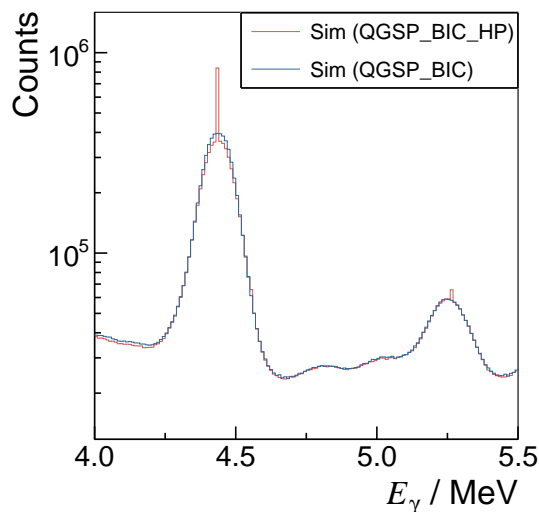


**Figure 5.3.3:** Emission spectrum of prompt gamma radiation in a PMMA target simulated by different physics lists.

For the HP model there is a spike in the emission spectrum of the 4.44 MeV gamma-ray line as seen in Figure 5.3.3. Only the two nuclei,  $^{11}\text{B}$  and  $^{12}\text{C}$ , have de-excitation energies of about 4.44 MeV. In this section it will be focused only on the de-excitation of the  $^{12}\text{C}$  isotope. Because the HP model only modifies neutron reactions by using an evaluated neutron data library, the effect must be due to reactions of neutrons. It is visible from Figure 5.3.3 that despite the spike, the area of the peak seems to remain constant. Hence there are roughly the same number of 4.44 MeV secondary gamma particles created regardless of the use of the neutron HP physics model. The emission spectrum of the 4.44 MeV is broadened due to Doppler broadening. As observed by [Schumann et al., 2015](#), “the implementation of Doppler broadening is very limited in Geant4.” Their analysis of the QGSP\_BIC\_HP physics list revealed, “that photons emitted at the end of an inelastic proton reaction are broadened and those being created by an inelastic neutron reaction are not.” Therefore the task is to further determine the events in the spike. These events are considered to be handled by the HP model and are supposed to result from neutron reactions of energy below 20 MeV. For this a simulation setup is chosen, where only natural carbon is present to interact with protons. The following reaction can then lead to the de-excitation of  $^{12}\text{C}$ .

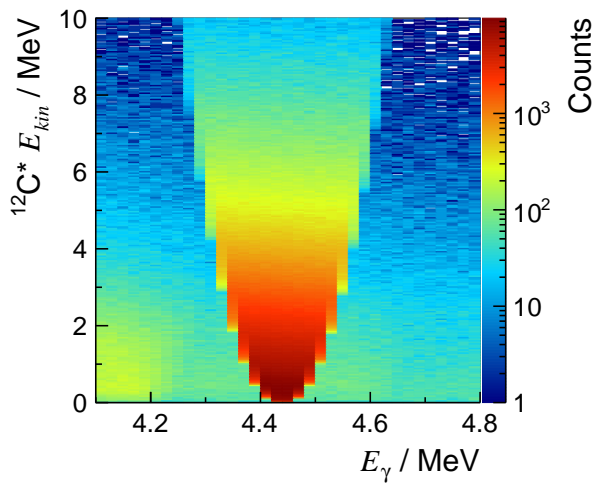
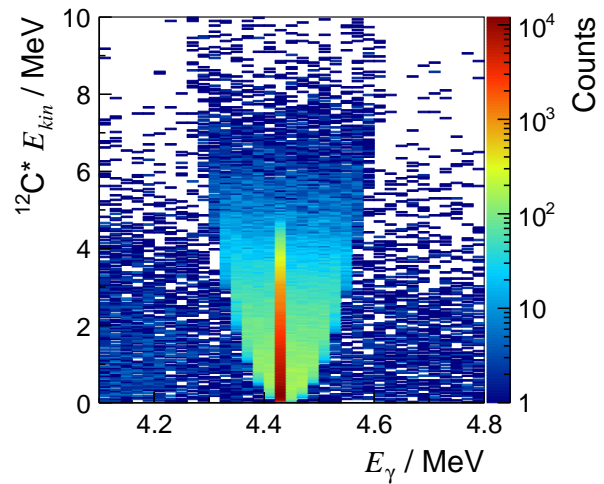
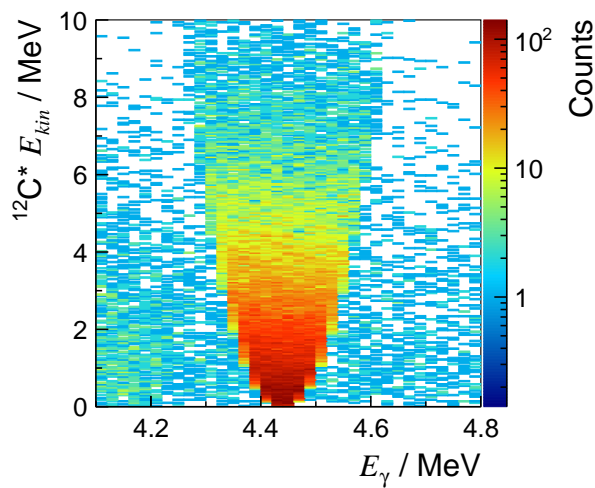
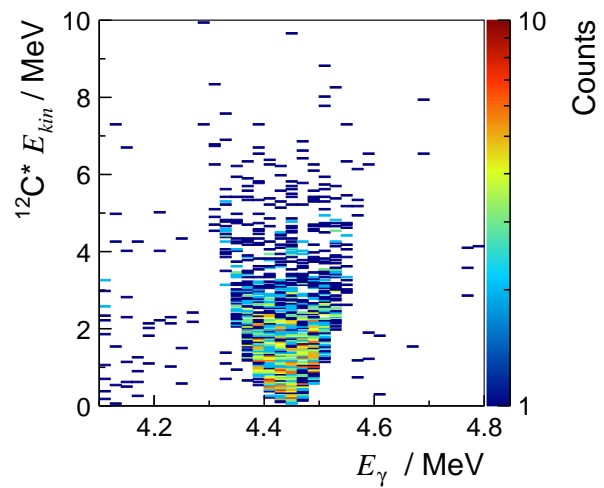


Though the primary particles are protons, the reactions in Equation 5.3.2 and 5.3.4 can also occur because of secondary neutrons from inelastic proton-nucleus-reactions. In the simulation all reactions are recorded, in which a gamma particle is created and one of the two carbon nuclei is involved. To study the emission behavior, the resulting gamma-ray energy is plotted with respect to the residual kinetic energy of the carbon nucleus. According to reactions 5.3.1-5.3.4 there are four plots resulting shown in Figure 5.3.4.

If Doppler broadening is implemented correctly, one would expect a funnel-like distribution for one discrete gamma-ray line. This can be seen for all reactions. In addition for the 5.3.2 type reaction there is a large number of events which do not seem to follow the funnel-like distribution. These are the events of neutron induced nuclear reactions on  ${}^{12}\text{C}$  which do result in the spike of the emission spectrum. Moreover it can be assumed, that these reactions are handled by two different models, in particular neutrons below 20 MeV by the HP model. It seems as though Doppler broadening of the nuclear de-excitation via gamma particles is not considered for the neutrons in the HP model. For the emission spectrum this leads to a higher influence of neutron induced reactions in the chosen ROI (see Figure 5.2.2). Therefore this method of extracting the emission profile with the chosen ROI is not applicable in the case of the HP model. On the other hand using the HP model would be preferable for more realistic processing of neutrons. For this the ROI could be broadened in future simulations. Alternatively one can implement the Doppler broadening for these reactions manually into Geant4. In the scope of this work this could not be done so far.

In conclusion one finds, when narrowing down the difference in the emission profiles with and without HP model activated, the problem lies in the combination of the following: negligence of Doppler broadening for the neutron induced in the HP model and the method of extracting the profile by a narrow ROI itself.



Proton induced reaction on  $^{12}\text{C}$  (5.3.1).Neutron induced reaction on  $^{12}\text{C}$  (5.3.2).Proton induced reaction on  $^{13}\text{C}$  (5.3.3).Neutron induced reaction on  $^{13}\text{C}$  (5.3.4).

**Figure 5.3.4:** Doppler broadening of the 4.4 MeV gamma-ray line from the  $^{12}\text{C}^*$  nucleus. Shown is the kinetic energy of the  $^{12}\text{C}^*$  nucleus over the gamma-ray energy. Each plot corresponds to a different reaction according to (5.3.1)-(5.3.4).



## 6 Experimental and Simulated Results

In this chapter the experimental results from the proof-of-principle experiment shall be discussed. Further, simulations are presented that were performed to gain a deeper understanding of the experimental findings. In the last section results from a direct reconstruction of the experiment with a simplified simulation are displayed.

### 6.1 Experimental Results of the Figure of Merit

In the experiment it was explored whether a DGRD is applicable for range verification. Therefore the conditional spectra were analyzed for different measurement positions. The Figure of Merit (FOM) was introduced to quantify the sensitivity of a DGRD from the conditional spectra [Gueorguiev et al., 2010]. In the setup of the experiment only the 4.4 MeV gamma-ray line was chosen for simplicity. As already seen from the benchmark experiment in Section 3.2, the FOM at photon energies of 511 keV and 1275 keV shows varying strong dependencies from the incident angle. In Figure 6.1.1 the plot of the FOM can be seen for the selected energy window as defined in Section 4.4. The results are shown for both detector units at 90 MeV and 150 MeV proton energy, respectively.

To make it clear, the scheme in Figure 6.1.2 shows the frame of reference for comparison of experimental and simulated data. The zero point of the z-axis in the analysis was chosen to be the position at which the plane of the front edge of the target and the plane between the detectors are at level. In the FOM the value on the z-axis stands for the relative position of the plane between the detectors towards the front edge of the target. Since there is a distributed source in the experiment, the FOM is shown in its dependency towards this  $z$  value rather than towards an angle.

In Figure 6.1.1 can be seen, that the FOM of the 4.4 MeV gamma-ray line is significantly depending on the relative position of the detectors towards the target. The difference between the two detection units of  $\varnothing 2'' \times 2''$  and  $\varnothing 2'' \times 1''$  scintillators is a shift on the vertical axis of the graph. The dependency seems smooth as expected. In a first approximation a third degree polynomial is chosen to fit the data points and to guide the eye. This has no

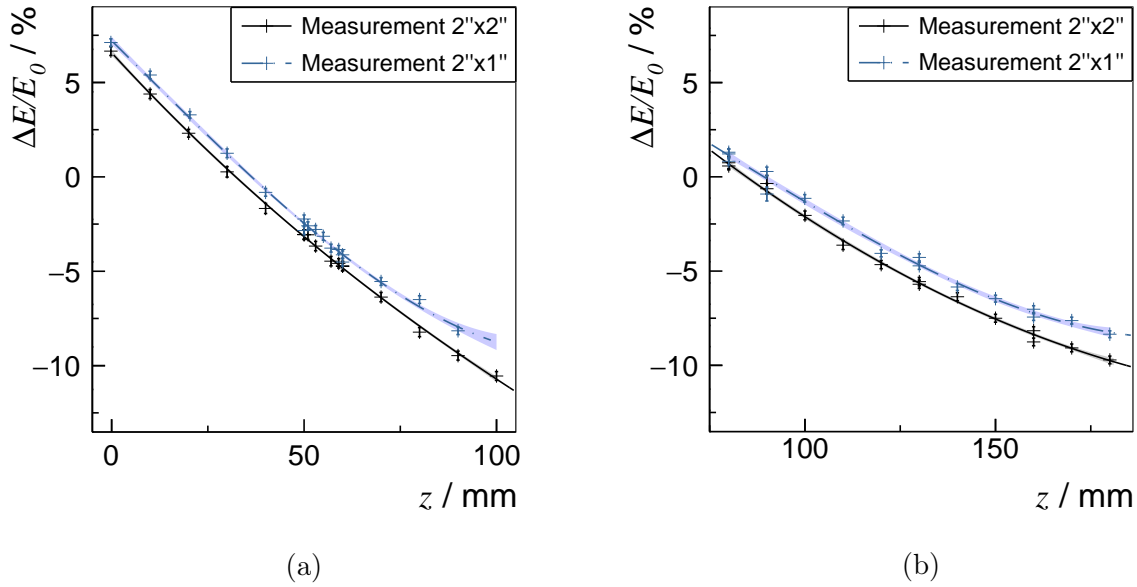


**Figure 6.1.1:** Plot of the FOM for the 4.4 MeV gamma-ray line with the selected energy window for the protons on PMMA with energy of (a) 90 MeV (CSDA range of 55 mm) and (b) 150 MeV (CSDA range of 136 mm), respectively. The two detection systems with scintillator size of  $\varnothing 2'' \times 2''$  and  $\varnothing 2'' \times 1''$  are displayed. The third degree polynomial fits serve to guide the eye.

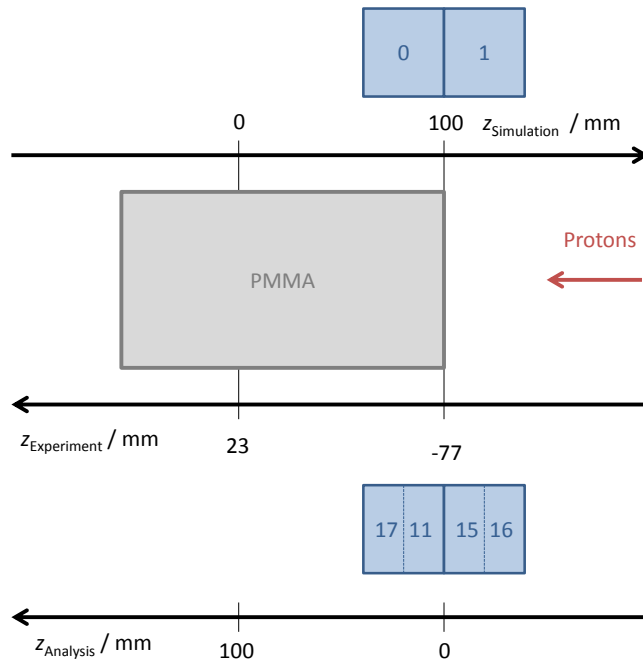


**Figure 6.1.2:** Reference frame of the analysis showing the conversion of the experimental and simulated data to the analysis frame.

physical motivation - in fact, because of the non-point-like activity distribution the FOM cannot be parametrized like in the benchmark experiment.

The two proton energies in comparison show a slightly steeper dependency for the FOM of 90 MeV. This can be explained by looking at the different activity distribution. For the 150 MeV proton beam the range is higher thus the activity distribution along the z-axis is broader. The FOM is sensitive towards the angle of the incident radiation. By having a broader distribution, more incident angles can occur. Small shifts of this distribution change the incident angles only little. In contrast, when shifting a point source along the z-axis, the incident angle will change completely. The conditional spectra of a distributed source are a weighted superposition of conditional spectra from all incident angles. Therefore the variation of these spectra due to shift on a line will be the smaller, the broader the activity distribution. Thus the FOM will be more flat compared to a less broad distribution.

In the experiment it was also investigated, if a change of the activity distribution is detectable by the FOM, since this is a more realistic situation for range verification. Such changes could for instance result from a deviation of the planned to the real target density or from a modified tissue composition. To study this, the beam energy was changed during a steady experimental setup. From the model of CSDA (see Equation 1.1.3) the proton energy was converted into a range to assess range prediction. In Figure 6.1.3 one can see that the FOM is directly dependent on the proton range as well. The precision of the range assessment at this level of statistics (around 50 000 events in the selected energy window) is of a few millimeters considering an uncertainty band of  $1\sigma$  around the fit. Similar precision is achieved for the previous measurements in Figure 6.1.1.

The FOM of the selected energy window could principally be used for range verification. It would also be interesting to know, if the FOM of other prompt gamma-ray lines shows such a correlation. Therefore the same analysis was done with different cuts of the sum energy that correspond to specific gamma-ray lines. For this, only the detection system with  $\varnothing 2'' \times 2''$  scintillators was evaluated. To show the influence of pair production on the FOM the analysis has been performed for the 4.4 MeV gamma-ray line with and without the additional cut on the 511 keV photons. The corresponding energy cuts and the resulting FOM are shown in Figure 6.1.4. From this plot becomes clear, that there is a strong dependency of the FOM on the energy of the scattered photons. In particular the sign of the slope is changing as the scattered gamma-ray energy is increasing. Because of this there exists a gamma-ray energy at which there is almost no correlation of the FOM from

the relative position to the target. For the needs of range verification this means, that the FOM might not be the best measure to quantify the effect. Another disadvantage is the fact, that the different gamma-ray lines need to be treated separately. One can also see, that the complete energy cut on the 4.4 MeV gamma-ray line has a weaker dependency of the FOM than the selected energy cut in section 4.4. If this is due to pair production will be investigated in the next section.

But is there a better parametrization for the shape of the coincident energy spectra? There were two more parameters introduced in Section 2.2.1. The skewness of the energy difference histogram and the left/right count ratio. Both parameters are also dependent on the relative position of target and detector system. But when comparing different gamma-ray lines the same problem like for the FOM occurs as seen in Figure 6.1.5. Therefore it can be concluded that these parametrization are able of extracting range only when applied on some single gamma-ray lines by sum energy cuts and possibly applying additional cuts.

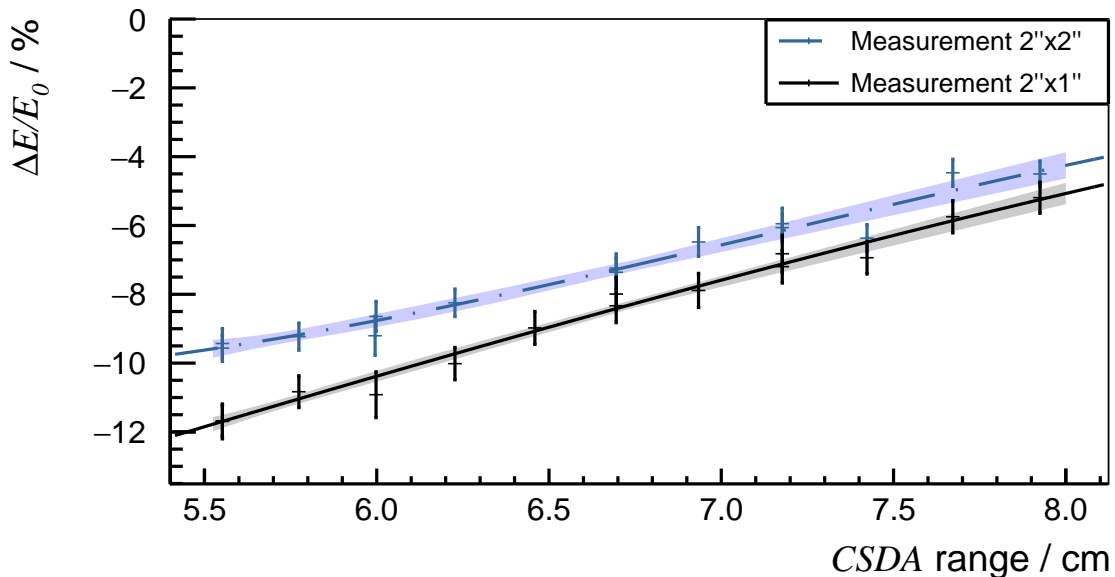


**Figure 6.1.3:** FOM dependent on the proton energy in a steady setup. Proton energy has been converted into range in PMMA via CSDA for range assessment. The two detection systems with scintillator size of  $\varnothing 2'' \times 2''$  and  $\varnothing 2'' \times 1''$  are displayed. The third degree polynomial fits serve to guide the eye.

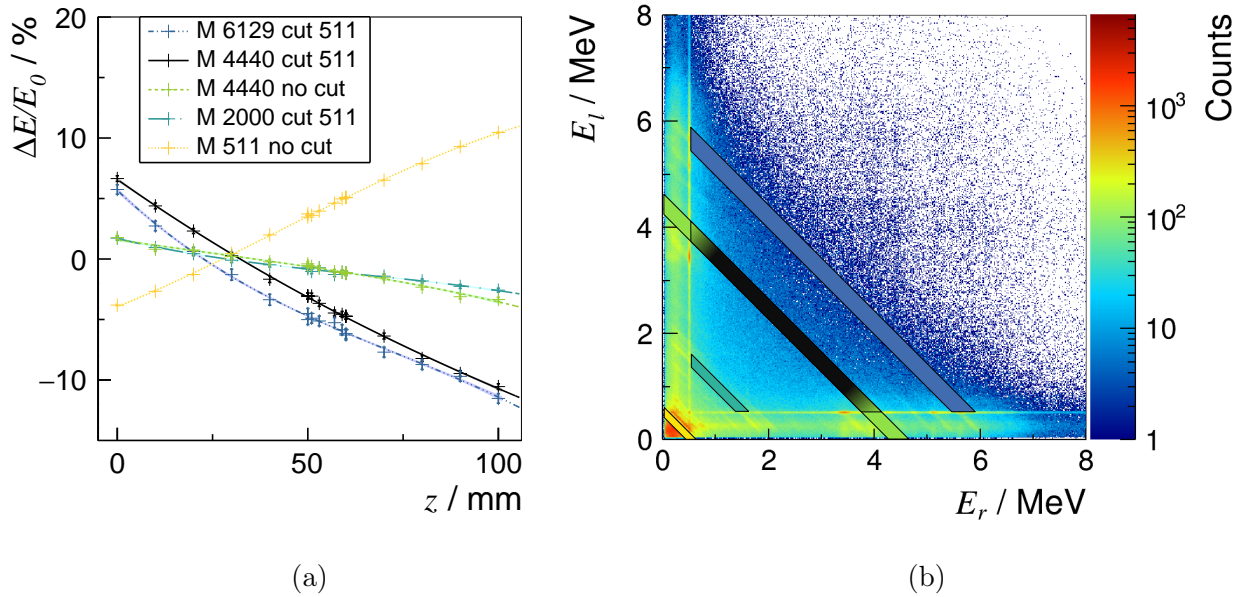


**Figure 6.1.4:** (a) Plot of the FOM for different gamma-ray lines and different energy cuts for the  $\varnothing 2'' \times 2''$  detectors. (b) Visualization of the different energy cuts in the two-dimensional energy histogram.

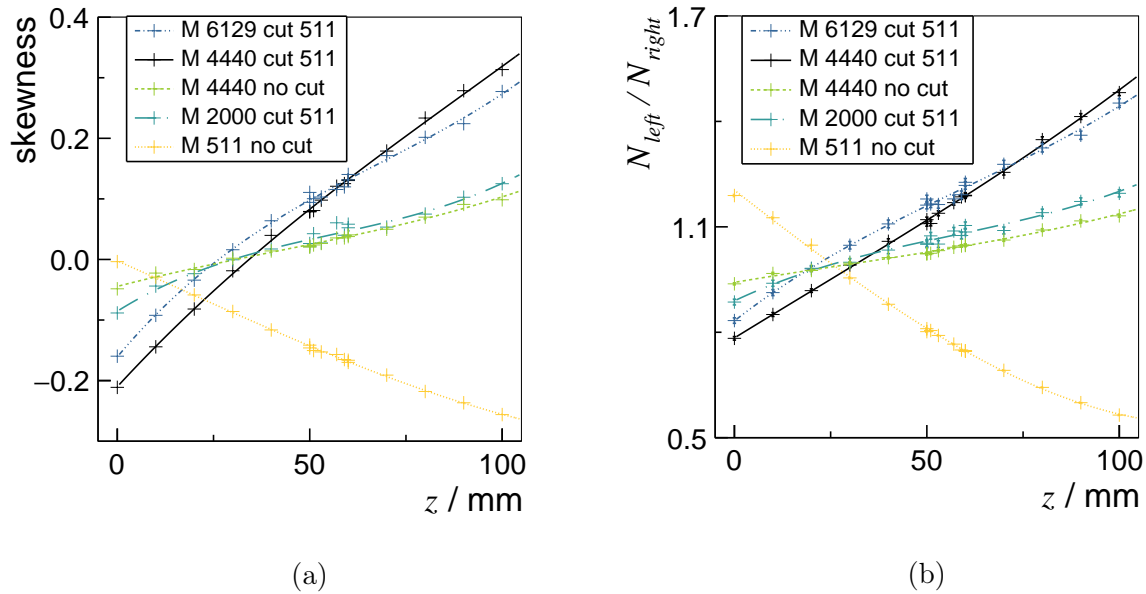


**Figure 6.1.5:** Skewness (a) and left/right count ratio (b) of the measured energy difference of the  $\varnothing 2'' \times 2''$  scintillators. Different gamma-ray lines with and without an 511 keV energy cut are selected at 90 MeV proton energy.

## 6.2 Simulation of Conditional Spectra

In order to understand the behavior of the FOM regarding different gamma-ray energies a simulation has been performed. The detection system of two cylindrical  $\varnothing 2'' \times 2''$   $\text{CeBr}_3$  was modeled. Then a monoenergetic gamma-ray point source was located in a certain distance at different positions along the z-axis of the detectors just like in the experiment. At run time only those events have been kept that caused a coincidence between the two detectors. In the analysis the condition is applied that the initial photon must have been fully absorbed. Unlike in the experiment, not only the conditional spectra can be measured, but it can also be resolved, in which of the two detectors the Compton scattering occurred. That might help to understand how much each detector contributes to the conditional spectra which can be measured. An asymmetric setup of the simulation, as shown in Figure 6.2.1, was performed with four different photon energies: 150 keV, 511 keV, 2 MeV and 4.44 MeV. Below in Figure 6.2.2 the conditional spectra for these gamma-ray energies are shown. In addition the conditional spectra are differentiated according to the detector in which the first interaction occurred.

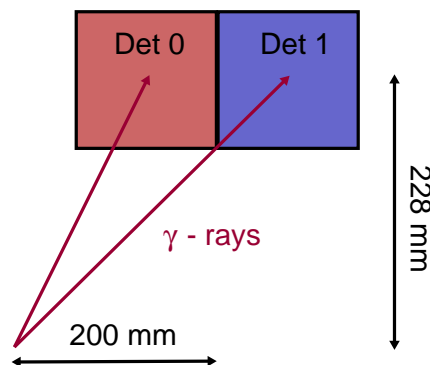


**Figure 6.2.1:** Setup of the simulation using two  $2'' \times 2''$   $\text{CeBr}_3$  detectors irradiated isotropically from the given point source position with gamma-rays of different energy.

In the following paragraphs important findings from these conditional spectra are listed and the influence on the FOM is qualitatively evaluated. For this “Det 0” is denoted as leading detector and “Det 1” is denoted as distal detector due to their positioning towards to point source.

First of all, from this figure the decreasing number of events for single Compton scattering paired with full absorption is noticeable as the gamma-ray energy increases. Hence the classical picture of a DGRD with one Compton scattering is inadequate for the description of the conditional spectra. Multiple Compton scattering leads to a smoothing of the



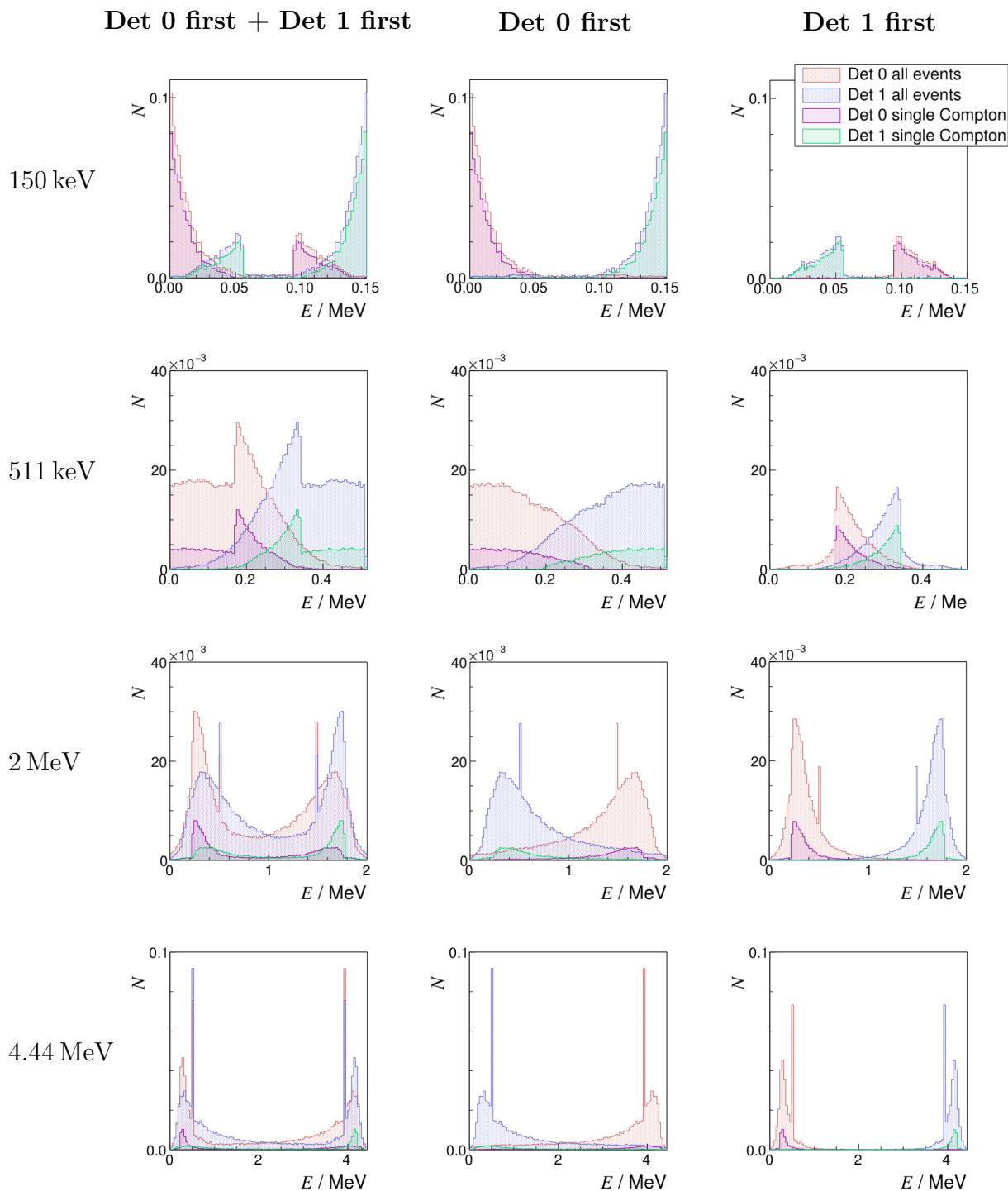


**Figure 6.2.2:** Normed conditional spectra for photons of energy 150 keV, 511 keV, 2 MeV and 4.44 MeV on two head-to-head  $\varnothing 2'' \times 2''$  CeBr<sub>3</sub> detectors. The columns contain the spectra under the condition that the first interaction occurred either in Det 0 or Det 1 and the sum of these spectra, respectively. The spectra were produced under the same position to the source (Figure 6.2.1) and by the condition of full absorption. The “single Compt” filter is showing only events with a Compton scattering in the first detector and no other Compton scattering or pair production elsewhere.

spectra as the sharp energy intervals from the allowed scattering angles are blurred. Still, this effect will only have a small influence on the FOM.

The pair production rate, which leads to coincidences, is rising with increasing gamma-ray energy from the threshold of 1.022 MeV on. It can be found that there are more coincidences due to pair production in the leading detector than in the distal detector. This is due to the shielding of the distal detector by the leading detector. Because of this shielding the pair production rate in the detectors is unexpectedly dependent on the incident angle and can be considered a valuable contribution to the conditional spectra.

Events with their first interaction in the distal detector, contribute generally less to the overall number of coincidences. This is due to the Klein-Nishina formula which prefers forward scattering as the gamma-ray energy is increasing (see Figure 2.1.1). But the contribution is highest for the case of 2 MeV and not for 150 keV since on the other hand the attenuation by the leading detector increases with lower energies and thus less photons reach the distal detector.

The energy distribution of the distal detector hit first is also narrower than for the other case. This is due to the Compton formula in which the slope of the scattered photon's energy is flatter for larger scattering angles as seen in Figure 2.2.2. Furthermore the Compton formula leads to a switch in the energy relation between the recoil electron and the scattered photon. Assuming the electron is fully absorbed at the detector of interaction this behavior can be validated by the conditional spectra of the different photon energies. Whereas for 150 keV the energy of the scattered photon is always higher than of the recoil electron, this already changes in the case of 511 keV photons. It is seen that for small scattering angles the recoil electron gains more energy in some cases than left on the photon when scattered in the leading detector. When scattered in the distal detector it even gains more energy in most cases. Getting to higher gamma-ray energies such as 2 MeV this trend is even spreading to the leading detector while the energy difference of the scattered particles in the distal detector is even more increasing for the majority of events. Though the possible scattering angles are not changing during the simulation, the energy ratio due to the Compton formula is still dependent on the initial gamma-ray energy and thus resulting in the switch. This is one of the main reason why the slope of the FOM is switching from positive to negative at higher gamma-ray energies (see Figure 6.1.4 (a)).

The other reason is found in the additional energy cut which has been applied on the data. Pair production was thought to weaken the dependency of the FOM and was therefore excluded in the analysis. The simulation denied this and showed that rather the events resulting from Compton scattering in one or the other detector compensate each other. Looking at the conditional spectra, energy intervals can be

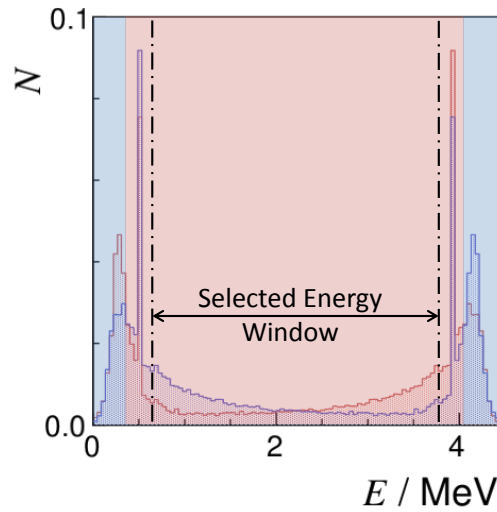


**Figure 6.2.3:** Energy intervals of the conditional spectra of the 4.44 MeV gamma-ray line derived from an asymmetric setup (Figure 6.2.1). In the red interval the leading detector and in the blue interval the distal detector counts more high energetic coincidences. The selected energy cut lies within red interval. The intervals result from the Compton kinematics for scattering in the leading or distal detector, respectively (Figure 6.2.2).

found in which one or the other contribution dominates. By applying the cut on the 511 keV photons in the experiment such an interval was picked accidentally as seen in Figure 6.2.3. Therefore the dependency of the FOM for the selected energy window is much stronger than for the whole sum energy cut on the 4.44 MeV as seen in Figure 6.1.4.

From the simulation of the conditional spectra can be concluded that the shape of these spectra is more sensitive on the source location than the difference of the mean values used for the FOM. Despite this, the FOM could still be used for range verification via prompt gamma radiation when looking at specific energy intervals in the conditional spectra. These intervals are dependent on the incident photon energy and can be determined by simulations. It is more advisable to use an algorithm which matches the conditional spectra to a series of measured or simulated templates of these spectra. This is in principle a fitting algorithm to find the source location for which the full information of the conditional spectra could be used. An example of this will be explained in the next chapter. Besides, for the reconstruction of an activity distribution of sources that emit the same energy (SPCI), one has to use the conditional spectra as described in Section 2.3. This reconstruction is in principle possible for prompt gamma-ray energies.

## 6.3 Simulated Results of the Figure of Merit in Comparison

The simulation could give a basic understanding on the energy dependence of the FOM. Now the experimental setup is replicated by adding a PMMA cuboid in the simulation. This is done to verify the simulation so that it is justified to simulated other detector geometries. At first the emission profile of the 4.4 MeV gamma-ray line was determined. Secondly, based on these emission profiles, gamma-rays where emitted from discrete positions in the target as described in Section 5.2. Just like in the experiment different relative positions of the target to the detector plane were chosen. In a first run, there was no detector cover included in the simulation. The resulting FOM is shown in Figure 6.3.1.

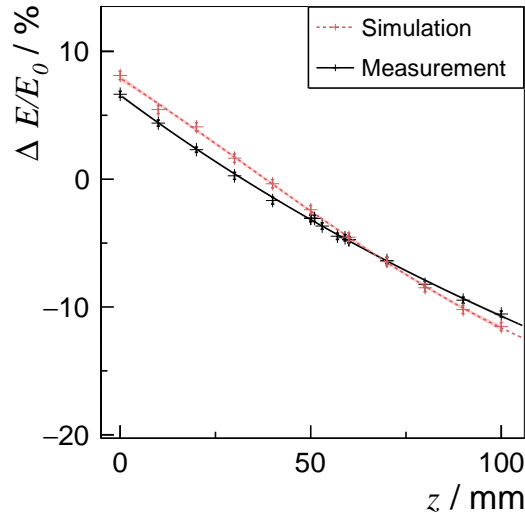


**Figure 6.3.1:** The FOM for the selected energy cut of the measurement and the simulation without detector cover in comparison.

The accordance of the two FOM seems already very good. The small discrepancies were thought to be eliminated by adding the aluminum cover from the experimental setup around the scintillators. So a cover of 400  $\mu\text{m}$  thickness was introduced to the simulation. The FOM of this second run is seen in Figure 6.3.2 (a). Surprisingly the cover does not enhance the agreement of the simulation and the measurement at all. There even is much steeper dependency of the FOM than without cover. From the first to the second step of the simulation two parameters have been changed. One parameter is the additional distance of 800  $\mu\text{m}$  between the two detectors, which leads to a more distinct selection of valid scattering angel for coincidences. Secondly, the aluminum material in between the

detectors leads to higher attenuation of coincidences by low energetic photons. To separate the influence of the two parameters, a third run of the simulation has been performed with an additional distance of 800  $\mu\text{m}$  between the two detectors. The combined results of the FOM are shown in Figure 6.3.2 (b).

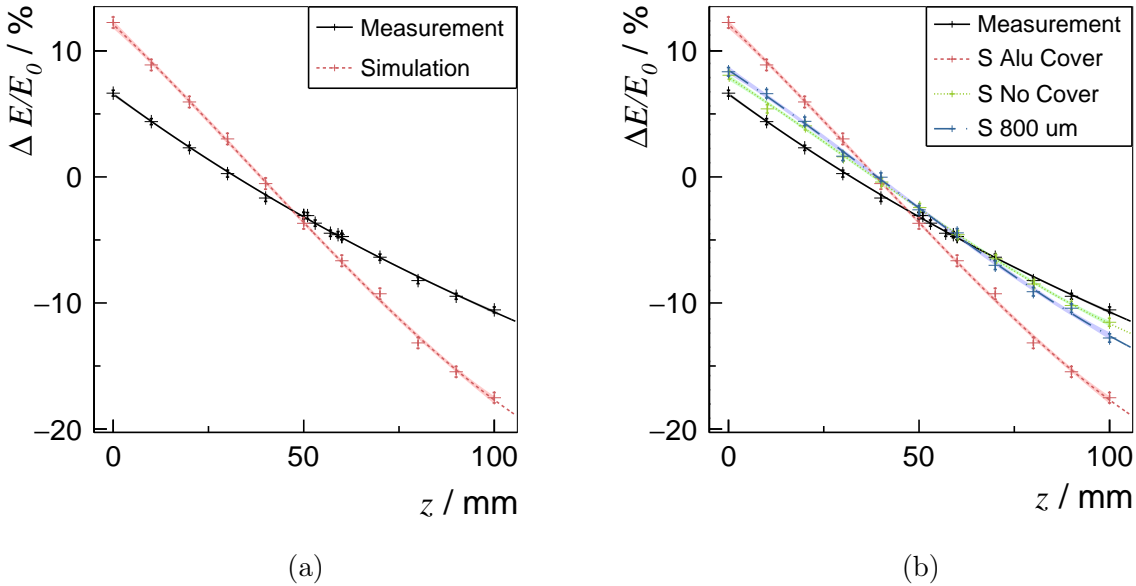


**Figure 6.3.2:** Comparison of the FOM for different simulation setups with the experiment. Plot of the FOM for the 4.4 MeV gamma-ray line with the selected energy window for the proton energy of 90 MeV and the  $\varnothing 2'' \times 2''$  CeBr<sub>3</sub> scintillators. (a) Simulated FOM obtained with the aluminum cover. (b) The FOM of other simulated setups are shown for comparison.

From this figure can be seen, that the aluminum has the larger impact on the conditional spectra. With the additional distance between the detectors the discrepancy is almost negligible. Therefore one can conclude that the geometric effect on valid scattering angles is small for this distance. As already mentioned, the aluminum cover is suppressing some coincidences more than others due to attenuation. This results in a steeper FOM in of the selected energy cut. From this, the extrapolation of the simulation cannot be justified. Therefore possible reasons for the deviation between the simulation and the experiment have to be found.

First it is to consider, that the simulation relies on cross section data that has been found to deviate from measurements [Jeyasugiththan and Peterson, 2015]. The emission profile has not been validated experimentally yet. And secondly, in the experiment there is not only the 4.4 MeV gamma-ray line emitted but a broad spectrum of lines. These lines do

also contribute to the selected energy window due to multiple Compton scattering and incomplete absorption. It has been found, that this so called correlated background is making up approximately 50% of the coincidences in a  $3\sigma$  range around the 4.4 MeV gamma-ray peak. In the following paragraph the influence of this correlated background is discussed.

In the experiment a background reduction can be achieved by choosing different energy intervals around the 4.4 MeV gamma-ray peak. Increasing the energy window around the 4.4 MeV gamma-ray line decreases the signal-to-background ratio (i.e. the ratio of “events of interest” which really result from the scattering of a 4.4 MeV gamma-ray to correlated background events). Not an arbitrary window can be chosen, as the statistical fluctuations will increase when reducing the interval width. The FOM for some exemplary energy intervals is shown in Figure 6.3.3 (a). It can clearly be concluded that the background coincidences reduce the dependency of the FOM. Also, all the fits of the data points, even from the simulation with cover, have the same point of intersection. This is interpreted as the point on the z-axis at which the correlated background and “events of interest” have the same mean energy difference in the conditional spectra. Because there is no background in the simulation, this fact shows, that the simulation with the cover agrees with the measurement.

To support this statement an arbitrary background was added to the simulated spectra. This background was estimated from the measurement<sup>1</sup>. A normalization matches the peak (P) to background (BG) ratio of the *integrals*  $I$  in the measurement to the simulation (S) by the *scaling factor*  $s$ . It was assumed that the background is fully contained in the integral of the peak. From this, the following formula is derived for the scaling factor  $s$ .

$$\frac{I_P}{I_{BG}} = \frac{I_S + s \cdot I_{BG}}{s \cdot I_{BG}} \quad (6.3.1)$$

$$s = \frac{I_S}{I_M - I_{BG}} \quad (6.3.2)$$

The scaling factor  $s$  is the factor to the estimated conditional spectra of the correlated background, before added to the simulated conditional spectra. From the background corrected

---

<sup>1</sup>As the correlated background in the selected energy window cannot be distinguished from the “events of interest”, another energy cut was applied which is close to the background expected under the 4.44 MeV peak. For extracting this background spectra the window of the selected energy window was shifted to  $E_0 = 4.74$  MeV with a width of  $\delta E_0 = 0.15$  MeV and a single detector cut of  $E_{i/r} \geq (0.511 \text{ MeV} + 0.07 \text{ MeV} + \delta E_0)$ . Then the conditional spectra of the background were shifted by  $-0.15$  MeV to match the intervals of the selected energy window.

simulated conditional spectra one can determine the FOM displayed in Figure 6.3.3 (b). The slope of the resulting FOM is found to be in more accordance to the measurement. In contrast, the curvature and the point of intersection have changed. This could be due to the chosen background window which is naturally not congruent to the selected energy window. However, the conclusion can be drawn that correlated background coincidences in the measurement are weakening the FOM of the selected energy window. As there has been no background in the simulation, this analysis showed, that the simulation with aluminum cover is modeling the experiment very well. By showing this correlation of the Geant4 model to the experiment, an extrapolation to other detector geometries is now justified.

In conclusion, the FOM of the selected energy window is influenced by correlated background coincidences from the whole prompt gamma-ray emission spectrum. The simulation could in principle create the correct FOM if the emission spectrum along the proton path was known. The deconvolution of the experimental spectrum will therefore increase the predictions of the model even further. The determination of the prompt gamma-ray emission spectrum is an ongoing activity at the OncoRay [Buch, 2018].

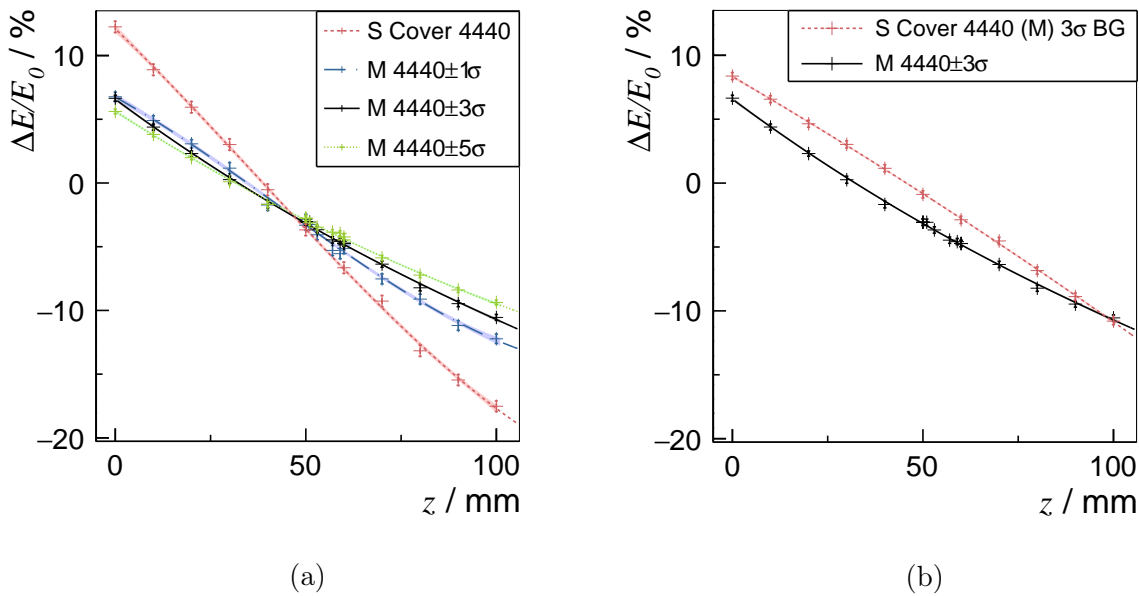


**Figure 6.3.3:** Estimation on the impact of correlated background coincidences from higher gamma-ray lines. Plot of the FOM for the 4.4 MeV gamma-ray line for the proton energy of 90 MeV and the  $\varnothing 2'' \times 2''$  CeBr<sub>3</sub> scintillators. (a) FOM of different  $\sigma$ -regions in the selected energy window in comparison to the simulation with aluminum cover. (b) FOM resulting from the simulated spectra with the added background of the measurement.

## Conclusions from this Chapter

1. A simple DGRD, consisting of two  $\varnothing 2'' \times 2''$  CeBr<sub>3</sub> scintillators, could principally be used for range verification in proton therapy by evaluation of the FOM.
2. The FOM of the selected energy cut was able to resolve range shifts smaller than 5 mm for a variation of the beam energy and a shift of the target, respectively.
3. The FOM is dependent on the sum energy of the selected coincidences and additional cuts on the energy deposition in the single detectors. Through a simulation this dependency could be explained by the Compton kinematics and the Klein-Nishina formula. In particular, high energetic photons are losing a higher relative fraction of their energy to electrons at the same scattering angle than low energetic photons.
4. The simulation also showed that the coincidence rate due to pair production in the individual detectors is dependent on the incident angle as well. This is due to the shielding amongst the detectors. Therefore such coincidences are also a valuable contribution to the coincident spectra.
5. The FOM could in principle be applied for range verification when restricting the conditional spectra to certain intervals. By this, a lot of statistics is discarded. Therefore an algorithm which matches the full conditional spectra to gain information on the source position would be preferred. Also SPCI algorithms can principally be applied on the conditional spectra at energies of prompt gamma radiation.
6. From the simulation of the proof-of-principle experiment the high influence of correlated background coincidences on the FOM was found. These coincidences are due to incomplete absorption and multiple scattering of more energetic photons than considered in the sum energy cut of the FOM. This could be identified as the reason for the deviation of the simulation and the experiment.
7. The simulation could in principle reproduce the correct FOM. By knowing the emission spectrum along the proton path, the predictions of the simulation will increase.



# 7 Optimizing a SPCC for Range Verification

In the previous chapter it could be shown that the FOM is not the optimal measure for range verification. However, the FOM did show a correlation to the proton range and the position of the target towards the detectors. The sensitivity achieved in the experiment must now be related to the clinical setting of PBS. The main issue of the FOM is the restriction to one specific energy. Therefore it shall be explored whether a fitting algorithm based on measured templates of spectra can be applied to the whole energy range of coincidences. As a far goal, a ML-EM reconstruction algorithm could not only yield the range of the protons but also the activity distribution of a certain gamma-ray line in the target. Regardless of how the range is reconstructed, all methods can be enhanced by more statistics of the conditional spectra. Therefore it will also be discussed in this chapter which efficiency can be achieved by a square segmented detector. Such a detector is believed to be a reasonable setup for range verification.

## 7.1 Test of a Template Matching Algorithm

A so called template matching algorithm can be performed on the basis of the correlation factor as defined in section 4.2. The principle idea is to have a series of template spectra  $T_i$  which are connected to the corresponding measurement position  $z_i$  on the  $z$ -axis. Then there is a measured spectrum  $M$  with an unknown position on the  $z$ -axis. Between each of the template spectra and the measurement the correlation can be calculated in dependence of the  $z$  position. Near the maximal correlation a parabola can be fitted in good approximation. Then the maximum of the parabola on the  $z$ -axis is determined as the unknown position of the measurement. The correlation factor is calculated according to the used type of spectra. Two different types of spectra were tested for this algorithm: the one-dimensional energy difference histogram of Figure 4.4.1 (c) and the two-dimensional energy histogram of Figure 4.4.1 (b). The correlation  $c(z)$  for the one-dimensional histograms can be calculated like in Equation 4.2.1. For the two-dimensional histogram the

same formula can be extended to two dimensions yielding the following. The symbols  $t_{j,k}$  and  $m_{j,k}$  denote the bin content of the two dimensional binning  $(j, k)$  of the template  $t$  and the measurement  $m$ , respectively.

$$c(z) = \sum_{j,k}^{(ROI)} \frac{t_{j,k} \cdot m_{j,k}}{\sqrt{\sum_{j,k}^{(ROI)} t_{j,k}^2 \cdot \sum_{j,k}^{(ROI)} m_{j,k}^2}} \quad (7.1.1)$$

In this paragraph the measured spectra from the proof-of-principle experiment were used as template spectra. Each measuring position is known for this set of measurements. In particular the series of 90 MeV protons and the detection system of  $\varnothing 2'' \times 2''$  CeBr<sub>3</sub> scintillators was selected. In Figure 7.1.1 the correlation is shown for the selected energy window as ROI (see section 4.4). The colored dotted vertical lines indicate three different “unknown” positions of the target. Their spectra were therefore excluded from the set of templates, to verify the algorithm even in the case of an imperfect/discrete set of templates<sup>1</sup>. The solid vertical lines of the same color mark the maximum position of the displayed parabola fit. The determined maxima and the measured “unknown” positions are in good agreement differing a few millimeters only for both cases - one and two dimensions. No robust uncertainty estimation has been performed so far. Also, this result is relatively independent of the binning. It could case-by-case be discovered, that the template matching algorithm is independent of binning as long as it is not too fine. As expected, at the boundary of the template measurements on the  $z$ -axis the position of the parabola fit is deviating more from the “unknown” position than in the center of the interval. Therefore the boundary of the template set should be avoided. Furthermore the parabola fit is only an approximation and not an exact model. It thus should only be applied in an interval close to the maximum of the correlation.

This results can also be achieved by evaluating the FOM. Hence it would be more interesting, if the template matching worked for the whole energy range of coincidences. This yields much more information and statistics which would otherwise be discarded. The results of a one and two dimensional template matching for no energy cut is seen in Figure 7.1.2. The algorithm is surprisingly working well deviating only millimeters at some “unknown” positions. Compared to the selected energy window the opening of the parabola fit is depending on the measured position. When the detectors are near the target entrance the parabola is narrow (blue) and passing the Bragg-Peak (green and red) the parabola is flat. It can be seen that the difference of the calculated and measured position is smallest

<sup>1</sup>If the position of interest was included, the correlation factor would be 1.

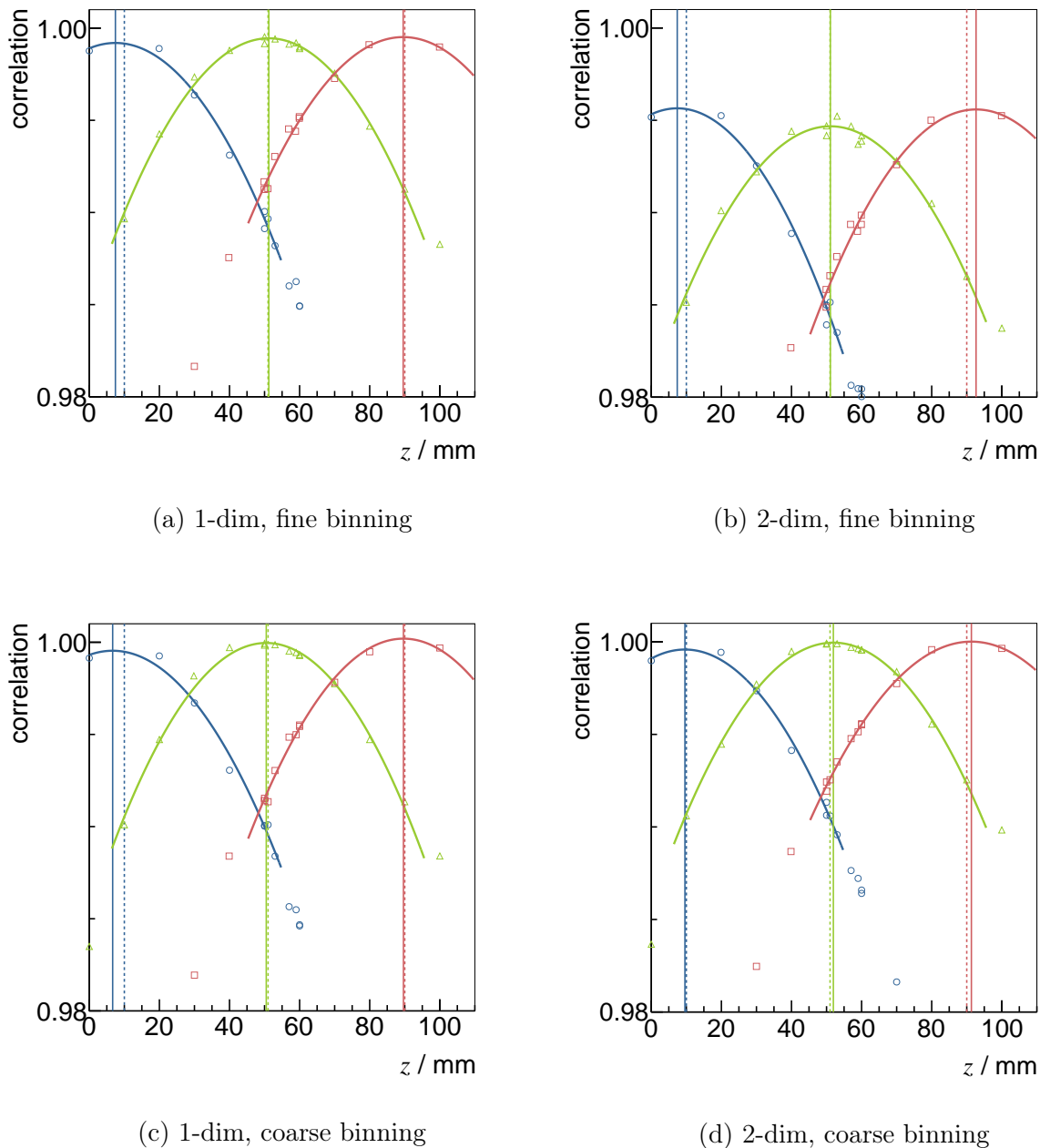


**Figure 7.1.1:** Template matching of the selected energy window with fine and rough binning in one and two dimensions, respectively.

for a the red parabola. When no energy window is selected, this suggests restricting the template matching algorithm to the region where the detectors are close to the Bragg-Peak. Using the correlation factor for template matching has the advantage of being independent of normalization of the matched spectra. As template also simulated spectra can serve. This has been tried for the selected energy window in Figure 7.1.3. As expected from the FOM, near the point of intersection the template matching works well. But as the

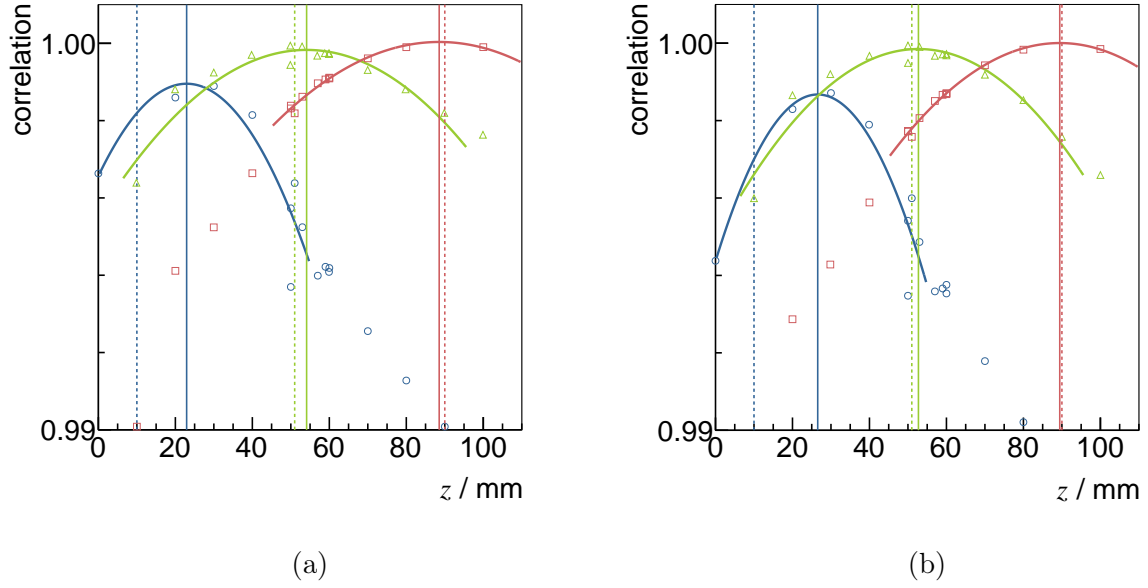


**Figure 7.1.2:** Template matching without energy cut in (a) one and (b) two dimensions.

slope of the FOM in the simulation is steeper than in the measurement, the position of the “unknown” measurement is underestimated at positions far away from this point.

## 7.2 Efficiency of the Detector Setup

The Geant4 detector model of the proof-of-principle experiment has been validated so far. From the simulation the efficiency of the system can now be determined to relate the statistical uncertainty to the clinical setting of PBS. The total efficiency  $\varepsilon_{tot}$  for a certain process to occur is dependent on two factors - the intrinsic and the geometric efficiency - as follows.

$$\varepsilon_{total} = \varepsilon_{geom} \cdot \varepsilon_{intrinsic} \quad (7.2.1)$$

The geometric efficiency  $\varepsilon_{geom}$  is defined as the fraction of the solid angle  $\Delta\Omega$  covered by the detector volume to the full solid angle.

$$\varepsilon_{geom} = \frac{\Delta\Omega}{4\pi} \quad (7.2.2)$$

The intrinsic efficiency  $\varepsilon_{intrinsic}$  is defined as the fraction of events  $N_{condition}$  leading to the “events of interest” to the number of total events  $N_{tot}$  impinging the detector. For instance, “events of interest” can be events that cause a coincident detection and are fully absorbed

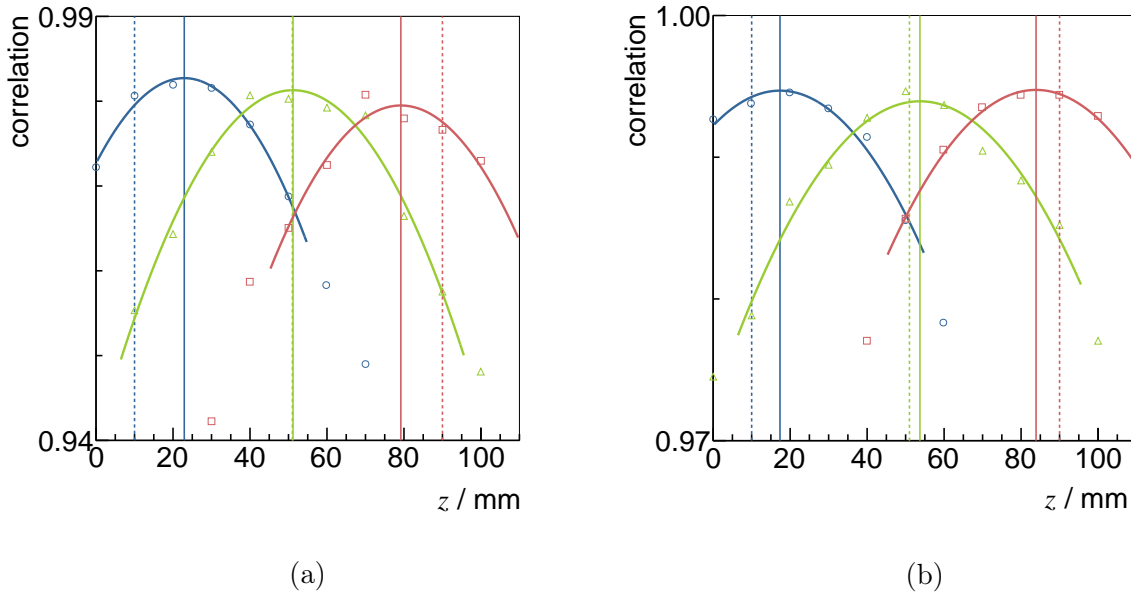


**Figure 7.1.3:** Template matching of the selected energy window with simulated spectra in one dimension. Simulation with (a) and without (b) the aluminum cover.

in the segmented detector.

$$\varepsilon_{intrinsic} = \frac{N_{condition}}{N_{tot}} \quad (7.2.3)$$

For the recent detector setup the intrinsic and the total efficiency is displayed in Figure 7.2.1. The center of the  $\varnothing 2'' \times 2''$  detectors was situated 228 mm from a point source leading to a geometrical efficiency of  $8.8 \times 10^{-3}$  without and  $9.1 \times 10^{-3}$  with cover. Two cases for “events of interest” were considered: coincidences with any and full energy absorption. The probability for full absorption is mainly affected by the attenuation causing a peak at approximately 0.6 MeV. The probability for a coincidence with any energy deposition to occur is of course higher than for a full absorption as these events are included. The deviation of both is increasing with higher photon energies. This is mainly due to multiple Compton scattering and pair production in the detectors. In principle the two lines restrict the total efficiency of a SPCC by an upper and lower bound. With a cover, the total efficiency is naturally but not significantly smaller. For 4.4 MeV the total efficiency lies roughly between 0.01 - 0.035 % in the current setup.

For the application of range verification it is important to know how many events to expect from a single pencil beam spot. Most of the pencil beam spots comprise  $10^7$  to  $10^8$  protons [Smeets, 2012]. In the region of 4.3 - 4.5 MeV (ROI) simulations of various physics

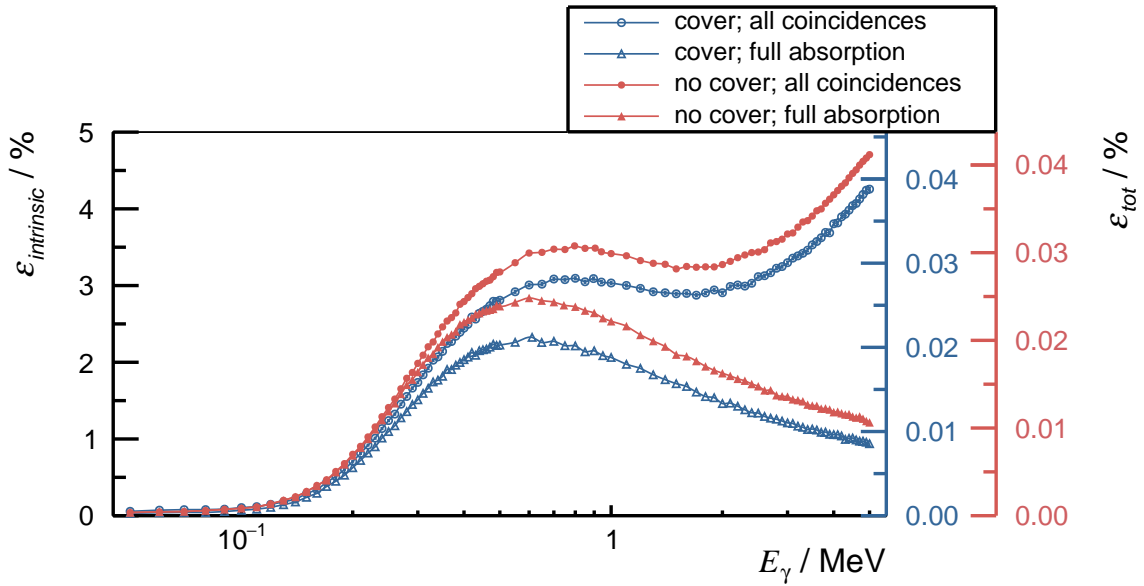


**Figure 7.2.1:** Simulated detection efficiency of the  $2'' \times 2''$  CeBr<sub>3</sub> detectors with and without an aluminum cover on each detector. “Events of interest” for the detection are coincidences of any or full energy deposition of the incident photons, respectively. Total efficiency is calculated at a distance of 228 mm from a point source to cylinder center.

lists (based on QGSP\_BIC) showed a yield of approximately 0.01 photons per proton confirming prior estimations of [Golnik et al., 2014](#). The number of valid events per spot  $N_{condition}$  can be calculated from this emission probability  $p_{\gamma ROI}$ , the number of protons per spot  $N_p$  and the total efficiency of the detector by the following formula.

$$N_{condition} = N_p \cdot p_{\gamma ROI} \cdot \varepsilon_{tot} \quad (7.2.4)$$

This would result in 10 - 100 events with full absorption of 4.4 MeV and 35 - 350 coincidences with any energy deposition per pencil beam spot. In the measurement there have been about 200 000 events with a sum energy of 4.4 MeV. As stated in section 6.3, the influence of events resulting from 4.4 MeV photons is only about 50% which are then 100 000 events in the experiment. From this number can be derived that the performed measurements have been conducted at 1000 - 10 000 times the principally feasible statistics of a single spot.

There is one problem to this estimation, the throughput of the detection system is not considered. Because of this another approximation regardless of the geometry is needed for the detectors. The maximal throughput of such a non-paralyzable detection system with a fix dead time of 1  $\mu$ s is 1 MHz, as already mentioned in section 3.1 [[Knoll, 2010](#), p. 122]. A reasonable throughput for the detection system in the measurement is about 500 kHz. A spot is typically irradiated within 10 ms [[Pausch et al., 2016a](#)]. At that throughput

this means 5000 events are registered in the detector. In the proof-of-principle experiment a fraction about 0.3% of all measured events in one detector could be classified as a coincidence with a sum energy of 4.4 MeV. As mentioned above, 50% of these events resulted from a 4.4 MeV photon. Therefore one would expect at this throughput that only  $5000 \cdot 0.5 \cdot 0.003 = 8$  fully absorbed coincidences of 4.4 MeV photons are detected in a single pencil beam spot. This number is smaller than that of the first estimation which was 10 - 100 events. This shows that the feasible coincidence rate cannot be reached by the current detection system. By segmentation of the detection system it is possible to reduce the throughput and to enable the detection of all feasible coincidences. This shall be studied in the next section.

### 7.3 Efficiency of a Segmented Detector

As proposed by [Pausch et al., 2016a](#), the setup of a square segmented detector like in Figure 2.3.1 is explored in terms of efficiency. In contrast to the last section, the throughput of the detectors is assumed to be optimal so there is no restriction on the load. This is reasonable as segmentation reduces the load on the individual segments. At the same time the throughput of the segments should stay the same as for the not segmented detector. For the development of a segmented detector mainly two geometrical parameters can be adjusted - the pixel thickness and the pixel base length of the square pixels. In addition one could also optimize the material composition like introducing a checker-board distribution and also changing the pixel cross section from square to hexagonal or circular, respectively. In principle one can say: the more information on the location of the interactions is available, the better reconstruction of the direction of a photon is feasible. Therefore minimizing the pixel cross section leads to the best results. Also the rate of fully absorbed photons will increase with larger pixel thickness. In the end the pixel cross section and thickness is a question of feasibility and costs. Also cross talk, signal-to-noise ratio and photon yield need to be considered in the optimization. The following plots shall therefore help to estimate the gain in efficiency under perfect conditions.

For this aim a  $\text{CeBr}_3$  cube of 10 cm edge length was simulated by taking interaction data in listmode. This means that for all interactions in the detector the spatial coordinates, the energy deposition, the particle types and the real time are recorded. In the analysis different pixel thicknesses and number of pixels (only square numbers) could be applied. A distance of 200 mm was set between the detector surface and a point source leading to a geometric efficiency of  $1.9 \times 10^{-2}$ . For a fix thickness of 5 cm different numbers of pixels have been studied in their influence on the intrinsic efficiency. Four different cases were

distinguished: coincidence with just two pixels and full energy deposition, coincidence with just two pixels and any energy deposition, coincidence with any number of pixels and full energy deposition and coincidence with any number of pixels and any energy deposition. The number of detectors being coincident is also called *multiplicity*  $M$ . The efficiency plots for this are shown in Figure 7.3.1. For comparison, the efficiency of the whole detector block for a full energy deposition and any energy deposition is displayed as well. The obtained data points for the photon energy of 4.4 MeV are visualized in a separate plot in Figure 7.3.2 (a) showing the dependency on the pixel base length.

It can be seen that for coincidences with  $M = 2$  a higher segmentation does not generally lead to more full or any energy depositions. This is only true below a certain energy. Above this energy because of the increasing mean free path length of the scattered photons and e.g. multiple Compton scattering higher multiplicities are preferred appearing. For the gamma-ray energy of 4.4 MeV the maximum of fully absorbed events of  $M = 2$  can be found at a pixel base length of about 25 mm. Looking at higher multiplicity more segmentation does indeed lead to higher efficiency. The efficiency is restricted by the full or any deposition in the whole detector block, respectively. The probability for any absorption to occur can be derived from the exponential law of attenuation. Therefore further segmentation will not have a large impact on the efficiency which is going into saturation. Already a pixel base length of 12.5 mm yields an intrinsic efficiency of more than 9% for full energy deposition at any multiplicity. Maximal 11% at saturation are feasible for this condition. Similarly does the curve of any energy deposition behave though it is still further away from saturation at this pixel base length.

For a fix segmentation of  $5 \times 5$  the detector thickness has been varied. The intrinsic efficiency of 4.4 MeV photons is displayed in Figure 7.3.2 (b). As expected, the efficiency for all conditions increase with the detector thickness. Also, the efficiency saturates, which makes it reasonable to find the right trade-off for the detector thickness.

A reasonable choice for the pixel base length is 10 mm and for the thickness 50 mm. With the total efficiency described above and the number of protons per spot this leads to 180 - 1800 events per spot from 4.4 MeV gamma rays which are fully absorbed but only a third of this for coincidences with multiplicity of exactly two. In Table 7.3.1 the feasible number of coincident events from 4.4 MeV gamma rays per  $10^8$  protons is displayed for different setups. Here the limitation by the throughput of the detector is not considered. The different setups are the proof-of-principle experiment, the simulated segmented detectors and an extrapolation to a  $3 \times 3$  matrix. It is yet to be studied which statistics is needed for a SPCI algorithm.



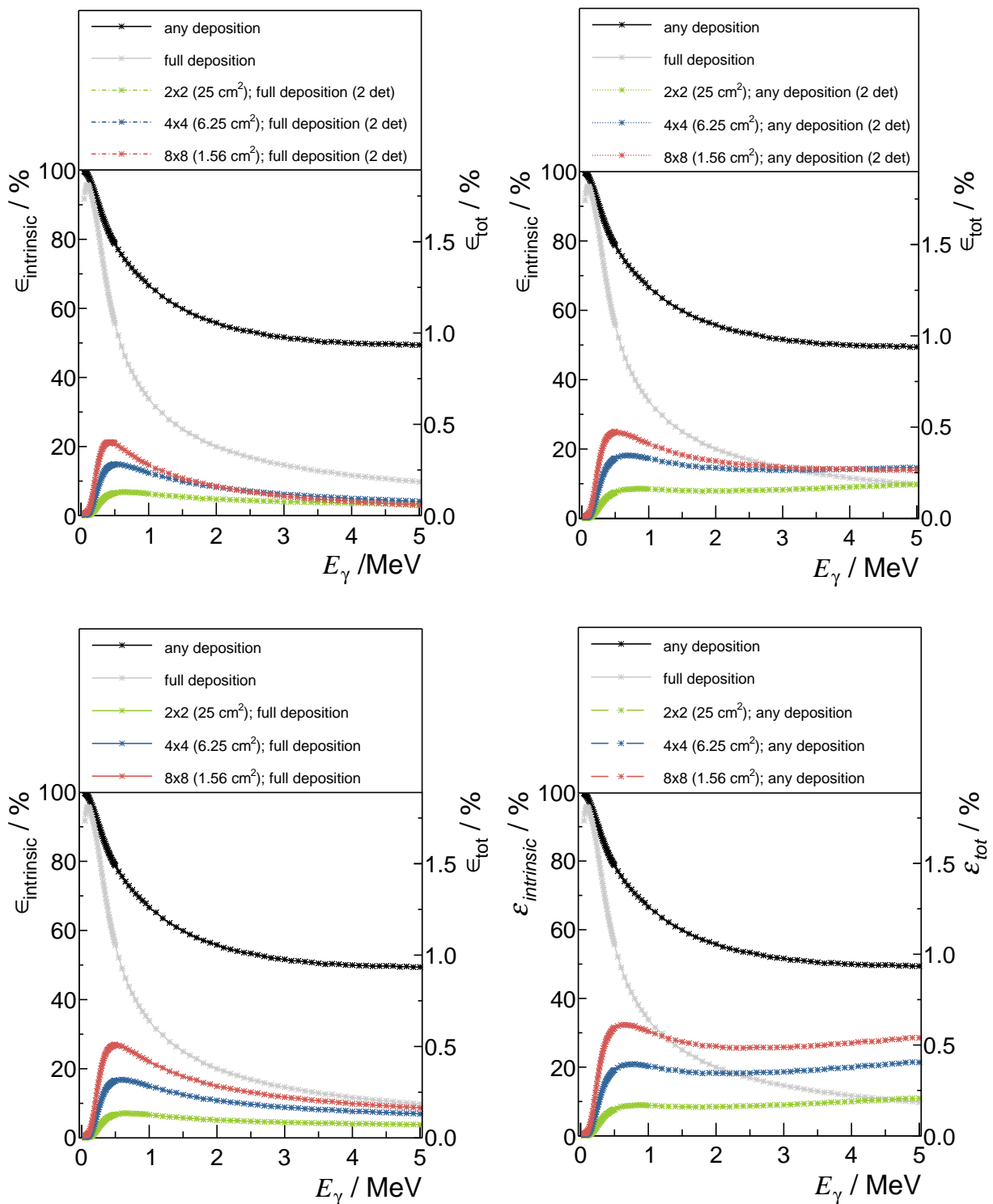


**Figure 7.3.1:** Simulated detection efficiency for selected conditions of coincidence dependent on the photon energy. Simulated was a  $10\text{ cm} \times 10\text{ cm}$   $\text{CeBr}_3$  scintillator block of  $5\text{ cm}$  thickness with different numbers of pixels (cross section given in the legend). The condition of the detection is described in the legend. If “2 det” is explicitly written, then only coincidence with multiplicity of two were selected. Elsewise all multiplicities greater equal two are considered. The total efficiency is calculated from the distance of  $200\text{ mm}$  between the point source and the detector surface.

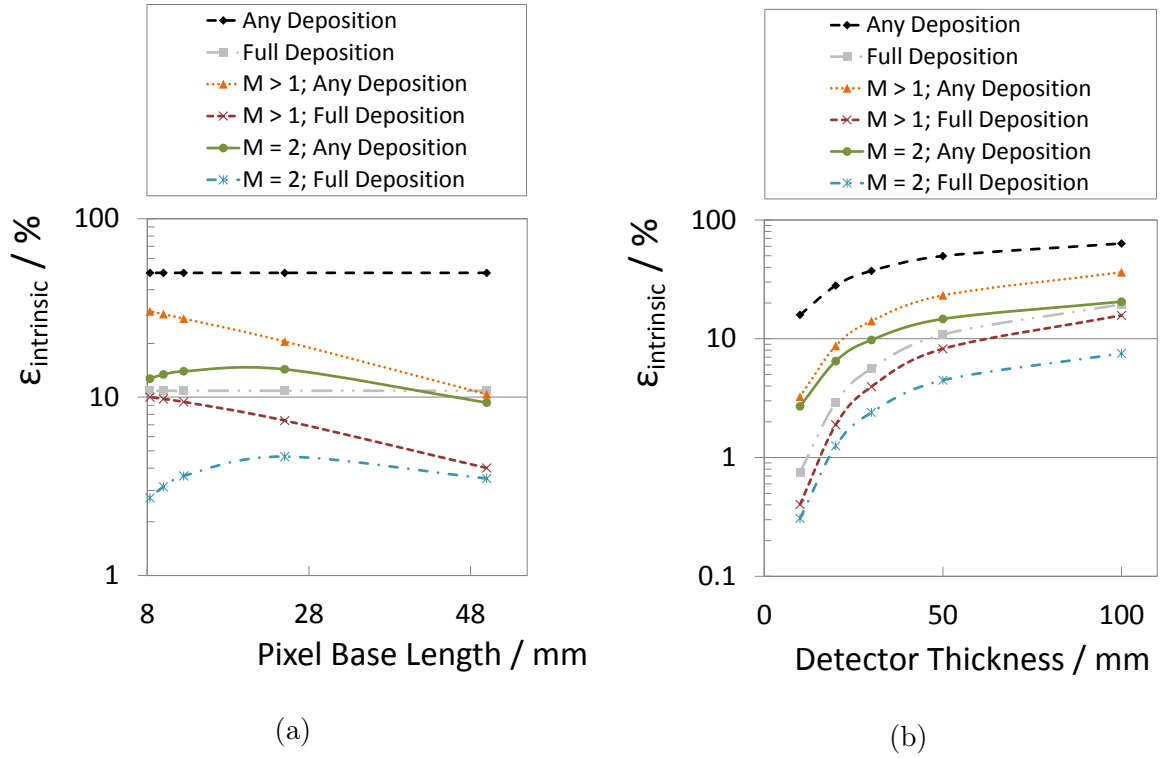


**Figure 7.3.2:** Intrinsic efficiency for different conditions of detection at 4.4 MeV photon energy. Dependency is shown for (a) pixel base length and (b) detector thickness.

**Table 7.3.1:** Feasible coincident events from 4.4 MeV gamma rays with *multiplicity*  $M$  and *sum energy*  $\Sigma E_i$  per  $10^8$  protons for different setups and selected conditions of coincidence. In the setup the detector and the distance to the point source is denoted.

Setup	Detector Volume / $\text{cm}^3$	$\frac{\Delta\Omega}{4\pi}$	# events $M = 2;$ $\Sigma E_i = 4.4 \text{ MeV}$	# events $M = 2;$ any $\Sigma E_i$	# events $M \geq 2;$ $\Sigma E_i = 4.4 \text{ MeV}$	# events $M \geq 2;$ any $\Sigma E_i$
$2 \times \varnothing 2'' \times 2''$ head-to-head @22.8 cm	206	0.009	100	350	-	-
$10 \times 10 \times 5 \text{ cm}$ $4 \times 4$ pixels @20 cm	500	0.019	880	2720	1400	3900
$10 \times 10 \times 5 \text{ cm}$ $10 \times 10$ pixels @20 cm	500	0.019	600	2550	1860	5550
$30 \times 30 \times 5 \text{ cm}$ $9 \times 10 \times 10$ pixels @30 cm (Extrapolation)	4500	0.066	2080	8850	6450	19 280

## 8 Summary and Conclusion

This work introduces a completely new approach to the field of range verification via prompt gamma-ray detection systems based on Compton scattering. At first it was shown, that the presented detectors, consisting of the digital spectrometer U100, a Photomultiplier Tube and a cerium bromide ( $\text{CeBr}_3$ ) scintillator, achieve a coincidence time resolution of about 0.8 ns at 511 keV. Rebuilding the experiment from [Gueorguiev et al., 2010](#) with these detectors could verify the eligibility of the system as a Directional Gamma Radiation Detector (DGRD). During the exploration of the experimental data, Bootstrapping has been found as a reliable method for gain drift compensation with a precision of less than 0.1 %.

In the proof-of-principle experiment it could be demonstrated based on the Figure of Merit (FOM), that the principle of a DGRD can be extended to gamma-ray energies of several MeV. At this energy the FOM is not a good measure any more as it is very sensitive to energy cuts in the conditional spectra. In contrast, the shape of the conditional spectra of a gamma-ray line is independent of such energy cuts. Therefore, to extend the principle of a DGRD to arbitrary gamma-ray energies, a simple template matching algorithm of coincident spectra was explored. The template matching was able to figure out the target position from the selected energy window. When applied on all coincidences without any energy cut, the algorithm could even then reproduce some target position within millimeters. For this the detection system has to be positioned at level to the Bragg peak. Further investigation on the potential of range extraction from this algorithm should be carried out with realistic experimental setups. Generally speaking, the precision of a few millimeters achieved in the proof-of-principle experiment from the FOM and the template matching apply to a statistic of 1000 to 10 000 times the events during a single pencil beam spot, detection dead time not considered.

A Geant4 simulation of the detection system could explain the behavior of the FOM for different gamma-ray energies. The main influences on the conditional spectra result from the Compton kinematics, the Klein-Nishina cross section and the geometry of the detector. Above 1 MeV gamma-ray energy pair production and multiple Compton scattering contribute also largely to the spectra. Against the expectation, coincidence by pair pro-

duction in the detector was found to be dependent on the source position as well due to attenuation effects in the detector.

In direct comparison with the experiment, the simulation could give a similar dependency of the FOM. It was explored that deviation are mostly due to an indistinguishable correlated background from the Compton continuum of higher prompt gamma-ray energies in the experiment. From this was concluded, that the simulation could in principle reproduce the correct FOM. By knowing the emission spectrum along the proton path, the predictions of the simulation will increase. Because of this, the determination of the prompt gamma-ray emission spectrum is an ongoing activity at the OncoRay.

Along the exploration of different physics list in Geant4 it was discovered that Doppler broadening is not implemented for neutron induced reactions in the current High Precision (HP) model of Geant4 v10.03.p01. Further investigation of models and cross sections should be ongoing to extend the simulation to the whole prompt gamma-ray spectrum and enhance the outcome. The simulated spectrum is the key parameter for the development of an imaging modality.

There are plans to build a segmented detector for the realization of such an imaging modality. Therefore a study was carried out, in which a segmented detector was analyzed in terms of detection efficiency. A  $\text{CeBr}_3$  detector block of 10 cm by 10 cm was segmented into square pixels which were varied in thickness and base length. It was found that for the multiplicity of two coincident pixels there is an optimal pixel base length depending on the initial gamma energy. When extending the reconstruction algorithms to higher multiplicities, the reduction of the pixel base length also yields a higher efficiency. With increasing pixel thickness the efficiency does generally increase so in this point the efficiency is mainly restricted by costs and the technical realization. For a detector block of 10 cm by 10 cm and 5 cm thickness and a division of  $10 \times 10$  pixels a total of 60 - 600 fully absorbed events with multiplicity of exactly two can be expected per pencil beam spot at a distance of 20 cm from the Bragg-Peak for the 4.4 MeV gamma-ray line. It must now be further investigated, if this statistics is sufficient for the introduced ML-EM reconstruction algorithm. In addition, extension of the algorithm to higher multiplicities and the analysis of other prompt gamma-ray energies is advised for range verification via Single Plane Compton Imaging (SPCI).

# Bibliography

- S. Agostinelli, J. Allison, K. Amako, J. Apostolakis, H. Araujo, P. Arce, M. Asai, D. Axen, S. Banerjee, G. Barrand, F. Behner, L. Bellagamba, J. Boudreau, L. Broglia, A. Brunengo, H. Burkhardt, S. Chauvie, J. Chuma, R. Chytracek, G. Cooperman et al. Geant4—a simulation toolkit. *Nucl. Instrum. Methods Phys. Res., Sect. A* **506**, 250–303 (2003).  
DOI: [10.1016/s0168-9002\(03\)01368-8](https://doi.org/10.1016/s0168-9002(03)01368-8)
- M. Berger, J. Hubbell, S. Seltzer, J. Chang, J. Coursey, R. Sukumar, D. Zucker and K. Olsen. XCOM: photon cross section database (version 1.5). National Institute of Standards and Technology, Gaithersburg, MD (2010). Accessed: 2018-05-24.
- M. J. Berger, J. S. Coursey, M. A. Zucker and J. J. Chang. ESTAR, PSTAR, and ASTAR: Computer Programs for Calculating Stopping-Power and Range Tables for Electrons, Protons, and Helium Ions (version 2.0.1). National Institute of Standards and Technology, Gaithersburg, MD (2017). Accessed: 2018-07-03.
- F. Beyer. Untersuchung eines neuen Konzepts für eine Bildgebung anhand der richtungsauffösenden Gammadetektion. Master's thesis, Technische Universität Dresden (2014).
- D. Brown, M. Chadwick, R. Capote, A. Kahler, A. Trkov, M. Herman, A. Sonzogni, Y. Danon, A. Carlson, M. Dunn, D. Smith, G. Hale, G. Arbanas, R. Arcilla, C. Bates, B. Beck, B. Becker, F. Brown, R. Casperson, J. Conlin et al. ENDF/B-VIII.0: The 8<sup>th</sup> Major Release of the Nuclear Reaction Data Library with CIELO-project Cross Sections, New Standards and Thermal Scattering Data. *Nucl. Data Sheets* **148**, 1 – 142 (2018). Special Issue on Nuclear Reaction Data.  
DOI: <https://doi.org/10.1016/j.nds.2018.02.001>
- R. Brun and F. Rademakers. ROOT — An object oriented data analysis framework. *Nucl. Instrum. Methods Phys. Res., Sect. A* **389**, 81–86 (1997).  
DOI: [10.1016/s0168-9002\(97\)00048-x](https://doi.org/10.1016/s0168-9002(97)00048-x)

- F. Buch. Messung des Emissionsspektrums prompter Photonen bei der Bestrahlung homogener Targets mit Protonen (working title). Master's thesis, Technische Universität Dresden (in preparation 2018).
- P. Cirrone, G. Cuttone, S. Mazzaglia, F. Romano, D. Sardina, C. Agodi, A. Attili, A. Blacato, M. De Napoli, F. Rosa, P. Kaitaniemi, F. Marchetto, I. Petrovic, A. Ristic-Fira, J. Shin, N. Tarnavsky, S. Tropea and C. Zacharatou. Hadrontherapy: a Geant4-Based Tool for Proton/Ion-Therapy Studies. *Progress in Nuclear Science and Technology* **2** (2011).
- DESTATIS. Todesursachen 2015 Deutschland. [https://www.destatis.de/DE/PresseService/Presse/Pressemitteilungen/2017/01/PD17\\_022\\_232.html](https://www.destatis.de/DE/PresseService/Presse/Pressemitteilungen/2017/01/PD17_022_232.html) (2017). Accessed: 2018-05-14.
- W. Enghardt, G. Kraft and T. Wuerschig. Detector assembly for detecting radiation with angular resolution and method for operating said assembly (2011). US Patent 8,030,617.
- C. Ferguson. General purpose Source Particle Module for Geant4/SPARSET: Technical Note (2000).
- G. Giovannini, T. Böhlen, G. Cabal, J. Bauer, T. Tessonnier, K. Frey, J. Debus, A. Mairani and K. Parodi. Variable RBE in proton therapy: comparison of different model predictions and their influence on clinical-like scenarios. *Radiation Oncology* **11** (2016). DOI: [10.1186/s13014-016-0642-6](https://doi.org/10.1186/s13014-016-0642-6)
- C. Golnik, F. Hueso-González, A. Müller, P. Dendooven, W. Enghardt, F. Fiedler, T. Kormoll, K. Roemer, J. Petzoldt, A. Wagner and G. Pausch. Range assessment in particle therapy based on prompt  $\gamma$ -ray timing measurements. *Phys. Med. Biol.* **59**, 5399–5422 (2014). DOI: [10.1088/0031-9155/59/18/5399](https://doi.org/10.1088/0031-9155/59/18/5399)
- A. Gueorguiev, G. Pausch, C. Herbach and L. Hoy. Directional gamma radiation detector system (2012a). US Patent 8,299,441.
- A. Gueorguiev, J. Preston, L. Hoy, G. Pausch, C. M. Herbach and J. Stein. A novel method to determine the directionality of radiation sources with two detectors based on coincidence measurements. In *IEEE Nuclear Science Symposium Medical Imaging Conference*, Seiten 1525–1530 (2010).

- A. Gueorguiev, J. Stein, J. Preston, L. Hoy and C. Herbach. Single plane compton camera (2012b). US Patent App. 12/806,621.
- F. Hueso-González, F. Fiedler, C. Golnik, T. Kormoll, G. Pausch, J. Petzoldt, K. E. Römer and W. Enghardt. Compton Camera and Prompt Gamma Ray Timing: Two Methods for In Vivo Range Assessment in Proton Therapy. *Front. Oncol.* **6** (2016).  
DOI: [10.3389/fonc.2016.00080](https://doi.org/10.3389/fonc.2016.00080)
- P. Jannusch. Untersuchung eines alternativen Konzepts zur bildgebenden Messung von Gammastrahlung in der Nuklearmedizin (2014).
- J. Jeyasugiththan and S. W. Peterson. Evaluation of proton inelastic reaction models in Geant4 for prompt gamma production during proton radiotherapy. *Phys. Med. Biol.* **60**, 7617–7635 (2015).  
DOI: [10.1088/0031-9155/60/19/7617](https://doi.org/10.1088/0031-9155/60/19/7617)
- L. Kelleter, A. Wrońska, J. Besuglow, A. Konefał, K. Laihem, J. Leidner, A. Magiera, K. Parodi, K. Rusiecka, A. Stahl and T. Tessonnier. Spectroscopic study of prompt-gamma emission for range verification in proton therapy. *Physica Med.* **34**, 7–17 (2017).  
DOI: [10.1016/j.ejmp.2017.01.003](https://doi.org/10.1016/j.ejmp.2017.01.003)
- G. F. Knoll. *Radiation detection and measurement*. John Wiley & Sons, Hoboken, N.J, 4th ed.. Auflage (2010).
- A.-C. Knopf and A. Lomax. In vivoproton range verification: a review. *Phys. Med. Biol.* **58**, R131–R160 (2013).  
DOI: [10.1088/0031-9155/58/15/r131](https://doi.org/10.1088/0031-9155/58/15/r131)
- R. Koch-Institut. Krebs in Deutschland für 2013/2014. [https://www.krebsdaten.de/Krebs/DE/Content/Publikationen/Krebs\\_in\\_Deutschland/kid\\_2017/krebs\\_in\\_deutschland\\_2017.pdf?\\_\\_blob=publicationFile](https://www.krebsdaten.de/Krebs/DE/Content/Publikationen/Krebs_in_Deutschland/kid_2017/krebs_in_deutschland_2017.pdf?__blob=publicationFile) (2017). Accessed: 2018-05-14.
- Y. Kong, G. Pausch, K. Romer, A. Kreuels, C. M. Herbach, M. Neuer, R. Lentering and J. Stein. Linearization of Gamma Energy Spectra in Scintillator-Based Commercial Instruments. *IEEE Trans. Nucl. Sci.* **57**, 1430–1434 (2010).  
DOI: [10.1109/TNS.2009.2033684](https://doi.org/10.1109/TNS.2009.2033684)
- B. Kozlovsky, R. J. Murphy and R. Ramaty. Nuclear Deexcitation Gamma-Ray Lines from Accelerated Particle Interactions. *The Astrophysical J. Suppl. S.* **141**, 523 (2002).  
<http://stacks.iop.org/0067-0049/141/i=2/a=523>

- M. Küchler. Einfluss starker Lastwechsel auf die Zeitnahme von Szintillationsdetektoren. Master's thesis, Technische Universität Dresden (2017).
- W. R. Leo. *Techniques for nuclear and particle physics experiments*. Springer, New York, 2nd rev. ed.. Auflage (1994).
- C. K. Müller. Untersuchung des Verhaltens eines Detektorsystems unter Lastwechseln im Hinblick auf die Prompt Gamma-Ray Timing Methode. Master's thesis, Technische Universität Dresden (2017).
- R. Orito, H. Kubo, K. Miuchi, T. Nagayoshi, A. Takada, T. Tanimori and M. Ueno. A novel design of the MeV gamma-ray imaging detector with Micro-TPC. *Nucl. Instrum. Methods Phys. Res., Sect. A* **513**, 408–412 (2003).  
DOI: [10.1016/j.nima.2003.08.071](https://doi.org/10.1016/j.nima.2003.08.071)
- PTCOG. Facilities in Operation. <https://www.ptcog.ch/index.php/facilities-in-operation> (2018). Accessed: 2018-05-14.
- H. Paganetti. *Proton therapy physics*. CRC Press, Boca Raton, FL (2012). edited by Harald Paganetti., "A Taylor & Francis book."
- H. Paul. Bragg Curve for Alphas in Air. [https://commons.wikimedia.org/wiki/File:Bragg\\_Curve\\_for\\_Alphas\\_in\\_Air.png](https://commons.wikimedia.org/wiki/File:Bragg_Curve_for_Alphas_in_Air.png) (2006). Accessed: 2018-05-14.
- G. Pausch, C. Golnik, A. Schulz and W. Enghardt. A novel scheme of compton imaging for nuclear medicine. In *2016 IEEE Nuclear Science Symposium, Medical Imaging Conference and Room-Temperature Semiconductor Detector Workshop (NSS/MIC/RTSD)*, Seiten 1–5 (2016a).
- G. Pausch, J. Petzoldt, M. Berthel, W. Enghardt, F. Fiedler, C. Golnik, F. Hueso-Gonzalez, R. Lentering, K. Romer, K. Ruhnu, J. Stein, A. Wolf and T. Kormoll. Scintillator-Based High-Throughput Fast Timing Spectroscopy for Real-Time Range Verification in Particle Therapy. *IEEE Transactions on Nuclear Science* **63**, 664–672 (2016b).  
DOI: [10.1109/tns.2016.2527822](https://doi.org/10.1109/tns.2016.2527822)
- T. E. Peterson, A. B. Brill and A. H. Walenta. High energy gamma-ray imaging using Cherenkov cone detection - A Monte Carlo study with application to a Compton camera system. In *2012 IEEE Nuclear Science Symposium and Medical Imaging Conference Record (NSS/MIC)* (2012).



- J. Petzoldt. *Toward the Clinical Application of the Prompt Gamma-Ray Timing Method for Range Verification in Proton Therapy*. PhD thesis, Technische Universität Dresden (2016).
- J. Petzoldt, K. E. Roemer, W. Enghardt, F. Fiedler, C. Golnik, F. Hueso-González, S. Helmbrecht, T. Kormoll, H. Rohling, J. Smeets, T. Werner and G. Pausch. Characterization of the microbunch time structure of proton pencil beams at a clinical treatment facility. *Phys. Med. Biol.* **61**, 2432–2456 (2016).  
DOI: [10.1088/0031-9155/61/6/2432](https://doi.org/10.1088/0031-9155/61/6/2432)
- C. Richter, G. Pausch, S. Barczyk, M. Priegnitz, I. Keitz, J. Thiele, J. Smeets, F. V. Stappen, L. Bombelli, C. Fiorini, L. Hotoiu, I. Perali, D. Prieels, W. Enghardt and M. Baumann. First clinical application of a prompt gamma based in vivo proton range verification system. *Radiother. Oncol.* **118**, 232–237 (2016).  
DOI: [10.1016/j.radonc.2016.01.004](https://doi.org/10.1016/j.radonc.2016.01.004)
- K. Roemer, G. Pausch, D. Bemmerer, M. Berthel, A. Dreyer, C. Golnik, F. Hueso-González, T. Kormoll, J. Petzoldt, H. Rohling, P. Thirolf, A. Wagner, L. Wagner, D. Weinberger and F. Fiedler. Characterization of scintillator crystals for usage as prompt gamma monitors in particle therapy. *J. Instrum.* **10**, P10033–P10033 (2015).  
DOI: [10.1088/1748-0221/10/10/p10033](https://doi.org/10.1088/1748-0221/10/10/p10033)
- J. P. Schmall, S. Surti and J. S. Karp. Characterization of stacked-crystal PET detector designs for measurement of both TOF and DOI. *Phys. Med. Biol.* **60**, 3549–3565 (2015).  
DOI: [10.1088/0031-9155/60/9/3549](https://doi.org/10.1088/0031-9155/60/9/3549)
- A. Schulz. Untersuchung eines alternativen Konzepts der nuklearmedizinischen Bildgebung mittels kollimatorfreier Detektionssysteme. Master's thesis, Technische Universität Dresden (2015).
- A. Schumann, J. Petzoldt, P. Dendooven, W. Enghardt, C. Golnik, F. Hueso-González, T. Kormoll, G. Pausch, K. Roemer and F. Fiedler. Simulation and experimental verification of prompt gamma-ray emissions during proton irradiation. *Phys. Med. Biol.* **60**, 4197–4207 (2015).  
DOI: [10.1088/0031-9155/60/10/4197](https://doi.org/10.1088/0031-9155/60/10/4197)
- J. Smeets. *Prompt gamma imaging with a slit camera for real time range control in particle therapy*. PhD thesis, Université Libre de Bruxelles (2012).

- J. Smeets, F. Roellinghoff, D. Prieels, F. Stichelbaut, A. Benilov, P. Busca, C. Fiorini, R. Peloso, M. Basilavecchia, T. Frizzi, J. C. Dehaes and A. Dubus. Prompt gamma imaging with a slit camera for real-time range control in proton therapy. *Phys. Med. Biol.* **57**, 3371–3405 (2012).  
DOI: [10.1088/0031-9155/57/11/3371](https://doi.org/10.1088/0031-9155/57/11/3371)
- B. S. Sørensen, J. Overgaard and N. Bassler. In vitro RBE-LET dependence for multiple particle types. *Acta Oncol.* **50**, 757–762 (2011).  
DOI: [10.3109/0284186x.2011.582518](https://doi.org/10.3109/0284186x.2011.582518)
- Target. U100. Target Systemelektronik GmbH & Co. KG (2018). Accessed: 2018-05-28.
- P. Thiroff, S. Aldawood, M. Boehmer, J. Bortfeldt, I. Castelhana, G. Dedes, F. Fiedler, R. Gernhäuser, C. Golnik, S. Helmbrecht, F. Hueso-González, H. v.d. Kolff, T. Kormoll, C. Lang, S. Liprandi, R. Lutter, T. Marinšek, L. Maier, G. Pausch and K. Parodi. A Compton camera prototype for prompt gamma medical imaging. *EPJ Web of Conferences* **117**, 05005 (2016).
- R. K. Tripathi, F. A. Cucinotta and J. W. Wilson. *Universal parameterization of absorption cross sections: light systems*. techreport **TP-1999-209726**, National Aeronautics and Space Administration (NASA) (1999).
- S. Vandenberghe, Y. D’Asseler, R. V. de Walle, T. Kauppinen, M. Koole, L. Bouwens, K. V. Laere, I. Lemahieu and R. Dierckx. Iterative reconstruction algorithms in nuclear medicine. *Comput. Med. Imaging Graph.* **25**, 105–111 (2001).  
DOI: [10.1016/s0895-6111\(00\)00060-4](https://doi.org/10.1016/s0895-6111(00)00060-4)
- J. M. Verburg and J. Seco. Proton range verification through prompt gamma-ray spectroscopy. *Phys. Med. Biol.* **59**, 7089–7106 (2014).  
DOI: [10.1088/0031-9155/59/23/7089](https://doi.org/10.1088/0031-9155/59/23/7089)
- J. M. Verburg, H. A. Shih and J. Seco. Simulation of prompt gamma-ray emission during proton radiotherapy. *Phys. Med. Biol.* **57**, 5459–5472 (2012).  
DOI: [10.1088/0031-9155/57/17/5459](https://doi.org/10.1088/0031-9155/57/17/5459)
- H. P. Wellisch and D. Axen. Total reaction cross-section calculations in proton nucleus scattering. *Phys. Rev. C*, 1329–32 (1996).

- T. Werner, J. Berthold, F. Hueso-González, J. Petzoldt, K. Römer, C. Richter, A. Rinscheid, A. Straessner, W. Enghardt and G. Pausch. Processing of Prompt  $\gamma$ -ray timing signals and data for precise proton range measurements at a clinical beam delivery (working title). *Phys. Med. Biol.* (in preparation 2019).
- P. Wohlfahrt, C. Möhler, K. Stützer, S. Greilich and C. Richter. Dual-energy CT based proton range prediction in head and pelvic tumor patients. *Radiother. Oncol.* **125**, 526–533 (2017).  
DOI: [10.1016/j.radonc.2017.09.042](https://doi.org/10.1016/j.radonc.2017.09.042)
- G. Zeng. Image reconstruction — a tutorial. *Comput. Med. Imaging Graph.* **25**, 97–103 (2001).  
DOI: [10.1016/s0895-6111\(00\)00059-8](https://doi.org/10.1016/s0895-6111(00)00059-8)



# List of Figures

Fig. 1.1.1:	Exemplary Bragg curve of 5.49 MeV alpha particles in air. . . . .	3
Fig. 1.3.1:	Principle of dose delivery in Pencil-Beam-Scanning mode. . . . .	5
Fig. 1.3.2:	Influence of range uncertainties on the depth dose curves of photons and protons. . . . .	6
Fig. 1.4.1:	Exemplary inelastic nuclear reaction of protons. . . . .	6
Fig. 1.4.2:	Prompt gamma-ray spectrum produced by a 150 MeV proton beam in PMMA measured with a High-Purity Germanium (HPGe) detector. . . . .	7
Fig. 2.0.1:	Dominant regions in energy for the three main interactions of photons with matter at different atomic numbers $Z$ . . . . .	9
Fig. 2.1.1:	Visualization of the Klein-Nishina cross section formula in polar coordinates. . . . .	10
Fig. 2.1.2:	Reconstruction of a photon source by the Compton camera principle. . . . .	12
Fig. 2.2.1:	Principle of a Directional Gamma Radiation Detector. . . . .	12
Fig. 2.2.2:	Ratio of the recoil electron's and the scattered photon's energy to the initial photon's energy. . . . .	14
Fig. 2.2.3:	Figure of Merit (FOM) at various gamma-ray energies. . . . .	16
Fig. 2.2.4:	Energy band structure of an activated crystalline scintillator. . . . .	16
Fig. 2.3.1:	Checkerboard setup of scintillation materials for a SPCC detector. . . . .	18
Fig. 3.1.1:	Photonic interaction cross sections of $\text{CeBr}_3$ in the energy region of interest for prompt gamma radiation. . . . .	20
Fig. 3.1.2:	Schematic sketch of the hardware and ports of the U100. . . . .	20
Fig. 3.1.3:	Coincidence time of two U100 detection units coupled to $\varnothing 2'' \times 2''$ $\text{CeBr}_3$ scintillators with different cable lengths between the spectrometers. . . . .	21
Fig. 3.2.1:	Setup of the benchmark experiment for the detection system. . . . .	22
Fig. 3.2.2:	FOM of a Na-22 point source for different sum energy conditions. . . . .	23
Fig. 3.3.1:	Sketch and photographs of the proof-of-principle experimental setup. . . . .	24
Fig. 3.3.2:	Sketch of the cyclotron and beamline at the UPTD. . . . .	25

Fig. 4.1.1:	Principle of the offline coincidence algorithm. . . . .	28
Fig. 4.1.2:	Structure chart of the offline coincidence algorithm. . . . .	28
Fig. 4.2.1:	Demonstration of the rebinning algorithm. . . . .	29
Fig. 4.2.2:	Progress graphs of the Bootstrapping algorithm. . . . .	31
Fig. 4.2.3:	Energy calibration of the template spectrum. . . . .	31
Fig. 4.2.4:	Exemplary comparison of the described Bootstrapping method to a conventional least-square fit. . . . .	32
Fig. 4.3.1:	Two-dimensional energy histograms of prompt gamma radiation for coincidences from different coincidence time windows. . . . .	34
Fig. 4.4.1:	Exemplary energy spectra of the selected energy window. . . . .	37
Fig. 5.2.1:	Perspective drawing of the experimental setup without a detector cover.	40
Fig. 5.2.2:	Visualizing the method of extracting the emission profile. . . . .	42
Fig. 5.2.3:	FOM of a restricted solid angle emission with and without correction in comparison to a constant solid angle emission. . . . .	43
Fig. 5.3.1:	Comparison of the experimental detector spectrum to the detector spectrum resulting from Geant4 reference physics lists. . . . .	45
Fig. 5.3.2:	Comparison of the emission profile from different physics lists in refer- ence to evaluated cross sections. . . . .	46
Fig. 5.3.3:	Emission spectrum of prompt gamma radiation in a PMMA target simulated by different physics lists. . . . .	47
Fig. 5.3.4:	Doppler broadening of the 4.4 MeV gamma-ray line from natural carbon.	49
Fig. 6.1.1:	Plot of the FOM for the 4.4 MeV gamma-ray line with the selected energy window. . . . .	52
Fig. 6.1.2:	Reference frame of the analysis. . . . .	52
Fig. 6.1.3:	FOM dependent on the proton energy in a steady setup. . . . .	54
Fig. 6.1.4:	Plot of the FOM for different gamma-ray lines. . . . .	55
Fig. 6.1.5:	Skewness and left/right count ratio of the measured energy difference with different energy cuts. . . . .	55
Fig. 6.2.1:	Setup of the simulation of 2" × 2" irradiated isotropically from the given point source position. . . . .	56
Fig. 6.2.2:	Normed conditional spectra for photons of different energy selected by the first interaction. . . . .	57
Fig. 6.2.3:	Energy intervals of the conditional spectra of the 4.44 MeV gamma-ray line. . . . .	59

---

Fig. 6.3.1:	The FOM for the selected energy cut of the measurement and the simulation without detector cover in comparison. . . . .	60
Fig. 6.3.2:	Comparison of the FOM for different simulation setups with the experiment. . . . .	61
Fig. 6.3.3:	Estimation on the impact of correlated background coincidences from higher gamma-ray lines on the simulation. . . . .	63
Fig. 7.1.1:	Template matching of the selected energy window with fine and coarse binning in one and two dimensions, respectively. . . . .	67
Fig. 7.1.2:	Template matching without energy cut in one and two dimensions. . .	68
Fig. 7.1.3:	Template matching of the selected energy window with simulated spectra in one dimension. . . . .	69
Fig. 7.2.1:	Simulated detection efficiency of the 2"×2" CeBr <sub>3</sub> detectors with and without an aluminium cover on each detector. . . . .	70
Fig. 7.3.1:	Simulated detection efficiency for selected conditions of coincidence dependent on the photon energy. . . . .	73
Fig. 7.3.2:	Intrinsic efficiency for different conditions of detection at 4.4 MeV photon energy. . . . .	74





# List of Tables

Tab. 1.4.1:	List of gamma-ray lines from proton reactions with oxygen and carbon.	8
Tab. 3.3.1:	List of all performed measurements of the proof-of-principle experiment.	25
Tab. 7.3.1:	Feasible coincident events from 4.4 MeV gamma rays with multiplicity $M$ and sum energy $\Sigma E_i$ per $10^8$ protons for different setups and selected conditions of coincidence. . . . .	74



# Danksagung

An dieser Stelle möchte mich bei all denjenigen bedanken, die zum Erfolg dieser Arbeit beigetragen haben und mich während meiner Zeit im Studium begleitet haben!

Allen voran meinem Professor Arno Straessner, der mich immer gefördert hat und die Zusammenarbeit mit dem OncoRay ermöglicht hat. Ganz besonders danke ich Guntram Pausch, als Leiter meiner Arbeitsgruppe am OncoRay, für seine Ideen, fachkundigen Einschätzungen und guten Ratschläge. Ich danke Toni Kögler für seine Expertise in der Analyse und Simulation und die Zeit, die er sich immer für meine Fragen genommen hat. Außerdem möchte ich Theresa Werner für anregende Diskussionen und ihr offenes Ohr danken. Vielen Dank für das Mit- und Weiterdenken und besonders das mühevollen Korrekturlesen am Ende der Masterarbeitszeit!

Ich danke unserer Mensa Gruppe für die lustigen und aufmunternden Pausen!

Ein großer Dank gilt außerdem meiner lieben Anne-Sophie für die Ermutigung und den Trost, wenn mal wieder etwas nicht klappte oder es einfach sehr stressig auf Arbeit oder im Studium war. Genauso viel bedeutet mir der Dank an meinen Eltern, die mich während der ganzen Studienjahre über begleitet haben.



# Erklärung

Hiermit versichere ich, dass ich die vorliegende Masterarbeit zum Thema

## **Single Plane Compton Imaging for Range Verification in Proton Therapy - A Proof-of-Principle Study -**

ohne unzulässige Hilfe Dritter und ohne Benutzung anderer als der angegebenen Hilfsmittel angefertigt habe. Die aus fremden Quellen direkt oder indirekt übernommenen Gedanken sind als solche kenntlich gemacht.

Die Arbeit wurde in gleicher oder ähnlicher Form noch nicht als Prüfungsleistung eingereicht. Die elektronische Fassung der Arbeit stimmt mit der gedruckten Version überein.

Jonathan Berthold

Dresden, 5. Juli 2018